Title
Finding structure in disorder: Evolutionary analyses of disordered proteins in Drosophila

Author
Singleton, Marc

Publication Date
2023

Peer reviewed|Thesis/dissertation

Finding structure in disorder: Evolutionary analyses of disordered proteins in *Drosophila*

By

Marc Singleton

A dissertation submitted in partial satisfaction of the
requirements for the degree of
Doctor of Philosophy
in
Biophysics
in the
Graduate Division
of the
University of California, Berkeley

Committee in charge:
Professor Mike Eisen, Chair
Professor Liana Lareau
Professor Susan Marqusee
Professor Priya Moorjani

Spring 2023

Abstract

Finding structure in disorder: Evolutionary analyses of disordered proteins in *Drosophila*
by
Marc Singleton

Doctor of Philosophy in Biophysics
University of California, Berkeley
Professor Mike Eisen, Chair

Living systems are governed by the interactions between large collections of atoms called macromolecules. The most important class of these macromolecules are proteins, which are the molecular machines that carry out a cell's processes. Though proteins are linear chains of simpler building blocks called amino acids, many proteins accomplish their functions by folding into well-defined three-dimensional structures. For many years scientists believed fixed structures were necessary for protein function, but by the early 2000s evidence had accumulated that segments with no fixed spatial relationship between their atoms are ubiquitous in proteins. Furthermore, because these intrinsically disordered regions (IDRs) are highly flexible and can therefore interact with diverse binding partners, they are essential for many cellular processes related to signaling and regulation.

Although our understanding of the structure and function of IDRs has grown significantly over the past two decades, predicting their functions from their sequences of amino acids remains a significant challenge. Because IDRs are structurally unconstrained, their sequences evolve rapidly and are therefore not amenable to traditional bioinformatics techniques which depend on the precise order of amino acids to make comparisons with known proteins. There is increasing evidence, though, that IDRs conserve distributed features such as their chemical composition or net charge, and a recent study clustered IDRs with similar patterns of conserved features into groups with distinct functions. This study, however, was restricted to IDRs in a set of yeast genomes, so it is unclear if these global relationships between conserved features and function are unique to yeast or a general property of IDR evolution. Thus, in this work I conduct a series of evolutionary analyses of IDRs in the genomes of 33 different species of fruit flies to detect patterns of conservation.

These comparisons, however, require the identification of IDRs with common ancestry which perform equivalent functions across many distinct organisms. Since the first genomes were sequenced in the late 1990s, researchers have developed techniques for identifying and aligning such proteins, called orthologs. While these methods are generally effective, they are conducted by automated computational pipelines and prone to errors when processing the highly divergent sequences that characterize many IDRs. The evolutionary relationships between the genomes of closely related species generally make such mistakes easier to identify, and fortunately over the past five years advances in DNA sequencing technology have yielded dramatic increases in the number of sequenced genomes in the *Drosophila* genus. However, because the existing methods for ortholog identification were designed for fewer or more distantly related genomes, they do not fully leverage such genomic redundancy to minimize errors.

Thus, in the first chapter, I develop a novel method for identifying orthologs which addresses this shortcoming and apply it to 33 *Drosophila* genomes to generate a set of aligned orthologs. In the second chapter, I then identify rapidly evolving IDRs in these alignments and analyse them with a variety of evolutionary models to dissect the forces driving their evolution and detect patterns of conservation. Finally, in the third chapter, I discuss several software tools and tutorials for fitting statistical models to data, which were created while pursuing the previous aims.

To my parents, who were always willing to indulge
another “experiment” in their kitchen sink

Acknowledgements

If it takes a village to raise a child, then it must take at least three to raise a scientist. Over the years, I've had countless friends, teachers, and mentors. These relationships have shaped the person I am today, so I'm grateful to all the people who took time out of their busy lives to help me in ways both small and large. However, I want to single out the following people who had an especially important impact on my time in graduate school.

Thank you to my advisor, Mike, for supporting me as a scientist and a person in equal measure.

Thank you to my committee, Susan, Liana, and Priya, for giving me the pep talk I needed every year.

Thank you to my lab, Holli, Stadler, Ciera, Ashley, Victoria, Augusto, and Xiao-Yong, for creating a space where it's okay to ask questions. A special thank you to my bay mates, Jenna and Colleen, for getting me through the hard days with sound advice and a healthy dose of humor.

Thank you to my undergraduate research mentors, Cathy and Jessica, for teaching me the most exciting science is at the intersection of different fields.

Thank you to my parents, Amy and David, for everything.

Thank you to my brothers, Andrew and Daniel, for giving me thick skin in the way only big brothers can.

Thank you to all the friends I've made in California and the Bay Area, for the much-needed life outside of work.

Finally, thank you to my partner, Joseph, for going on this crazy ride with me. I couldn't have done this without you.

Contents

CHAPTER 0

Introduction

Abstract

Living systems are governed by the interactions between large collections of atoms called macromolecules. The most important class of these macromolecules are proteins, which are the molecular machines that carry out a cell's processes. Though proteins are linear chains of simpler building blocks called amino acids, many proteins accomplish their functions by folding into well-defined three-dimensional structures. For many years scientists believed fixed structures were necessary for protein function, but by the early 2000s evidence had accumulated that segments with no fixed spatial relationship between their atoms are ubiquitous in proteins. Furthermore, because these intrinsically disordered regions (IDRs) are highly flexible and can therefore interact with diverse binding partners, they are essential for many cellular processes related to signaling and regulation. Although our understanding of the structure and function of IDRs has grown significantly over the past two decades, predicting their functions from their sequences of amino acids remains a significant challenge. Because IDRs are structurally unconstrained, their sequences evolve rapidly and are therefore not amenable to traditional bioinformatics techniques which depend on the precise order of amino acids to make comparisons with known proteins. There is increasing evidence, though, that IDRs conserve distributed features such as their chemical composition or net charge, and a recent study clustered IDRs with similar patterns of conserved features into groups with distinct functions. This study, however, was restricted to IDRs in a set of yeast genomes, so it is unclear if these global relationships between conserved features and function are unique to yeast or a general property of IDR evolution. Thus, in this work I conduct a series of evolutionary analyses of IDRs in the genomes of 33 different species of fruit flies to dissect the forces driving their evolution and detect patterns of conservation.

0.1 Background

Life is a physical phenomenon. Despite the complexity of living things, their processes are governed by the same physical laws that describe the planets' motion around the sun and the propagation of electromagnetic waves through space. However, many systems are too complex to describe with physical models and equations, so scientists simplify them into levels of abstraction that are more useful.[1] For example, Punnett squares facilitate the prediction of genotypes and phenotypes by distilling the complexities and nuances of diverse reproductive systems into a set of simple rules. However, since life spans a scale from single cells to entire ecosystems, biology likely employs more layers of abstraction than any other scientific discipline. One of the most powerful and widely used frameworks within the life sciences is biochemistry, which characterizes biological processes

[1] This is the origin of the observation that biology is applied chemistry and chemistry is applied physics.

in terms of their component molecules and chemical reactions. A specific focus is four classes of macromolecules called nucleic acids, carbohydrates, lipids, and proteins, all of which are unique to biological systems. Though not all biological molecules are macromolecules and not all biological macromolecules fit neatly in one of these four categories, much of life at the molecular level is understood in terms of their structure and function.[2] Each of the four has a characteristic role. Nucleic acids, *i.e.* DNA and RNA, are responsible for information storage and transfer. Carbohydrates primarily store energy but can also act as structural components of cells. Lipids are a diverse class of oily molecules which are components of cell membranes, store energy, and transmit signals. Proteins have a range of functions, including catalyzing reactions, transmitting signals, transporting materials, and providing structure. Many of these overlap with the functions of the other macromolecule classes because proteins are involved in virtually every biological process. However, unlike the others, which are often passive participants, proteins are highly active and dynamic. They respond to signals, change shape, and often use the other macromolecules as substrates in their activities. Proteins are essentially the molecular machines that carry out life's functions.

Some examples will illustrate the central role of proteins more clearly. Blood is a part of the circulatory system, which is responsible for transporting nutrients and waste. Though blood is a complex mixture, containing a cocktail of cells, proteins, sugars, gases, and ions dissolved in a medium of water, its primary cellular component is red blood cells. These cells, which give blood its red color, ferry oxygen from lungs throughout the body. While water can dissolve some oxygen, the body requires more oxygen more quickly than is available in the aqueous component of blood alone. Thus, red blood cells are packed with a special protein called hemoglobin, which binds oxygen.[3] Each red blood cell contains as many as 270 million molecules of hemoglobin [1], each of which can carry up to four oxygen molecules. Because red blood cells are so dense with hemoglobin, composing roughly 35% of their total volume [2], any defect in hemoglobin can dramatically impact the structure of the red blood cells themselves. A well-studied example is sickle cell disease where an error in the body's hemoglobin molecules deforms red blood cells into a characteristic sickle shape. This prevents them from easily flowing through blood vessels, resulting in pain and oxygen deprivation.

Whereas hemoglobin is an example of a protein mediating transport, proteins are also involved in transmitting signals and catalyzing chemical reactions. For example, the back of the eye contains a light-sensitive surface called the retina which is composed of photoreceptor cells. These cells respond to light because they produce special proteins called opsins that translate light into chemical and electrical signals which are then interpreted by the brain. Humans, and primates broadly, have three types of opsins, which are sensitive to red, green, and blue light, respectively, that mediate our color vision. Color blindness is the result of photoreceptor cells missing one of these proteins, typically either the red or green opsin. In contrast to sickle cell disease, this condition is caused by a missing rather than a mutated protein. In other cases, however, a protein is not missing or mutated, but instead not produced at the right time and place. For example, lactose is a sugar found in milk that requires a specific protein, lactase, to metabolize properly. Many humans who can digest milk products in childhood lose this ability in adulthood because they stop producing lactase. As a result, lactose in dairy products passes undigested into the colon where it is broken down by bacteria, causing symptoms such as bloating and diarrhea.

[2]Macromolecule is a loose term applied to molecules with high molecular masses. In practice, it usually refers to one of the classes listed above, among a few other prominent non-biological examples.

[3]In biology, binding is a slippery word whose exact meaning can varying greatly depending on the context. However, it generally means that a molecule physically interacts with another molecular for an extended period.

Despite performing this diverse range of functions, all proteins are made from of a set of 20 simple building blocks called amino acids.[4] Though each amino acid is chemically unique, they share a common backbone composed of two distinct and complementary "receptor" and "donor" sites for chemical bonds. Thus, in a protein the amino acids are bonded in a linear chain like beads on a string. However, once synthesized, proteins are not tidy rod-shaped molecules. Instead, the chain loops and weaves between itself creating a three-dimensional structure in a process called folding. These structures, which are highly stable and characteristic of each protein, are a result of the interactions between the amino acids in the chain and the surrounding medium, which is typically water. Because each amino acid has unique geometric and chemical properties that influence the energetics of these interactions, a protein's three-dimensional structure is encoded by the sequence of amino acids that compose it. A protein's function is in part a result of its structure. For example, the structure of hemoglobin precisely positions its amino acids and a helper molecule called a heme group to create a pocket that can stably but reversibly bind oxygen. This allows hemoglobin to carry oxygen throughout the body until it is delivered to its destination. However, people affected by sickle cell disease have a mutation in the sequence of their hemoglobin proteins which causes it to malfunction. Frequently this mutation is a single change where the sixth amino acid in the sequence, glutamate, is substituted for valine [3]. This creates a sticky patch on the surface of hemoglobin, and under low-oxygen conditions normal hemoglobin changes shape to expose a sticky patch on its surface as well. The two patches are complementary, which allows hemoglobin proteins to clump together into long, fibrous strands. These strands distort the shape of red cells, giving them their characteristic sickle shape.

Clearly, understanding the relationship between the sequence, structure, and function of proteins is essential for unraveling more complex biological phenomena. Though biologists study all three properties of proteins, they are generally most interested in function since it is the most directly related to the biological processes the protein takes part in.[5] However, functions and biological processes are not always easily identified or measured. Thus, determining a protein's structure is frequently the first step of detailed studies of its function. Though in recent years researchers have developed powerful computational tools that can accurately predict structure from sequence alone, historically structures were determined experimentally, and experimental methods still remain the gold standard. While many methods can reveal information about the structure of a protein, the most powerful techniques, X-ray crystallography, NMR spectroscopy, and cryogenic electron microscopy (cryo-EM), can map the spatial coordinates of every atom in a protein. However, this resolution requires extremely pure samples of the protein of interest. Since proteins are only produced by living systems, preparations begin with a complex mixture consisting of cells or tissue, and the protein of interest is isolated through a series of extraction and purification steps. Some proteins are only produced in small amounts or degrade easily, so each step may require substantial optimization to achieve a sufficient yield. When structural techniques were first developed in the late 1950s, they were so time-consuming that a graduate student could dedicate an entire PhD to solving a single protein structure. Many developments have substantially accelerated the process,

[4]The term amino acid encompasses any compound that contains an amino and carboxyl group. However, proteins are only synthesized from the 20 "canonical" amino acids. Another two (selenocysteine and pyrrolysine) are incorporated via a distinct mechanism under rare circumstances and are therefore considered non-standard.

[5]Function generally refers to *molecular* function which is a description of a specific chemical activity possessed by a protein. A biological process, however, is the larger "biological program" which is accomplished by the action of multiple linked molecular functions. For example, the molecular function of hemoglobin is to bind oxygen, an activity it shares with a related protein myoglobin. However, the two have different roles in the process of oxygen transport and storage. Hemoglobin is found in red blood cells where it acts as a carrier during transport. In contrast, myoglobin is found in muscle cells, where it stores oxygen until needed.

but it remains a labor-intensive technique which may require several months of effort. However, the result is a powerful map that scientists use to suggest hypotheses and interpret data.

The success of structural methods at elucidating the molecular details of protein function cemented the view that function depends on the presence of a fixed structure. While scientists understood proteins were not completely rigid and could adopt a variety of related structures, many believed that functional proteins largely had a single dominant structure [4]. Despite its strength, exceptions to this structure-function paradigm were known. For example, elastin is a protein secreted by cells which allows tissues like skin or blood vessels to repeatedly expand and contract. It imparts this elasticity by forming networks of disordered chains that act like molecular springs. When a tissue experiences a force, the chains stretch to accommodate it. When the force is removed, the chains return to their random orientations, which reduces their end-to-end length and forces the tissue to return to its original shape [5, 6]. However, as a result of this unique role in providing tissue elasticity, elastin's disorder was viewed as a specific adaptation rather than a general mechanism of protein function. In other cases, proteins had regions which returned undefined or highly variable atomic coordinates when analysed with structural techniques, indicating they lacked defined structures and were disordered. Because these segments were often short loops between structured regions, they were seen as linkers which facilitated the structure of the functional portions of proteins. By the early 2000s, though, enough exceptions had accumulated that scientists began to recognize that fully and partially disordered proteins were involved in many biological processes [7–9]. Many examples were proteins which folded on binding to their targets, commonly other proteins. This mechanism was a departure from the prevailing model of interactions between biological macromolecules which required highly stable and complementary interfaces, like two puzzle pieces fitting together. As a result, scientists speculated that disorder was an adaptation that allowed proteins to efficiently relay and regulate signals by enabling interactions with many possible targets. Furthermore, the flexibility of disordered proteins would permit environmental conditions to easily modulate these interactions.

In the following years, as the complete genomes of several scientifically important model organisms such as *S. cerevisiae* (baker's yeast), *C. elegans* (roundworm), and *D. melanogaster* (fruit fly) were sequenced for the first time, researchers applied computational methods for predicting disorder to the proteins inferred from their genomes. They discovered that disorder is ubiquitous in eukaryotic organisms,[6] with estimates of the fraction of proteins containing disordered segments of greater than 30 residues ranging between 28 and 63% [10, 11].[7] For reference, though the lengths of proteins can vary dramatically, a typical protein contains on the order of a few hundred residues, so these regions can compose a significant fraction of a protein's length. Because these segments were disordered in their native state, *i.e.* under normal operating conditions, they were termed intrinsically disordered regions (IDRs) to emphasize the disorder was not induced by exposure to chemicals or heat. Furthermore, while most proteins were predicted to contain a mixture of structure and disorder, some intrinsically disordered proteins (IDPs) were entirely or almost entirely disordered. Thus, disorder was recognized as a pervasive but poorly understood feature of proteins.

Many studies investigated the structural and functional properties of IDRs over the following years.

[6] All life belongs to one of three categories, or domains. Two, Archaea and Bacteria, are all single-celled organisms with simple cellular structures. In contrast, the cells of members of Eukarya, *i.e.* eukaryotes, are complex and contain substructures called organelles, among other differences. Animals, plants, and fungi are eukaryotes, but the domain includes many microorganisms as well.

[7] The amino acids that compose the links of a protein chain are conventionally called residues to distinguish them from their related, but chemically distinct, free forms.

They found that although IDRs still have sequence-structure-function relationships, they play by a very different set of rules. These differences manifest at all three levels but are at first most easily understood in terms of structure. Strictly speaking, a protein's structure refers its three-dimensional arrangement of atoms. Thus, structured regions in proteins, often called domains, typically fold into a small number of related structures.[8] This does not imply these folded domains are completely rigid, though. At the molecular level, everything is in constant motion. For example, at room temperature an average water molecule moves at over 500 meters per second![9] However, liquid water is so dense that it will collide with something after moving only a fraction of its own length. Likewise, in the cellular environment folded domains are buffeted by collisions with water and other molecules, but they are constrained by the rigid bonds and interactions between amino acid residues in the chain. Thus, while folded domains can "flex" and "breathe," these motions are minor variations on their overall structure.

In some cases, folded domains have multiple structures, or conformations, which are related to different functional states. For example, hemoglobin has two forms, traditionally called the T and R states [3]. The T state is hemoglobin's oxygen-free form, but on binding oxygen its structure shifts to the R state. The change is small, differing at most by only a few hydrogen atoms. However, this enough to re-orient the atoms that interact with oxygen, allowing it to bind more tightly and promoting oxygen uptake at the other three binding sites. Once the red blood cells reach their destination, other physiological factors favor the adoption of the T state, which coordinates the release of all four oxygen atoms. In the other cases, conformational changes can dramatically re-organize a protein's structure. For example, the 26S proteasome is a complex of proteins responsible for degrading other proteins. Its structure is highly complex and consists of over three dozen distinct protein subunits, which are in turn organized into three subcomplexes: a lid, a base, and a core [12, 13]. The functions of these subcomplexes are roughly analogous to the parts of a paper shredder. The lid is like the outer shell because it regulates access to the "motor" in the base and the "blades" in the core that pull in and degrade the protein, respectively.[10] Like a paper shredder, the motor is only engaged when a protein is correctly positioned in the lid. Unlike a paper shredder, however, the motor is activated by a conformational change rather than a physical switch. When the tail of a protein marked for degradation is inserted in the motor, the lid shifts by nearly forty hydrogen atoms to align the motor with the pore that leads into the core subcomplex. Despite the scale of this re-arrangement, it occurs over the span of only half a second [14]. Thus, when folded domains have multiple conformations, they are generally discrete forms without stable intermediates.

In contrast, IDRs have no fixed spatial relationship between their atoms, so their structures are sometimes described as conformational ensembles, *i.e.* collections of conformations where the distances and orientations between residues can vary considerably. Furthermore, IDRs populate a continuum of structural states over time, whereas when folded domains undergo large conformational changes, they are usually triggered by specific environmental signals or chemical modifications,

[8] Though there are various overlapping definitions, domains typically refer to independently folding regions of a protein. Domains are also described as discrete functional or evolutionary elements since proteins may contain several domains which are connected by unstructured linker sequences.

[9] This value was derived using the Maxwell–Boltzmann distribution, which is a physical model of the speeds of particles in an ideal gas. Clearly, water is not a gas at room temperature, so it should be considered a rough approximation.

[10] As with many analogies, this comparison to a paper shredder simplifies several structural and functional details of the proteasome. For example, in a paper shredder the motor powers the blades which both pull in and shred the paper. In the proteasome, however, these are distinct steps. The motor subunits in the base first physically interact with the target protein to simultaneously unfold and pull it into the core. Different subunits in the core then break the exposed chemical bonds between amino acid residues in the chain.

and the intermediate structures are transient. Despite the diversity of conformations available to IDRs, they can be broadly grouped into one of several qualitative descriptions which range from extended coils to more compact globules. The specific conformational class of a given IDR, however, is dictated by its local composition of amino acid residues. Because the chemical properties of each amino acid in the protein alphabet are dictated its specific arrangement of atoms, each has a unique impact on a protein's structure. However, to simplify discussion and analysis amino acids are often compared by quantitative factors like size or charge. One of the most useful scales for describing an amino acid's overall effect on protein structure is hydrophobicity, which measures a molecule's tendency to associate with water. Molecules which interact with water are hydrophilic (water loving), and molecules which do not are hydrophobic (water fearing). Thus, hydrophilic molecules, like sugar or alcohol, easily dissolve in water, whereas hydrophobic molecules, like fats and oils, remain separate. Since the cellular environment is largely water, the hydrophobic residues in proteins tend to cluster into a hydrophobic core. This hydrophobic collapse is a major driving force in the early stages of protein folding, so a protein's relative number of hydrophilic and hydrophobic residues is a key determinant of whether it is folded or disordered.

Unsurprisingly, disordered regions are characterized by a relative depletion of hydrophobic residues [15]. However, there is no simple formula which accurately predicts disorder in a protein using only the hydrophobicity values of its constituent residues. Other factors, such as the number and distribution of charged residues, also impact a sequence's predisposition for disorder and its resulting conformational class [16–18]. For example, sequences with high number of either positively or negatively charged residues, called polyelectrolytes, tend to form stiff rods because the like charges repel each other. However, if a sequence contains a high number of positively and negatively charged residues in roughly equal proportion, the sequence is called a strong polyampholyte, and its conformational class depends on the distribution of those charged residues. If the two classes of residues are segregated into separate blocks of like charges, they attract and form hairpins. However, if they are evenly distributed, the attractive and repulsive forces balance on average, and the sequence generally assumes expanded coil-like conformations. High numbers of polar amino acids, which are hydrophilic but not charged, are associated with semi-compact globules. Though their side chains, the portions which give each amino acid its unique identity, are hydrophilic, their interactions with water are not sufficient to overcome the tendency of the hydrophobic backbone, composed the donor and receptor sites common to all amino acids, to self-associate. Thus, like folded domains, the structures of disordered proteins are dictated by their sequences. However, because IDRs do not make stable contacts between specific residues in their chains, multiple sequences can generally correspond to a single conformational class.

The structural diversity of IDRs is directly related to their functional plasticity, and as IDRs are not confined to one conformation, they can interact with and bind to many possible partners. Often these partners are other proteins, but they can also be other macromolecules like DNA or even small molecules and ions. As a result of this adaptability, IDRs are enriched in proteins involved in cell signaling. Because cells are highly compartmentalized, they have a dizzying array of mechanisms to relay messages.[11] Many are mediated by interactions between proteins, which in turn create a change in the state of the system that propagates the signal. Often these state changes are chemical

[11]The most fundamental compartment is the cell, which roughly separates inside from outside and life from non-life. However, the cells of more complex organisms called eukaryotes contain additional subcompartments called organelles. Compartmentalization is essential in living systems because it confines and concentrates biochemical reactions that would be harmful if they occurred at the wrong place or time. However, it also introduces many complications because information in the form of physical or chemical signals cannot travel freely.

alterations made by one protein to another, which are termed post-translational modifications (PTMs).[12] One of the most common modifications is phosphorylation where a phosphate group is attached to a specific amino acid in the protein. Phosphate groups contain three negative charges, so their addition can dramatically affect a protein's structural energetics and induce a conformational change. Thus, phosphorylation often plays a key role in toggling proteins between inactive and active states. In general, though, PTMs encompass a variety of chemical modifications with similarly diverse impacts on a protein's behavior. Because IDRs are generally exposed to their environment, they are frequent targets of PTMs. However, PTMs do not occur haphazardly in proteins but are instead targeted to binding sites created by sequential patterns of residues called short linear motifs (SLiMs). SLiMs are a general mechanism for mediating interactions with proteins, so while many SLiMs are targets of PTMs, others simply recruit binding partners. In contrast to the highly structured interfaces that characterize interactions with folded domains, however, SLiMs are usually no more than ten residues [19]. Thus, their interactions are relatively weak and highly transient. As their flexibility makes SLiMs easily accessible, they are also enriched in IDRs, which in turn allows them to bind to many partners, sometimes simultaneously. IDRs therefore often act as hubs in complex regulatory networks by propagating signals from diverse sources or organizing binding partners into higher-order structures [20–22]. Furthermore, these signals and interactions are easily tuned because PTMs can modulate their meanings and strengths, respectively, by modifying only a few residues. Thus, IDRs are like "molecular computers" that integrate complex data and respond accordingly to execute different biological "programs."

Some of the most prominent examples of IDRs in cell signaling are found in the proteins that regulate the creation of other proteins. A protein's amino acid sequence is encoded in DNA in a unit called a gene, and since all cells in an organism share the same genome, they can in principle synthesize any protein encoded in it.[13] However, different cell types instead express unique complements of proteins that in large part determine their identities. This selective conversion of the information stored in DNA into proteins is called gene expression and is a highly regulated process that varies in space and time, *i.e.* between different cells and within a single cell. Though gene expression involves dozens, if not hundreds, of distinct biochemical reactions, most occur as steps within two major processes: transcription and translation. In transcription, the sequence of a protein encoded in the cell's DNA is transcribed into an intermediate molecule called messenger RNA (mRNA). mRNA is also a kind of nucleic acid, and is chemically closely related to DNA. However, as a much smaller molecule containing only the information needed to synthesize a protein, mRNA is more easily transported and manipulated in subsequent steps. Thus, if a gene stored as DNA is a cell's master record of a protein sequence, mRNA is its working copy. In translation, a vast molecular machine called the ribosome then synthesizes a protein by translating the information encoded in a strand of mRNA into a sequence of amino acids.

Both transcription and translation are tightly regulated processes, but because cells employ numerous interlocking mechanisms to control access to DNA and the creation of mRNA, transcription is often the major regulatory checkpoint in gene expression. A key step in this process is the recruitment of the protein complex which transcribes DNA into mRNA to the beginning of a gene's sequence, *i.e.* its transcription start site (TSS). The placement of this complex, called RNA

[12] A protein's amino acid sequence is encoded in a cell's DNA, and the process of reading that information to create a protein (from an intermediate molecule called RNA) is translation. Therefore, any modifications to a protein after its initial synthesis are post-translational.

[13] The DNA sequences of different cells in an organism are not always strictly identical. For example, spontaneous mutations can create changes that range from single-letter substitutions to large-scale rearrangements. In other cases, such as during the creation of sex or immune cells, a cell's DNA is intentionally modified to generate genetic diversity.

polymerase, is dictated by regulatory sequences encoded in the DNA, and while some regulatory sequences are ubiquitous, like those that mark a gene's TSS, many are gene-specific. Thus, the unique collection of regulatory sequences associated with a gene determines many aspects of its expression. RNA polymerase does not directly contact these gene-specific regulatory elements, however. Instead, proteins called transcription factors directly bind these sequences and interact with other components of the transcriptional machinery which in turn recruit RNA polymerase to the TSS. Accordingly, a typical transcription factor has two parts: a DNA-binding domain and an activation domain. DNA-binding domains are usually structured because they make stable contacts with specific regulatory sequences. In contrast, activations domains interact with the transcriptional machinery and are highly enriched in IDRs [23]. Decades of research have identified many of the proteins involved in these interactions as well as some common properties of their sequences [24–31]. Despite this progress, however, the precise mechanisms by which transcription factors locate their DNA targets and recruit the transcriptional machinery to initiate expression of specific genes remains an unsolved problem in molecular biology. As disordered regions play a key role in this process, studies which broadly investigate the relationship between the sequence, structure, and function of IDRs therefore have significant implications for our understanding of gene regulation.

0.2 Aims

Despite recent advances in identifying IDRs and their conformational ensembles from their sequences alone [16–18, 32], the relationship between their sequence and function remains poorly understood. In contrast, predictions of structure and function are readily available for many folded domains. Because they make specific contacts between residues, the sequences of folded domains are generally conserved or evolve slowly. Thus, the specific sequence of a folded domain constitutes its unique "signature." Traditional bioinformatics techniques use these signatures to detect similar protein sequences and transfer structural and functional information between them [33–35]. Though this approach is simple in principle, it is extremely difficult to perfect in practice, and fully mapping the relationship between the sequence and structure of folded domains alone hsa been an active area of research for decades. Part of the challenge is the available data is extremely sparse relative to the sheer number of possible protein sequences. Even for a moderately sized protein of 100 amino acid residues, there are $20^{100} \approx 1.3 \times 10^{130}$ possible sequences. Only in the past few years have researchers in many senses solved this problem by using advanced techniques from machine learning to leverage the information encoded in nearly two hundred thousand experimentally determined structures [36].

IDRs, however, challenge this sequence-dependent model of protein structure and function. Because they do not make stable contacts between residues which establish a fixed structure, IDRs are not generally constrained to maintain a specific sequence of residues. Thus, while there are exceptions, many IDRs evolve extremely rapidly, and related IDRs are therefore not easily identified by their sequence. There is growing evidence, though, that IDRs evolve under a different set of constraints. Because the composition and patterning of residues in an IDR dictates its conformational class, many distinct sequences can yield similar conformational ensembles. Furthermore, because modification and binding sites in IDRs are usually fewer than ten residues, their interaction interfaces are compact and can occur in multiple positions without compromising function [19]. Thus, rather than conserving specific sequences, IDRs are hypothesized to conserve distributed "molecular features" associated with those sequences. By the mid 2010s several studies had demonstrated evidence of such constraint in the flexibility [37], chemical composition [38], net charge [39], or

charge distribution of IDRs [40]. These initial studies demonstrating evidence of constraint were generally restricted to specific features or proteins. However, by comparing the observed values of various IDR-associated properties against those generated under a simulated model of evolution, in 2019 Zarin *et al.* showed most IDRs across the entire yeast proteome contain conserved features. Furthermore, they identified clusters of IDRs with common "evolutionary signatures," *i.e.* patterns of conserved features, which were associated with specific biological functions. This analysis for the first time provided a global view of the relationship between sequence and function in IDRs.

These analyses were conducted using IDRs identified in various species of yeast, which is a widely used model organism in molecular biology research. However, no known subsequent studies have determined if similar patterns of conservation are found in the IDRs of other systems. As another foundational model organism with abundant genomic information across many evolutionary lineages [41–44], the fruit fly, *Drosophila melanogaster*, is a natural choice for subsequent investigation. Furthermore, given its complex multicellular development process and shared signaling pathways with humans, the findings of such a study would significantly advance our understanding of the role of IDRs in gene regulation as well as human health and disease. The concordance of these results with the previously identified IDR clusters would also have profound implications for the broader mechanisms of IDR evolution. For example, the absence of global patterns of evolutionary signatures across IDRs in *Drosophila* would suggest they are a property of IDRs which is unique to yeast. In contrast, the identification of clusters similar to those in yeast would indicate the existence of a taxonomy of IDRs which is conserved across the tree of life.

Though modern genetic engineering techniques enable the direct manipulation of DNA sequences in living systems, gene editing remains a lengthy and work-intensive process in fruit flies. Therefore, experimentally testing the vast number of sequences needed to fully map the relationship between distributed features and function in IDRs is infeasible. The comparative genomics approach instead leverages the work done by nature to identify evolutionarily conserved features and generate specific hypotheses to guide experiments [45]. As life is constantly exploring the space of allowed proteins through evolutionary change, features which are unimportant for a protein's function or, at a larger scale, an organism's survival offer no benefit for their maintenance and are therefore gradually degraded and lost. Thus, conservation in related sequences is powerful signal of function.

These comparisons, however, require the identification of IDRs with common ancestry that perform equivalent functions across many distinct organisms. Given the difficulties with identifying similar IDRs by their sequences, this may seem like a chicken and egg problem. Fortunately, IDRs are frequently associated with more conserved folded domains. Thus, identifying evolutionarily related proteins by their overall sequence signatures and aligning them will in turn identify the equivalent IDRs in those sequences. The first step of an evolutionary analysis of IDRs, then, is the identification of proteins with common ancestry, called orthologs. Since the first genomes were sequenced in the late 1990s, researchers have developed techniques for identifying and aligning orthologs [46–49]. While these methods are generally effective, they are conducted by automated computational pipelines and prone to errors when processing the highly divergent sequences that characterize many IDRs. The evolutionary relationships between the genomes of closely related species generally make such mistakes easier to identify, and fortunately over the past five years advances in DNA sequencing technology have yielded dramatic increases in the number of sequenced genomes in the *Drosophila* genus. However, because the existing methods for ortholog identification were designed for fewer or more distantly related genomes, they do not fully leverage such genomic redundancy to minimize errors. Thus, in the first chapter, I develop a novel method for identifying

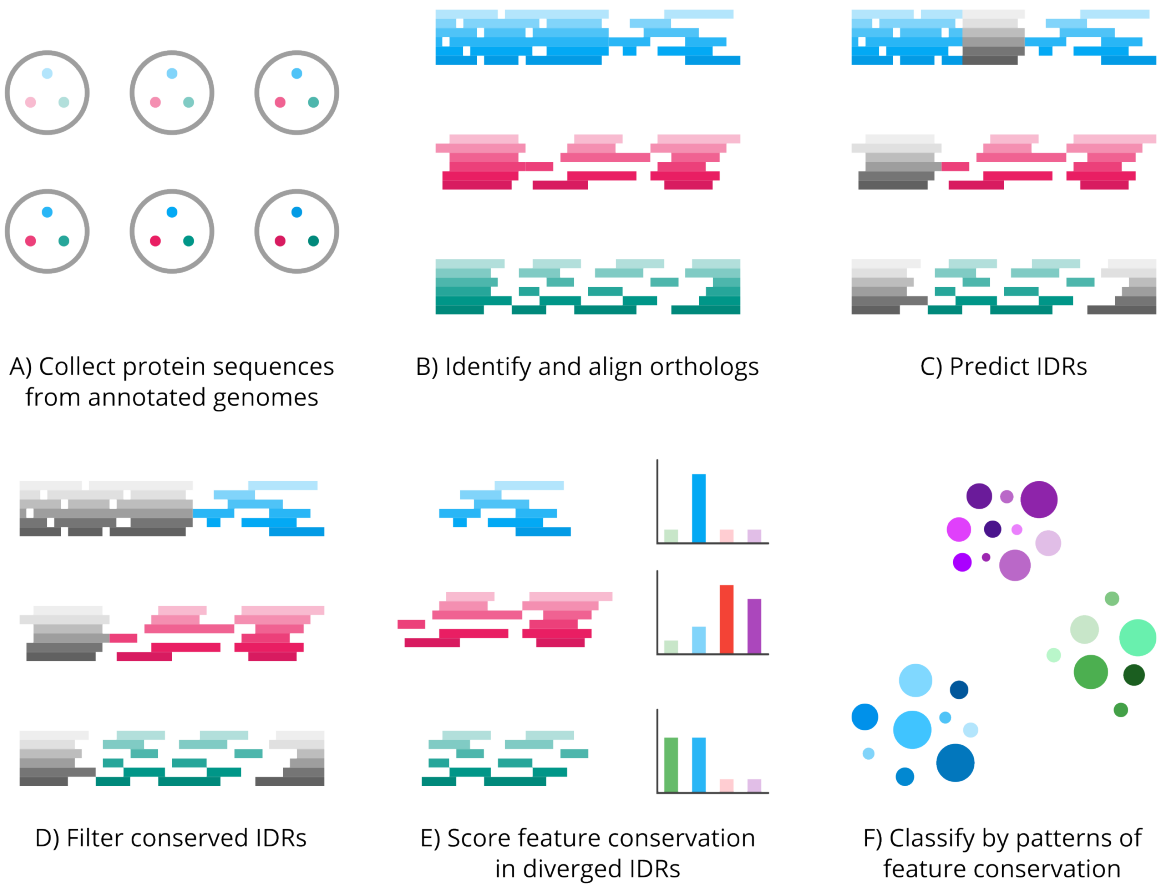

Figure 0.1. Graphical overview of aims. (A) The large open circles represent the genomes of different *Drosophila* species, and the small, filled circles represent protein sequences in those genomes. Orthologs are colored with shades of the same hue. **(B-D)** Each horizontal line represents a sequence in panel A, and together each set of lines creates an alignment. The lines are broken where gaps are inserted to align equivalent segments. The grey segments denote regions of the alignment which are not part of subsequent analyses. **(E)** Each aligned IDR is scored on four features, where the strength of that feature is indicated by the height and color of its bar. **(F)** Scoring many IDRs on these features yields three distinct clusters.

orthologs which addresses this shortcoming and apply it to 33 *Drosophila* genomes to generate a set of aligned orthologs (Fig. 0.1A-B). In the second chapter, I then identify rapidly evolving IDRs in these alignments and analyse them with a variety of evolutionary models to dissect the forces driving their evolution and detect patterns of conservation (Fig. 0.1C-F). Finally, in the third chapter, I discuss several software tools and tutorials for fitting statistical models to data, which were created while pursuing the previous aims.

CHAPTER 1

Leveraging genomic redundancy to improve inference and alignment of orthologous proteins

Abstract

Identifying protein sequences with common ancestry is a core task in bioinformatics and evolutionary biology. However, methods for inferring and aligning such sequences in annotated genomes have not kept pace with the increasing scale and complexity of the available data. Thus, in this work we implemented several improvements to the traditional methodology that more fully leverage the redundancy of closely related genomes and the organization of their annotations. Two highlights include the application of the more flexible k-clique percolation algorithm for identifying clusters of orthologous proteins and the development of a novel technique for removing poorly supported regions of alignments with a phylogenetic HMM. In making the latter, we wrote a fully documented Python package Homomorph that implements standard HMM algorithms and created a set of tutorials to promote its use by a wide audience. We applied the resulting pipeline to a set of 33 annotated *Drosophila* genomes, generating 22,813 orthologous groups and 8,566 high-quality alignments.

1.1 Introduction

Comparative genomics is a powerful tool for yielding insights into evolutionary relationships, molecular function, and the forces that drive gene, genome, and population evolution. These methods often rely on the identification of homologous sequences or homologs, that is sequences with common ancestry, since this ensures that differences between sequences reflect variations in evolution from a common point of divergence. However, many analyses impose the additional condition that the sequences have diverged through speciation events (orthology) rather than duplications (paralogy) or other mechanisms such as horizontal gene transfer [50]. The underlying assumption is orthologs have conserved equivalent functions whereas paralogs, by virtue of their redundancy, are more likely to diverge [51–55].[1] This relationship between orthology and function is an essential component of modern biological research since it permits the transfer of annotations between biological systems using sequence similarity alone.

Given this importance, methods for inferring orthologous groups of proteins were developed shortly

[1]For multiple sequences, orthology is usually defined relative to their most recent common ancestor. This technically includes sequences which split by duplication after this point (in-paralogs), but excludes sequences which split by duplication before (out-paralogs) [56]. Many current orthology inference pipelines explicitly incorporate steps to detect in-paralogs. However, the resulting orthologs groups can easily be restricted to those without in-paralogs (single copy orthologs) for analyses where an assumption of conserved function is necessary.

after the first genomes were sequenced in the late 1990s [46–48]. One early and influential approach was to cluster triangles of hits resulting from homology searches between pairs of genomes [49]. Graph-based approaches have remained popular, and in the intervening years many other researchers have refined this method by implementing various pre- and post-processing steps. Despite these improvements, many databases and pipelines use the same triangle clustering algorithm [57] or other methods which require relatively few hits between sequences to infer an orthologous group, *e.g.* connected components and other single-linkage criteria [56, 58–60] or Markov clustering [61–63]. However, the scale of biological sequence data has changed dramatically. For example, in the last decade, the number of annotated genomes available from NCBI has increased nearly 20-fold and currently exceeds 900 (Fig. A1). Though this figure is only a rough proxy of the total number of assemblies available, it will likely continue to grow rapidly in the coming years as many large-scale genome assembly efforts such as i5K [64], the Bird 10,000 Genomes Project [65], and the Vertebrate Genomes Project [66] have already yielded results. Thus, the dense taxonomic sampling made possible by these projects poses new challenges and opportunities for the standard methods of orthology inference and alignment, which implicitly assume fewer and more distantly related genomes or fail to fully leverage the redundancy and organization of their annotations.

In this work we therefore developed a computational pipeline that can robustly infer and align orthologous groups of proteins even when the genomes are highly redundant. Like many other orthology inference pipelines, our overall approach is based on clustering a graph of hits from homology searches. However, we modified many details to maximize the detection of highly diverged orthologs while also minimizing the impact of incomplete or incorrect annotations. Furthermore, since modern genome annotation pipelines frequently produce gene models and protein sequences in tandem, we implemented an additional clustering step to organize the resulting orthologous groups of proteins into gene-level units. However, most of our efforts were focused on the final step of aligning the orthologous sequences. Though genome annotation pipelines are often proficient at identifying the overall locus of genes, the accurate identification of exon boundaries and start codons when transcript evidence is limited remains an ongoing challenge [67, 68]. Consequently, protein sequences derived from annotation pipelines can include non-homologous segments of significant length or exclude highly conserved segments. Such heterogeneity in the structure and length of the sequences in an orthologous group poses many challenges for their alignment and subsequent analysis. Thus, we implemented several novel quality control and data cleaning steps to correct mis-alignments and identify likely sequencing, assembly, or annotation errors.

To develop these methods, we chose a set of 33 assembled and annotated *Drosophila* genomes, which includes all 12 species from the original *Drosophila* 12 Genomes Consortium [69]. However, the genomes of these 12 species have been re-sequenced since their first release, which has resulted in substantial improvements in their assemblies and annotations [41, 42]. Despite these developments and other several other recent genome assembly projects of species in the *Drosophila* genus, there is not yet a collection of high-quality alignments of orthologous proteins that reflects these improvements in genome assembly and diversity [43]. Given the *Drosophila* genus spans diverse habitats and over 50 million years of evolution but maintains a conserved life cycle and body plan, such a resource would facilitate a new generation of studies that illuminate the forces that drive protein evolution in unprecedented detail [70, 71].

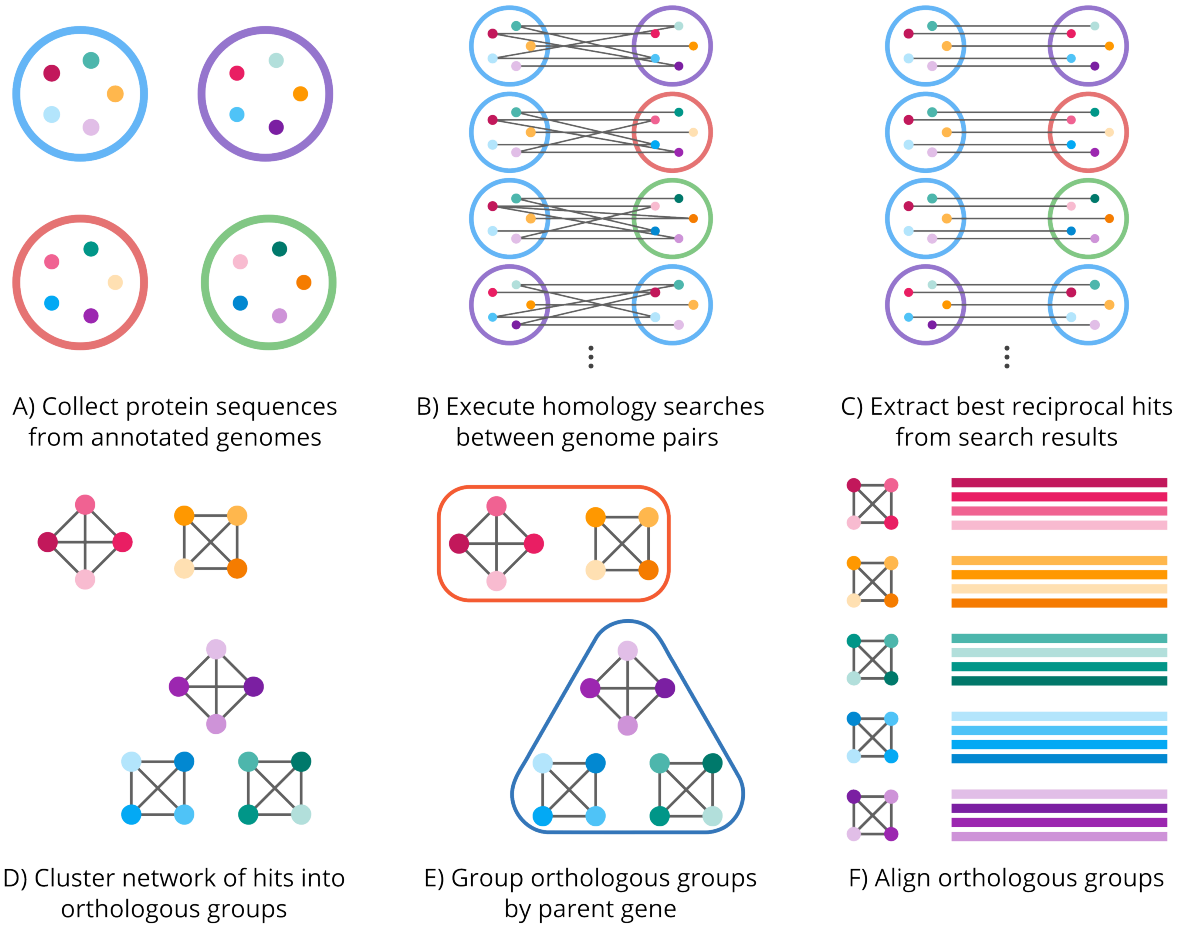

Figure 1.1. Overview of orthology inference pipeline. (A-C) The large, open circles represent the annotated genomes, and the small, filled circles represent the protein sequences associated with each annotation. Sequences that share homology are colored with shades of the same hue. **(D-F)** The small, filled circles and lines represent the same sequences and best hits from the previous steps.

1.2 Results

1.2.1 Pipeline overview

Our pipeline follows a similar overall approach to other graph-based methods of orthology inference. First, protein sequences from annotated genomes are collected (Fig. 1.1A), and homology searches are conducted between all query-target pairs of genomes (Fig. 1.1B). The raw output from these homology searches is processed to yield best hits between pairs of sequences (Fig. 1.1C). Next, the network of best hits is clustered into self-consistent orthologous groups (Fig. 1.1D). Since genes can have multiplied associated isoforms, we then implemented a novel second clustering step where orthologous groups are grouped by their parent genes, which are represented by the two sets of clusters with warm and cool colors, respectively (Fig. 1.1E). Finally, representative sequences in each orthologous group are aligned (Fig. 1.1F). In the following sections, we discuss each of these and other steps which were omitted for clarity in greater detail.

1.2.2 Input genomes and pre-processing

All annotated genomes in the genus *Drosophila* available in April 2022 were downloaded from NCBI's RefSeq database. The assemblies annotated by the NCBI eukaryotic genome annotation pipeline have passed several quality checks and all have supporting transcript evidence, so the annotations are generally highly complete [72]. The *D. miranda* annotation was excluded due to its unusual karyotype [73]. Other annotations were excluded after preliminary clustering showed a deficiency in the number of orthologous groups containing those genomes, indicating their annotations were less complete (data not shown). The *D. melanogaster* annotation was downloaded from FlyBase [44]. In total, the input data consists of 33 genomes, which are listed in Table A1. Many genes have transcripts that differ only in their UTRs, and as a result there are many duplicate protein sequences in the annotations. Though not strictly necessary, we removed the duplicates in our pipeline, which greatly reduced the computational burden of later steps.

1.2.3 Extraction of best hits from BLAST output

The protein sequences in each genome annotation were searched against each other in reciprocal pairs using BLAST, yielding a list of high-scoring segment pairs (HSPs) for each query-target pair [33]. HSPs are local alignments, meaning they do not necessarily span the entire lengths of the query and target sequences. Consequently, the search algorithm may return multiple HSPs for each query-target pair if statistically significant regions of homology are separated by nonhomologous or poorly conserved regions. Though the most significant HSP is often used to represent all HSPs between a query-target pair, this approach can fail to rank the pairs by their overall significance if their alignments are broken into multiple HSPs. Furthermore, since query-target pairs were later filtered by the amount overlap between their sequences, it can also exclude pairs that pass the overlap threshold even if the most significant HSP alone does not. Thus, HSPs were merged into a single object called a hit. The best hits for each query were then taken as the highest-scoring hits that passed a minimum overlap criterion and were reciprocal between the query and target sequences.

1.2.4 Clustering in orthologous groups

The best hits between sequences are naturally visualized as a graph where sequences are nodes and best hits are edges between nodes. Two connected components, sets of nodes joined by a sequence of edges, are shown (Fig. 1.2A-B). The sequences in the first (Fig. 1.2A) all contain C2H2 zinc fingers, whereas the sequences in the second (Fig. 1.2B) are members of the Par-1 family of serine/threonine protein kinases. In both components, some sets of nodes have a high density of edges, forming distinct clusters, whereas other nodes are only sparsely connected to their neighbors. To better understand the structure of these two components, we calculated the number of sequences, unique genes, and unique species in each. The first has 385, 346, and 33 sequences, genes, and species, respectively, and the second has 222, 33, and 33 sequences, genes, and species, respectively. We then plotted the relationship between the number sequences and unique genes across all components to see if this pattern holds true generally (Fig. 1.2C). Two distinct trendlines are apparent. The first increases linearly with the number of sequences with a slope of one, indicating each sequence is generally associated with a unique gene. The second is constant with an intercept of 33, indicating the number of unique genes quickly saturates at the total number of genomes. Thus, there are generally two classes of components. The first is composed of many distinct genes, whereas the second is composed of many different isoforms of a single group of genes.

The diffuse networks observed in the first component class are likely the result of a combination of factors, including rapid evolution, gene duplication, and annotation errors. Regardless of their origin, these hits are not strong candidates for comparative analyses since an orthology relationship is supported by relatively few genome pairs. Instead, likely orthologs should consistently identify each other as best reciprocal hits across many genome pairs. The same is true of the hits in the second component class. Although the genes as a unit form a single orthologous group, sequences with few hits are likely non-conserved or tissue-specific isoforms. Thus, orthologous groups can be operationally defined as self-consistent clusters in the hit graph. However, sequence divergence or assembly and annotation errors may prevent a best reciprocal hit between orthologous sequences across all genome pairs. In fact, although the most common number of reciprocal hits is 32, one fewer than the total number of genomes, many sequences have fewer (Fig. 1.2D). Thus, the clustering method should require a high degree of self-consistency without demanding complete consensus.

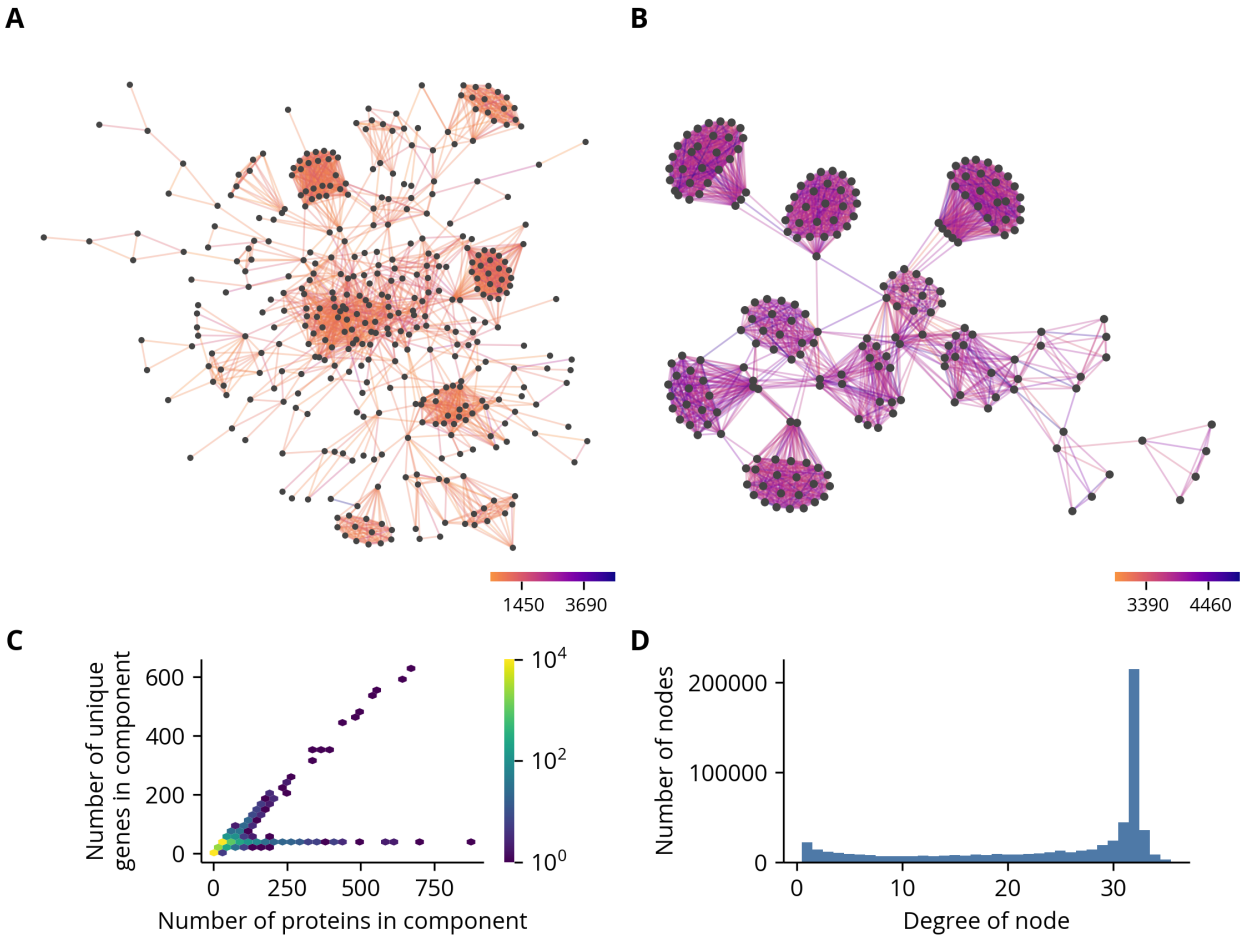

Figure 1.2. Selected connected components of hit graph and summary statistics. (A-B) Two distinct connected components of the hit graph. Edges are colored by the value of their bit score. **(C)** Hexbin plot of the number of sequences and the number of unique genes in each component. **(D)** Histogram of number edges associated with each sequence, *i.e.* the degree of each node. Only the lower 99th percentile of the distribution is shown.

The identification of sets of densely connected nodes in graphs is known as community detection in network analysis. While many community detection algorithms are available, only some are

commonly used in the context of orthology inference. One early method that remains popular is building clusters progressively by identifying nodes that form a triangle with at least two other nodes in the cluster [49, 57]. Other approaches include the MCL algorithm, which clusters graphs by simulating stochastic flow [61–63], and connected components or other single-linkage criteria [56, 58–60]. While these methods are robust when clustering hit graphs derived from smaller or more diverse sets of genomes, they are not suitable for the large number of closely related genomes in this work since they require relatively few edges to define a cluster. For example, the MCL algorithm and connected components method assign a node to a cluster as long as it has a single edge, and triangle clustering only requires two edges to two adjacent nodes.

However, connected components and triangle clustering are special cases of the more general k-clique percolation algorithm where k equals two and three, respectively. The clique percolation algorithm detects clusters by first identifying cliques, sets of nodes which are fully connected, of a specified size k in the graph (Fig. 1.3A). Clusters are then taken as the connected components of an overlap graph where an edge exists between two cliques if they share k-1 nodes in common. An intuitive way to visualize this algorithm is by "rolling" a clique of some size k over the graph (Fig. 1.3B). More specifically, a cluster is initiated when a set of nodes which form a k-clique is identified. The cluster expands by shifting the k-clique to an adjacent k-clique that shares k-1 nodes in common with the current k-clique. A cluster stops expanding when there are no adjacent k-cliques, and the algorithm terminates when there are no k-cliques which are not part of a cluster. The strength of this algorithm is its ability to exclude sparsely connected nodes from clusters with an easily tunable parameter k. Higher values of k require greater overlap between a candidate node and those already in the cluster and therefore produce tighter clusters at the cost of excluding more speculative orthology relationships (Fig. 1.3C). We set k to four as compromise between these concerns, yielding 22,813 orthologous groups, a plurality of which contained all 33 species (Fig. A2).

1.2.5 Addition of paralogs to orthologous groups

A weakness of the best reciprocal hits criterion is its exclusion of recently diverged paralogs. Since only the highest scoring hits for each query are included in the graph, a paralog without a corresponding duplicate in the target genome is ignored if it is marginally more diverged than the other copy. This is corrected by adding likely paralogs to the orthologous groups. Briefly, the protein sequences in each genome were searched against themselves. If the bit score for an intra-genome hit exceeded the bit score of any inter-genome hits for the same query, the two sequences were identified as a paralogous pair. Orthologous groups were then supplemented with paralogs by adding the paired sequences for each of the original members of the orthologous group. Most orthologous groups contain no paralogs, and those that do generally have few relative to the original number of sequences in the group (Fig. A3).

1.2.6 Grouping orthologous groups by gene

As genes can have several annotated isoforms, each gene can be associated with several orthologous groups. However, the orthologous groups are not organized into gene-level units since they were clustered using sequence similarity only. A graph-based approach was therefore used to group orthologous groups with similar sets of parent genes. First, a gene overlap graph was constructed by defining an edge between orthologous groups if the intersection of their associated sets of parent genes is at least 50% of the smaller of the two. Gene groups were then taken as the connected components of the resulting graph, yielding 14,909 groups. This is commensurate with the roughly

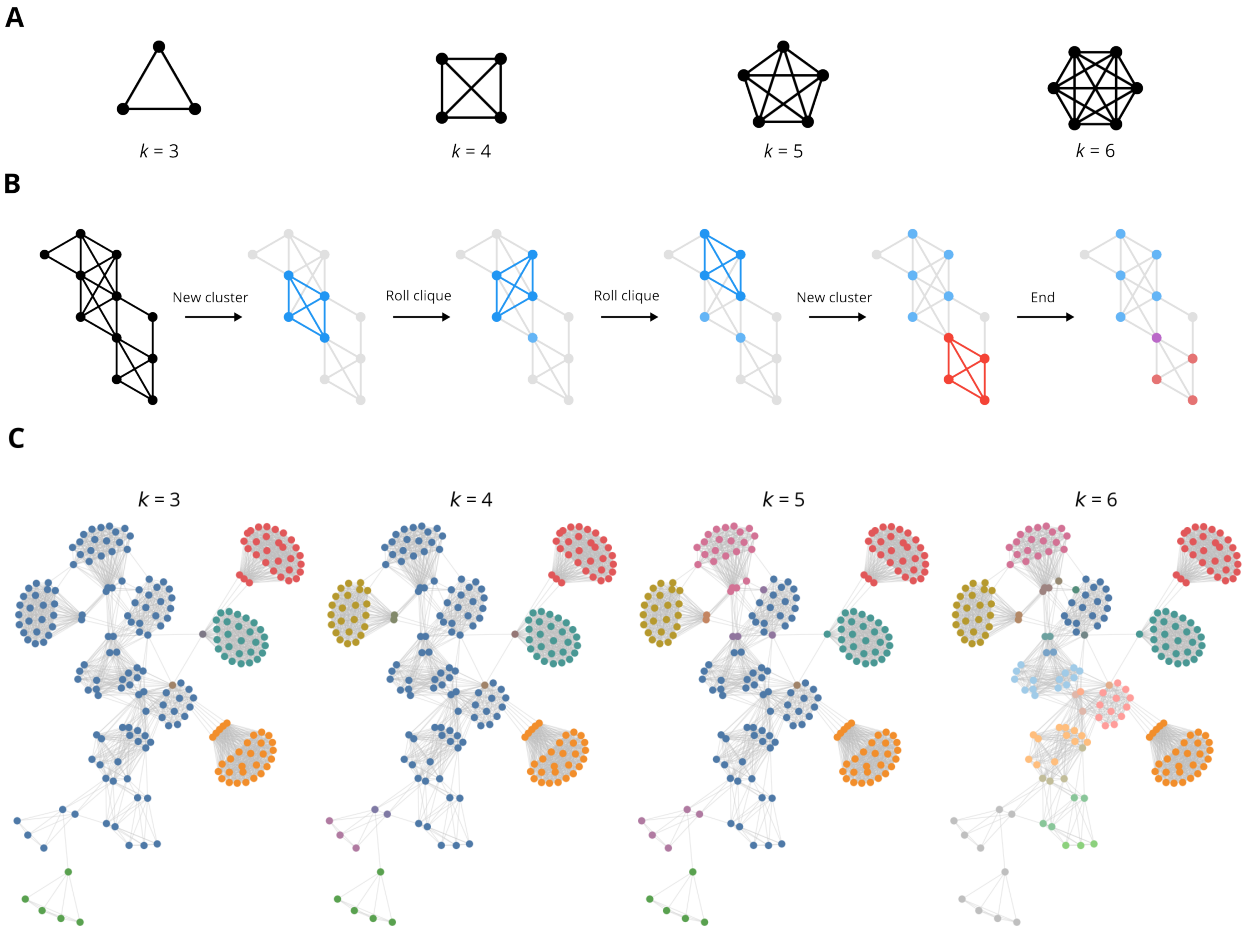

Figure 1.3. Clique percolation algorithm. (A) Cliques for k equal to three, four, five, and six. k equal to one and two correspond to a single node and two nodes joined by an edge, respectively. **(B)** Illustration of clique percolation algorithm where $k = 4$. **(C)** A single component clustered by clique percolation with varying values of k. Nodes are colored according to their cluster. If a node belongs to multiple clusters, it uses a blend of those colors.

15,000 genes in each genome, which suggests this approach has successfully clustered orthologous groups derived from a common set of parent genes.

1.2.7 Initial alignment and selection of representative sequences

Since the NCBI annotation pipeline incorporates transcriptome data from a variety of sources, its inputs are heterogeneous in sequencing depth, developmental stage, and tissue of origin across different genomes. As a result, some genomes are annotated with different or multiple splice isoforms of a given orthologous gene, which can create complex networks in the resulting hit graph. For example, if the genomes are variably annotated with one or both of two distinct isoforms, the resulting graph may contain two clusters connected by a "bridge" formed by the genomes which contain only one of the isoforms. If the nodes bridging the two clusters form cliques with themselves and the clusters, the clique percolation algorithm will merge all the nodes into a single orthologous group where some genes have multiple associated sequences. However, these additional sequences can complicate downstream comparative analyses that may not easily generalize to genes with

multiple associated sequences. Thus, in our pipeline a single representative was chosen for each gene using an alignment-based strategy detailed in the methods section. Briefly, a statistical profile was created from an alignment of the sequences in each orthologous group, and the representative for each gene was chosen as the sequence which best matched this profile.

1.2.8 Selection of single copy orthologous groups

The criteria for selecting orthologous groups for further analyses depends on the biological question under investigation. For example, studies of gene duplication will focus on orthologous groups with paralogs in some lineages but not in others. In contrast, analyses which assume functional conservation should restrict the orthologous groups to single copy orthologs since paralogs more frequently undergo functional divergence [53–55]. A simple method for identifying such groups is requiring each species to have exactly one associated gene. However, since the probability of at least one missing gene annotation approaches one as the total number of genomes increases, this is too restrictive and fails to leverage the redundancy of closely related genomes. Instead, a set of phylogenetic diversity criteria detailed in Table A2 were applied to ensure the major lineages were represented in downstream analyses. Furthermore, genome-wide analyses should select one orthologous group per each of the previously identified gene groups as to not bias the results towards genes with many distinct groups of isoforms. In summary, orthologous groups failing the phylogenetic diversity criteria were first removed, and the representative for each gene group was chosen as the highest scoring orthologous group when ranked by the number species and the sum of the bit scores associated with each edge. This significantly reduced the number of orthologous groups from 22,813 to 8,566.

1.2.9 Alignment refinement

Though the pipeline's quality control measures ensure a high degree of overall sequence identity between members of an orthologous group, some sequences contain long "poorly supported" segments which have no homology to most or any other sequences in the alignment. Since most common multiple sequence alignment algorithms assume the sequences are largely homologous, these segments are sometimes "over-aligned" by forcing them into alignment where chance sequence similarities occur. Typically, these segments remain contiguous, so the alignments alternate between short runs of columns with few or no gaps and large gap-rich regions (Fig. 1.4A-B, left). More rarely, when long poorly supported segments are adjacent to a long gap in the same sequence, the two are interlaced, yielding long gaps interrupted by short segments of spurious alignment (Fig. 1.4C, left).

The aligner MAFFT has a mode for addressing over-alignment with a parameter, a_{max}, that adjusts the strength of the correction [74, 75]. a_{max} varies between 0 and 1, with higher values yielding a stronger correction. While values above 0.8 completely eliminate over-alignment and successfully align highly conserved regions, the alignment as a whole is severely degraded, as even homologous sequences with a small amount of divergence are separated by gaps. Thus, in our pipeline orthologous groups were aligned in two stages. In the first, the sequences were aligned with a strong correction of 0.7. Highly conserved regions were identified, which divided the alignment into a complementary set of diverged regions. The sequences in each of these regions were extracted and aligned separately with a more conservative value for a_{max} of 0.4. The resulting "sub-alignments" were "stitched" back into their positions in the original alignment. By defining highly conserved "anchor" regions, this approach largely prevents the alignment of chance sequence similarities in long poorly supported segments (Fig. 1.4, right).

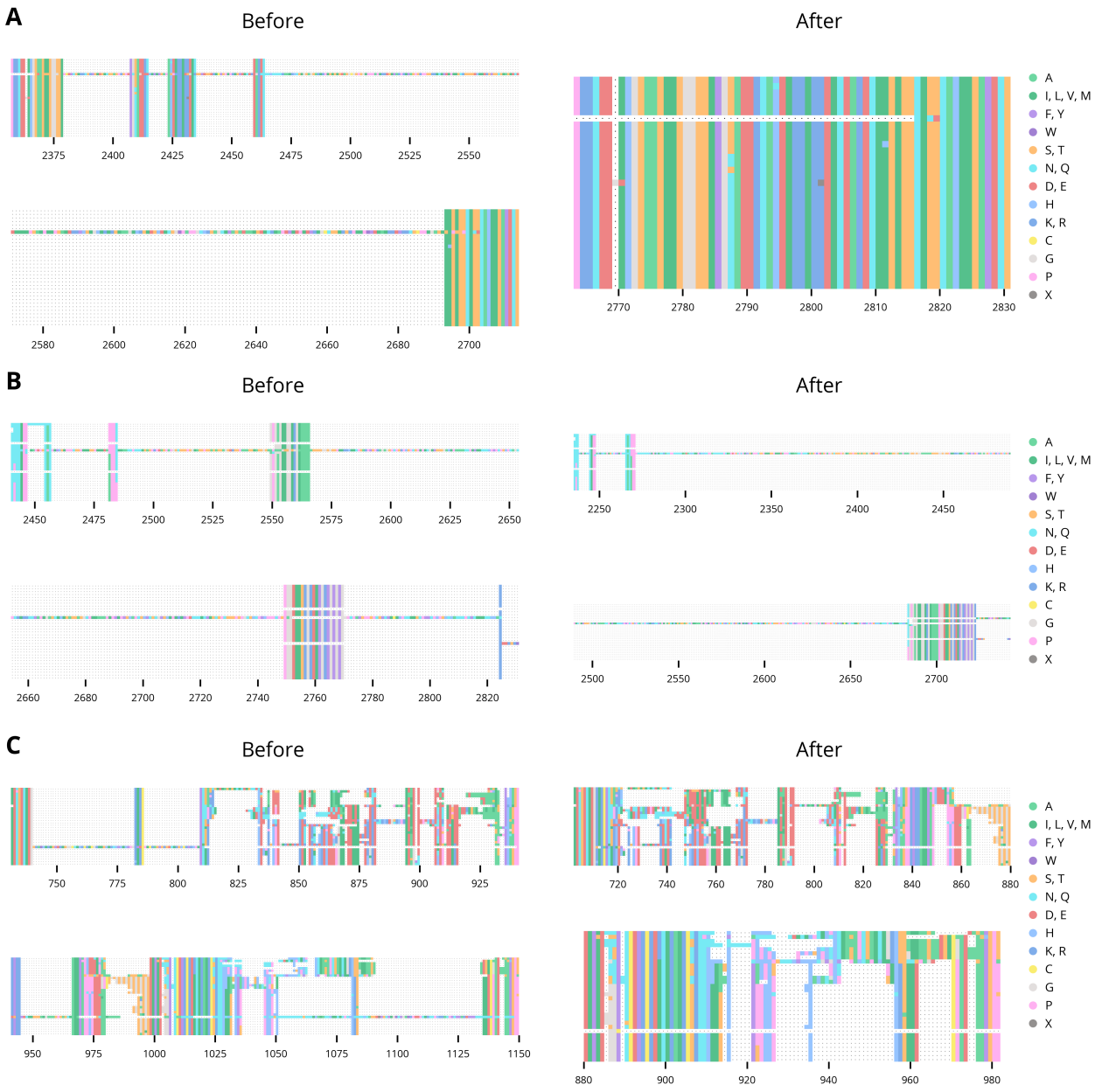

Figure 1.4. Alignment with long poorly supported segments. The alignments of representative sequences in orthologous groups 0167 **(A)**, 2770 **(B)**, and 23D9 **(C)** before and after refinement.

1.2.10 Alignment curation

Although the refinement process corrects most cases of over-alignment, the alignment may still contain regions whose aligned segments have poor or inconsistent support. For example, long poorly supported segments in internal regions were not removed from the alignment since they are bounded by at least one consensus column to the left and right. Additionally, some regions have a significant fraction of sequences with strongly supported segments, but the observed gap pattern is discordant with the expected phylogenetic relationships. Since they are present in so few sequences, the former segments are likely artifactual, resulting from errors during assembly

or annotation. (Biological explanations such as alternative splice sites, frameshift mutations, or transposition events are also possible, however.) In contrast, the high sequence identity and clear boundaries of the segments in the latter regions suggest they are conserved but skipped exons. Given the heterogeneous sourcing of the transcript evidence, these sequences containing these segments are likely splice isoforms specific to certain tissues or developmental stage.

Since the segments in these regions are likely the result of incorrect or incomplete annotations rather than meaningful biological variation, maintaining them in the alignments would propagate spurious homologies to subsequent analyses. This is a common issue in alignments generated by automated pipelines, so downstream analyses often focus on the strongly supported regions by removing or "trimming" columns below some threshold number of gaps or sequence identity [76, 77]. This approach, however, is inadequate if the taxonomic sampling is dense, as a single indel event along a lineage containing many species can increase the number of gaps above the threshold. Moreover, as this method does not incorporate any spatial information, it can rapidly alternate between trimming and preserving columns. Thus, it can severely disrupt any analyses which are sensitive to the spatial organization of an alignment.

Phylogenetic HMMs (phylo-HMMs) are statistical models that incorporate phylogenetic and spatial information to calculate the probability that each observation in a sequence was generated by one of several hidden states [78, 79]. Since they can evaluate both the probability of a gap pattern in a column given the known phylogenetic relationships and the local context, a phylo-HMM was used to segment the alignment into contiguous regions with different patterns of gaps. A fully specified phylo-HMM requires a fixed number of hidden states and a probability distribution for each. Thus, we identified four distinct types of regions in the alignments, roughly corresponding to highly conserved regions with few to no gaps, diverged regions, regions with a stable gap pattern discordant with the expected phylogenetic relationships, and regions with poorly supported segments. For simplicity, however, we refer to the states that generate each type of region as 1A, 1B, 2, and 3, respectively. To model probability distributions for each state, we first conceptualized the observed alignments as the superposition of two distinct processes (Fig. 1.5A, left). The first is a phylogenetic process which evolves and splits a single ancestral sequence over time according to a tree. The second is the annotation process which can erroneously exclude or include segments from a sequence. The result is an alignment of annotated sequences which contains evolutionary information obscured by noise from the annotation process, shown here by the exclusion of three N-terminal residues in the fourth annotated sequence. To simplify modeling this behavior with an HMM, we coded the sequences into binary symbols. The distributions for each state then consisted of two components derived from the encoded sequences (Fig. 1.5A, right). The first component models the gap pattern with a Markov process. This Markov process is in turn composed of two subprocesses where the first is a phylogenetic process, and the second is a jump process. These subprocess roughly correspond to changes caused by evolution and annotation, respectively. Because this first component did not fully capture the propensity for the gap patterns to remain constant, we included a second component that models the "gap stickiness" as a beta-binomial random variable by counting the number of symbols that remain constant between columns. Each component is associated with a set of parameters, and the unique parameters for each state yield its characteristic gap pattern and gap stickiness.

After the model was trained on manually labeled examples, it was used to assign a label to the columns in each alignment. Columns assigned to states 1A and 1B are the regions of interest for downstream analyses since the gaps generally follow the expected pattern given the phylogenetic

tree. In contrast, columns assigned to states 2 and 3 largely corresponded to the long poorly supported segments and phylogenetically discordant regions discussed previously and were therefore removed from the alignments. In the example decoded alignment shown, the decoded states closely follow the expected patterns (Fig. 1.5B). Overall, 29% of alignments were trimmed of at least one segment or region. However, 87% of the trims were segment trims, meaning the removed segments were largely inferred as state 3 and therefore were likely long poorly supported segments aligned to few if any other sequences (Fig. A5).

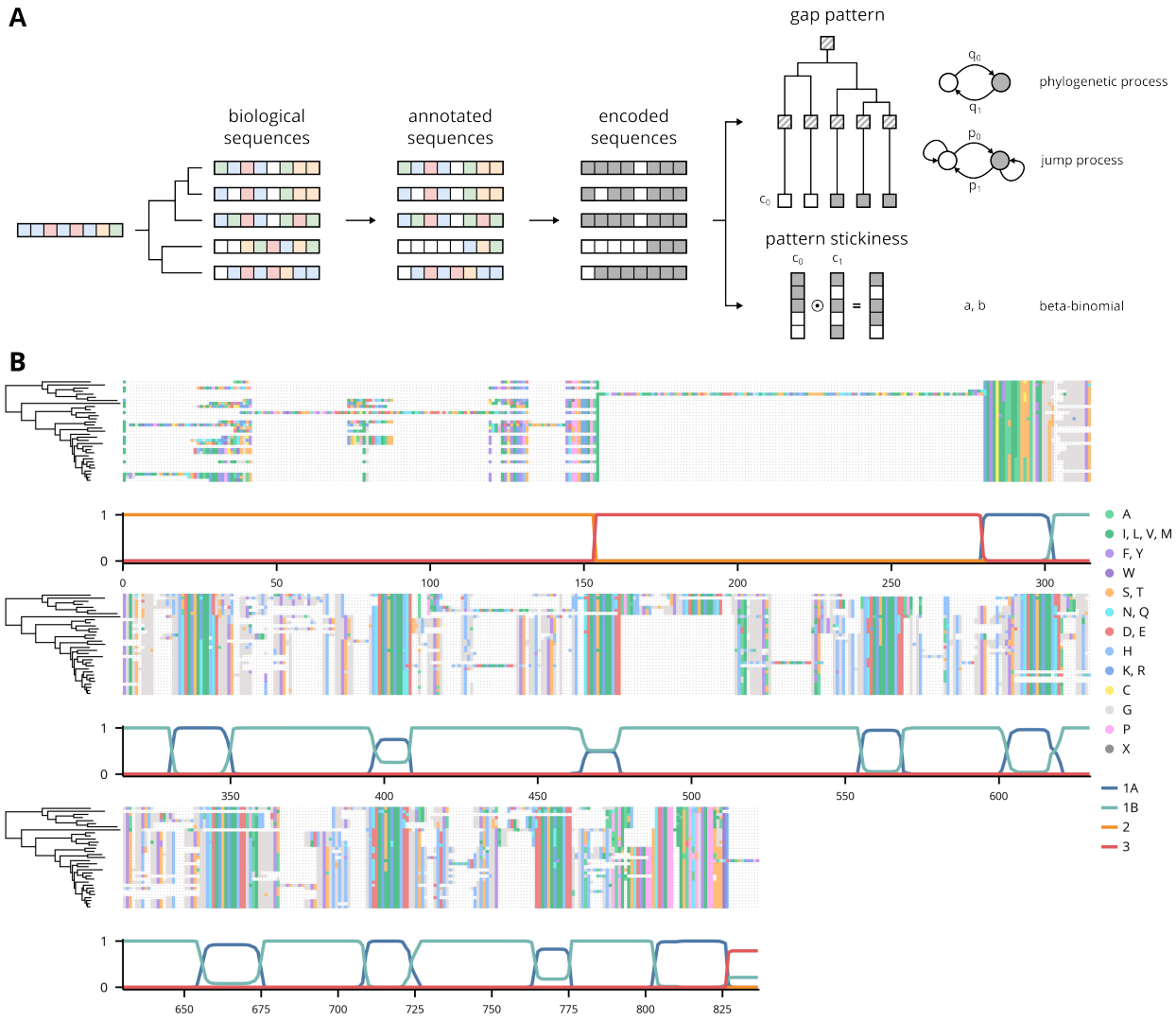

Figure 1.5. HMM emission architecture and a decoded alignment. (A) Schematic of theoretical alignment generating process and corresponding probabilistic components in HMM. White and colored boxes indicate gap and non-gap symbols in the biological sequences, respectively. White and grey boxes indicate gap and non-gap symbols in the encoded sequences, respectively. c_0 and c_1 indicate the first and second columns in the alignment, respectively. The parameters associated with each component are shown to the right. **(B)** The alignment of the representative sequences in orthologous group 2252 decoded using the trained HMM.

Though the phylo-HMM removed phylogenetically incongruent insertions, some sequences still contained extensive segments of uninterrupted gaps. These segments are easily identified in regions which are otherwise highly conserved, so they are also likely the result of incorrect or incomplete

annotations. However, they can also span more diverged regions, which complicates a simple rule- or threshold-based approach for identifying them. Thus, another phylo-HMM was trained to label each position in a sequence as generated by either a "missing" or "not missing" state. In this case, though, the aligned sequences were processed individually and not as aligned columns. As the previous phylo-HMM already ensured each column has sufficient support, these labels can instead be used to exclude sequences from downstream analyses depending on the amount of tolerated overlap with the regions of interest. Overall, 15% of alignments have at least one sequence with a segment of "missing" data (Fig. A7).

1.2.11 Inference of species trees

Many phylogenetic methods require a species tree to inform the evolutionary relationships between sequences. In fact, the phylo-HMMs discussed previously used a species tree as an input, though we omitted this detail for clarity of exposition. Therefore, to support the curation step and other downstream analyses, we sought to infer phylogenetic trees from the aligned sequences. However, since the roots of phylogenetic trees are not identifiable with commonly used time-reversible substitution models, we repeated the orthology inference pipeline with the outgroup species *Scaptodrosophila lebanonensis*. Afterwards, we inferred phylogenetic trees using the LG model of amino acid substitution from 100 meta-alignments sampled from alignments of single copy orthologous groups. We then combined them into a single consensus tree (Fig. 1.6A). To provide a similar tree for the analysis of non-coding regions, we inferred phylogenetic trees using the GTR model of nucleotide substitution from 100 meta-alignments sampled from nucleotide alignments which were "reverse translated" from the protein alignments and their corresponding coding sequences (1.6B). Both trees have an identical topology, which is consistent with other published phylogenies [69, 80].

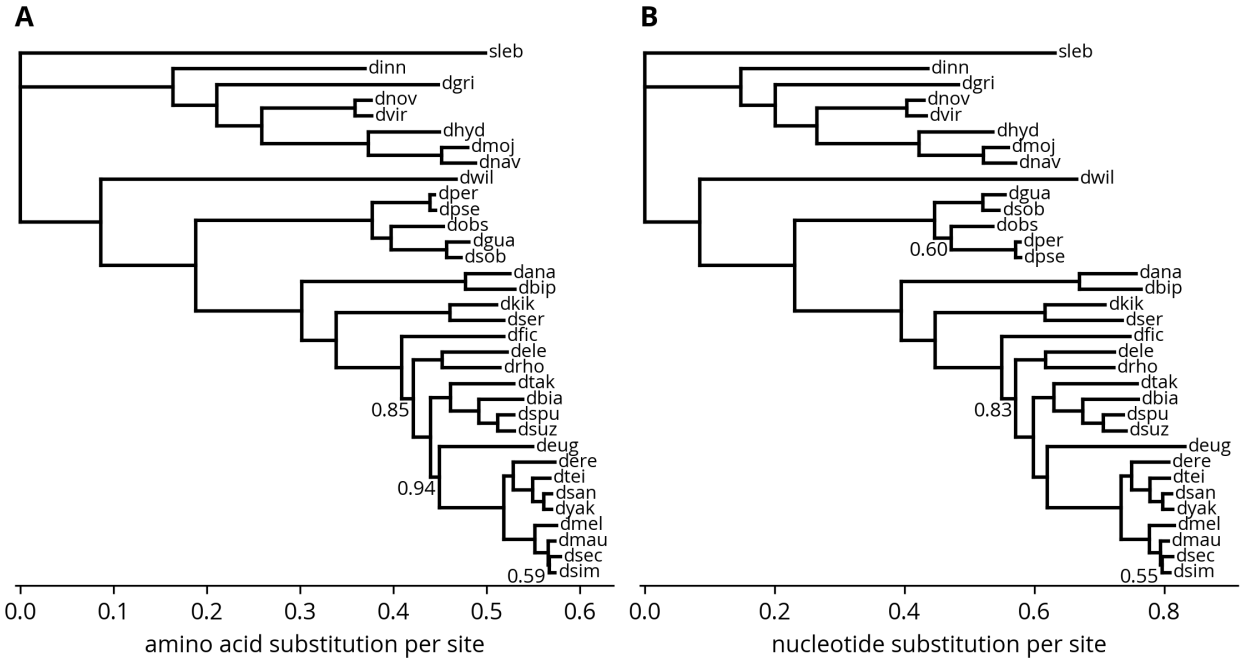

Figure 1.6. Phylogenetic tree of species. (A) Consensus tree from LG model fit to meta-alignments directly sampled from the original protein alignments. **(B)** Consensus tree from GTR model fit to meta-alignments sampled from "reverse translated" nucleotide alignments. Values at nodes are bootstrap percentages.

1.3 Discussion

1.3.1 Developments in genome assembly and annotation challenge existing methods of orthology inference

The orthologous groups and alignments yielded by this pipeline are a valuable resource for comparative studies of gene birth/death processes and protein evolution at the level of both entire proteomes and specific gene families in the *Drosophila* genus. To assist these efforts, the final alignments after curation and the labels from the "missing" phylo-HMM are provided as supplemental data. Although this work focused on single copy orthologs, other studies may require different subsets of orthologous groups that demand other pre-processing and alignment strategies. Therefore, we have included the orthologous groups and the initial alignments with and without non-representative sequences in the supplemental data as well. While we anticipate these resources will remain relevant in the near term, the trends that permitted this work to substantially improve on previous efforts will render them obsolete in the coming years as more *Drosophila* genomes are assembled and annotated. However, an authoritative and lasting set of orthologous groups and alignments is not the primary goal of this work. Instead, it serves as a case study in how dense taxonomic sampling and modern genome assembly and annotation pipelines present new opportunities and challenges to the traditional techniques for identifying and aligning orthologous groups.

For example, despite many additional pre-processing steps and other tweaks introduced by later authors, the basic framework of orthology inference by clustering the hit graph has remained largely unchanged in the past twenty years [49, 56–60, 62, 63]. This longevity is a testament to the robustness of the underlying idea that orthologous proteins should consistently identify each other as the most similar pairs between their genomes. Even as the number of genomes and their taxonomic density has increased dramatically, many orthology inference pipelines continue to use algorithms which were originally applied to sets of far fewer and more distantly related genomes. This mismatch in scale increases the chance of propagating annotation errors since only a small number of edges are needed to create or merge clusters. Thus, we instead applied a generalization of the triangle and connected components clustering methods called k-clique percolation where k is a tunable parameter that influences the tightness of a cluster. The optimal value of k for a given set of genomes is unclear and likely depends on the desired trade-off between sensitivity and specificity. Furthermore, k is not necessarily a global parameter and can instead depend on the properties of each connected component. For example, one possibility is to take an entire component as an orthologous group if its number of unique genes and unique species are equal since all the sequences are isoforms of a single set of genes. This would effectively set k equal to one for this component. Another approach is to make k an decreasing function of the density of edges, so sparser graphs are clustered more permissively. However, percolation theory or simulations may yield additional insights.

Another challenge is the annotation of multiple isoforms for a single gene. Though prior pipelines have generally selected the longest isoform as the representative before conducting the orthology searches, if the sequences do not share a common intron-exon structure this approach can introduce artifacts or other issues during alignment. Instead, as protein sequences are increasingly derived from or linked to genomic sequences, we sought to incorporate the full annotations into the orthology inference pipeline. This, however, created two additional complications. First, a single gene could have several associated orthologous groups if its isoforms belonged to different clusters. Second, a single orthologous group could have several isoforms of a single gene if its isoforms were clustered

together. In both cases, the presence of multiple sequences for a single gene creates ambiguities over which is the "primary" isoform. Since the first occurs at the level of orthologous groups, the orthologous groups were first grouped by the similarity of their parent genes using a graph-based strategy. Afterwards, a single representative is easily chosen as the group with the largest number of distinct species, though other criteria are possible. Since the second occurs within an orthologous group, the sequences were first aligned, and a representative for each gene was chosen as the sequence which was most concordant with this initial alignment.

The second major innovation in this work is its method for the refinement and trimming of alignments. Since sequences produced from automated annotation pipelines can contain long segments which are not homologous to most or any other sequences in their respective orthologous groups, their alignments may contain over-aligned or poorly supported regions which can introduce artifacts into downstream analyses. Thus, in refinement over-alignment is avoided by aligning the sequences in two stages. In the first highly conserved regions are aligned using a strong correction for over-alignment, and in the second more diverged regions are aligned with a weaker correction. This process usually prevents errors caused by long poorly supported segments without degrading the quality of the alignment. In trimming, a phylo-HMM is used to remove regions which are poorly supported by the phylogenetic consensus.

1.3.2 Comprehensive bioinformatic analyses of proteins will depend on splice-sensitive alignments

While the combination of these two steps yielded high-quality alignments that are suitable for further analyses, they are an *ad hoc* fix for underlying issues with the gene models and alignment algorithms. The most principled solution is to optimize or supplement the gene models using the initial alignments generated by the orthology inference pipeline, which is possible with tools such as OMGene or OrthoFiller [68, 81]. However, if preserving the original annotations is desired or necessary, the remaining possibility is to correct the alignments as we have done here. In fact, the errors we sought to address broadly stem from shortcomings of current alignment algorithms rather than errors in the sequences themselves. Though the scoring functions of modern multiple sequence alignment algorithms are complex, they are generally derived from models that penalize gaps with a linear or affine cost. As a result, they often interlace gaps with short, aligned segments rather than a single long gap. However, when the sequences are different isoforms of a single gene, their alignment will necessarily contain contiguous exon sized gaps. The same is true when aligning isoforms of diverged orthologs, though the relationship between their exons may be complex.

The most popular aligners for protein sequences (Clustal Omega [82], MAFFT [74], MUSCLE [83], T-Coffee [84]) do not include splice sites in their alignments, which makes them prone to aligning non-homologous exons. Current algorithms can easily be extended to incorporate splice sites by coding them as a new symbol and preventing alignment between splice sites and amino acids, which was recently implemented in the aligner, *Mirage* [85]. The biggest challenge in practice, however, is mapping a protein sequence to its genomic sequence to identify splice sites in the protein sequence. Although this information can in principle be derived from the GTF annotation files produced by the NCBI pipeline, annotating the splice junctions in the protein sequences themselves would facilitate splice-sensitive alignment.

These improvements would enhance rather than replace the phylo-HMM trimming method developed in this work. The model could easily be extended to include a state that outputs a splice symbol before transitioning to one of the states in the current architecture. This intermediate state

would increase the accuracy of state inference since a splice symbol followed by a phylogenetically discordant gap pattern would strongly signal a state 2 region. The association between state 2 and skipped exons can be made explicit by requiring that transitions to and from state 2 first proceed through the splice state. This of course depends on proper labeling of the training data, which would be trivial since the boundaries between exons would be marked by splice site symbols rather than inferred from gap patterns. Unfortunately, this would not allow the phylo-HMM to label extended exon boundaries as state 2 since they would not be bounded by splice symbols to the left and right. Accordingly, the phylo-HMM would need to permit transitions between state 3 and any other state to accommodate more complex splice variants and other annotation errors. Thus, this extended phylo-HMM would combine the strengths of splice-sensitive alignment with the more heuristic approach used here. Since state 2 inferences would necessarily correspond to skipped exons, they would be suitable for analyses of this form of alternative splicing. Though state 3 inferences would not directly correspond to specific biological process, they still have value as spatially and phylogenetically aware labels for trimming poorly supported segments from alignments.

The phylo-HMM could be further enhanced by expanding its emission distribution to include more symbols in the amino acid alphabet. This would allow it to better model observed substitution patterns between specific symbols, for example the high rate of exchange between gaps and glutamine residues caused by polyglutamine tracts. The transitions between amino acids could be parametrized with a published matrix such as LG [86], but the transitions between amino acids and gaps would be inferred from labeled data. It is unclear if the resulting gain in accuracy would justify the increased computational burden, however.

1.3.3 Accessible computational tools will facilitate future comparative studies

Though benchmarks are available for optimizing and comparing methods of orthology inference, the metrics are calculated over a set of reference genomes which are sparsely sampled over a broad taxonomic range, so it is unclear if they are informative for method designed to yield robust inferences when the genomes are highly related [87]. Furthermore, the heterogeneity of genome architectures and annotations may require quality assurance methods tailored to each set of genomes. Thus, there is likely no one-size-fits-all approach to orthology inference, and with many other standalone programs available for more standard use cases (Hieranoid [88], OMA standalone [89], OrthoFinder [90], OrthoInspector [91], Orthologer [92]), we have chosen not to package the code into an end-to-end pipeline. Instead, we have devoted considerable attention to organizing and documenting the code to make it accessible to a newcomer and thereby facilitate the adaptation of specific steps to similar projects as needed.

In contrast, though many HMM packages are available for the Python programming language, we found none were satisfactorily documented or contained tutorials to introduce HMMs and their APIs to a wide audience. We therefore refactored this code into a package available on PyPI and GitHub called Homomorph. The package itself only implements standard HMM algorithms, but the GitHub repository includes tutorials that introduce the API and implement training routines. Similar tutorials for machine learning libraries such as TensorFlow have undoubtedly fueled the application of neural networks across diverse fields, but HMMs are also powerful models that can be more appropriate when the data obey certain statistical or structural constraints. Thus, we hope this package and its accompanying tutorials will serve as an on-ramp to HMMs and spur their greater adoption by non-specialists.

Though databases of orthologous groups such as COGs [93], Ensembl Compara [94], EggNOG [95],

OMA [96], OrthoDB [92], OrthoInspector [97], and OrthoMCL [98] will continue to be useful for comparative studies across broad taxonomic ranges, the increasing speed at which high-quality genome assemblies and annotations are produced means no single database can encompass the most complete data. Furthermore, since many early comparative genomics studies spanned diverse branches of the tree of life, future research will likely prioritize taxonomic depth over breadth. Thus, custom sets of orthologous groups will grow more and not less common. Despite the challenges these developments pose, they also present new opportunities to bridge the gap between mutational and macroevolutionary processes.

1.4 Materials and methods

1.4.1 Sequence de-duplication and BLAST search parameters

The protein sequences for each annotation were de-duplicated by removing any sequences which had already appeared in association with the same gene. Thus, the first accession associated with a sequence and gene pair was the sequence's representative accession for the gene. BLAST+ 2.13.0 was used for the sequence similarity searches [33]. An E-value cutoff of 1 was used for the initial searches. However, this cutoff was lowered to 1E-10 during processing of the BLAST output.

1.4.2 Extraction of HSPs from BLAST output

To reduce the computational burden of merging HSPs into hits, the BLAST output was filtered to extract HSPs associated with the highest-scoring gene. The HSPs were first grouped by target protein, and the resulting groups were sorted in descending order by the bit score of their highest-scoring HSP. Iterating over the groups, all HSPs in a group were passed to the next step until the parent gene of the group was not the parent gene of the highest ranked group. This method collected all candidate HSPs for a target gene if the highest-scoring HSP within a group exceeded the highest-scoring HSP of the next best gene. This is in some senses an extension of the best hit criterion where hits are considered at the level of genes rather than proteins. If multiple genes tied for the highest-scoring HSP, the iteration stopped when the parent gene of the current group matched none of these highest-scoring genes.

1.4.3 Merging of HSPs into hits

HSPs were merged in two stages where the first combined non-overlapping HSPs, and the second combined the remaining HSPs. In the first stage, proceeding from highest to lowest bit score, HSPs were marked as "disjoint" if they did not overlap with any other HSP previously marked as disjoint. Although this greedy strategy did not necessarily yield the highest-scoring set of disjoint HSPs, it prioritized higher scoring HSPs. In the second stage, all disjoint HSPs were marked as "compatible," and proceeding from highest to lowest bit score the remaining HSPs were marked as compatible if the overlap with any other compatible HSP was no more than 50% of the length of either. The best hit for each query was chosen as the hit with the highest sum of bit scores from disjoint HSPs. The best hits were filtered by overlap and reciprocity criteria. The overlap criterion was applied first and required that 50% of residues in the query were aligned in compatible HSPs. This excluded false positives from conserved domains embedded in larger non-homologous proteins by ensuring the hits spanned a sufficient fraction of the query and target sequences. The reciprocity criterion required each query-target pair had a corresponding hit where the roles were reversed, which ensured there was no ambiguity in which target was the best match for the query.

1.4.4 Clustering by *k*-clique percolation

k-clique percolation was implemented in two steps. In the first, maximal cliques were identified. In the second, a percolation graph was constructed by defining edges between cliques if they had *k*-1 nodes in common. Clusters were the connected components of this second graph. The first step used the NetworkX implementation of a maximal clique algorithm. The second step used a modification of the NetworkX implementation of the *k*-clique community algorithm. The NetworkX implementation exhaustively finds all edges in the percolation graph. Since joining a *k*-clique community only requires that a clique has a single edge connecting it to that a community, this approach was needlessly expensive for large graphs. The custom implementation instead used a progressive approach where each clique was checked against a list of known communities, merging communities as necessary in each step.

The hit graph was sparse, so these algorithms were efficient when applied to its individual connected components. However, some components had a structure with many maximal cliques, which dramatically slowed the first or second step of the clique percolation algorithm. Thus, if either step exceeded 90 s, the process timed out, and the simpler *k*-core algorithm was used instead. Out of over 10,000 connected components, only seven timed out, and many of those contained highly dense clusters of histone sequences.

1.4.5 Addition of paralogs to orthologous groups

The protein sequences for each annotation were searched against themselves with the same settings as for the inter-genome searches. The resulting output was processed identically except the HSPs were not filtered using the best gene criterion. Thus, all HSPs for each query were merged into hits. The best hit for each query and target gene was chosen as the hit with the highest sum of bit scores from disjoint HSPs. (Grouping by target gene ensured only the highest-scoring isoform was selected.) Query-target pairs whose hits exceeded the maximum bit score for all inter-genome hits associated with that query and passed the overlap and reciprocity filters were designated as paralogous pairs. The orthologous groups were supplemented with paralogs by adding the paired sequences for each of the original members of the orthologous group.

1.4.6 Initial alignment and selection of representative sequences

The sequences in each orthologous group were aligned using MAFFT 7.490 with the following settings: --globalpair --maxiterate 1000 --thread 1 --anysymbol --allowshift --leavegappyregion --unalignlevel 0.4 [74]. Representative sequences for each gene were selected by maximum likelihood according to binary profiles constructed from these alignments. First each sequence was coded into gap and non-gap symbols. The sequences were grouped by gene, and for each group and position if at least one sequence was aligned in the group, the group contributed one count for the non-gap symbol to the profile at that position. Otherwise, the group contributed a count for the gap symbol at that position. To account for the phylogenetic dependencies between sequences, the counts were weighted according to a Gaussian process over the GTR2 consensus tree described in the section on inferring species trees [99]. If a species had multiple genes in the orthologous group, the species weight was divided evenly among them. Each coded sequence was scored according to this profile, and the maximum likelihood sequence for each gene was selected as its representative. By assigning a non-gap count to groups and positions where at least one sequence was aligned, the profile prioritized the selection of sequences with the fewest gaps that best matched the consensus alignment. Since this scheme can cause a sequence to score negative infinity if it has a gap at

a position where every group has at least one aligned sequence, the profile was initialized with a pseudocount of 0.005 for the gap and non-gap symbols at each position.

1.4.7 Alignment refinement

The representative sequences in the single copy orthologous groups were aligned with the same settings as described in the previous section except a_{max} was set to 0.7. A binary profile was created from the alignment using Gaussian process sequence weighting as described in the section on selecting representative sequences. (Because the orthologous groups were single copy and contained only representative sequences, each sequence received the full weight associated with its species.) The binary profile was converted into a binary mask by identifying where the weighted fraction of non-gap symbols exceeded 0.5. The binary mask was closed with a structuring element of size three, and highly conserved regions were identified as the contiguous intervals of this closed mask with a minimum length of 10. Diverged regions were taken as the complement of the highly conserved regions. For each diverged region, the corresponding segments of the sequences in the initial alignment were extracted and aligned with a_{max} set to 0.4. The resulting sub-alignments were stitched into the initial alignment.

1.4.8 Alignment curation

The alignments were coded into gap and non-gap symbols to simplify the emission distributions. The "insertion" phylo-HMM was composed of the four hidden states described in the main text. The emission distributions for each consisted of two components which modeled the gap pattern and the propensity for those patterns to remain constant ("gap stickiness"), respectively. The first component was a two-state Markov process which was in turn composed of two subprocess. The first was a phylogenetic process on the on the GTR2 consensus tree described in the section on inferring species trees, and the second was jump process at the tips. The second component was a beta-Bernoulli distribution on the number of symbols which were constant between subsequent columns. The "missing data" phylo-HMM was composed of two hidden states which were both parameterized with the same two-state, two component Markov process as the insertion phylo-HMM. However, the emission probabilities were calculated as the posterior probability of the observed symbol given the data rather than the probability of the data. Only the alignments of the single copy orthologous groups were curated, so each tip in the species tree corresponded to a single sequence in the alignment.

The likelihoods of phylogenetic trees were efficiently calculated with Felsenstein's pruning algorithm, and all HMM algorithms were implemented with custom code which is available as the package Homomorph on PyPI [100]. The insertion phylo-HMM was trained on 47,387 manually labeled columns in 14 alignments, and the missing data phylo-HMM was trained on 67,001 manually labeled positions in 23 sequences in 11 unique alignments (Fig. A4, Fig. A6). Because maximum-likelihood estimation of the model parameters yielded posterior decoding curves which toggled between hidden states too rapidly, the models were instead trained discriminatively [101]. The difference, briefly, is maximum-likelihood estimation finds the parameters that best reproduce the observed distributions whereas discriminative training finds the parameters that minimize prediction error. Discriminatively trained models typically perform better in practice since real-world data are rarely fully described by the distribution specified by the model.

The posterior distributions over states were calculated for each alignment using the trained insertion phylo-HMM. Regions with a high probability of state 2 or 3 were candidates for trimming. However,

because the probability of a state can change rapidly or gradually depending on the local context, a simple cutoff would not necessarily define the boundaries of these regions as the columns where the gap pattern changed most abruptly. Instead, the following algorithm was used. First, a high cutoff defined a "seed" region. The left and right endpoints of the seed were then expanded both inwards and outwards to define two intervals from which boundaries were selected. The outward expansion halted when the probability or its derivative was below two distinct thresholds, respectively. The inward expansion halted when the derivative was below a different threshold. The left and right boundaries were chosen as the columns in each interval with the maximum product between the derivative and the change in the gap profile between columns. The gap profile was calculated as the number of gaps in each column using Gaussian process sequence weighting as described in the section on selecting representative sequences. By combining where the model's confidence changed rapidly with the observed change in the gap pattern, this method generally selected reasonable boundaries.

States 2 and 3 have distinct characteristics which required different trimming strategies. Regions with a high probability of state 3 were handled first. Because the long poorly supported segments in state 3 regions were sometimes aligned to highly conserved columns or short segments in other sequences, trimming columns entirely would remove these segments from the other sequences even if they would not qualify as long and poorly supported themselves. Thus, regions with high state 3 probabilities were trimmed at the level of individual sequences rather than entire columns using the following method. First, the probability of state 3 for columns with a gap profile value less than or equal to 0.1 was set to 0 to break long poorly supported segments aligned to highly conserved columns into separate regions. Regions were defined with the previously described algorithm using high and low cutoffs of 0.75 and 0.01, respectively. The outer and inner derivative cutoffs were both 0.001. The mean number of non-gap symbols in a region was calculated using Gaussian process sequence weighting as described in the section on selecting representative sequences. (The sequences with the five most non-gap symbols were also excluded to not bias the estimate with long poorly supported segments.) The final mean μ was taken as the minimum of this value and two. A cutoff k, derived from a geometric model of the number of non-gap symbols and a significance level α, was calculated using the equation $k = \log(\alpha)/\log(1-p) - 1$ where $p = \frac{1}{\mu+1}$ and $\alpha = 0.01$. Any sequence whose number of non-gap symbols in the region equaled or exceeded this value was trimmed by replacing all non-gap symbols with gaps.

To trim the remaining state 2 regions, the posterior probability of state 2 was added to a modified state 3 probability which was set to zero for any state 3 regions identified in the previous step. This ensured that any regions which were intermediate between state 2 and 3 were included. Regions were defined from this combined probability using the algorithm described previously except with a high probability cutoff of 0.9 instead of 0.75. The posterior probabilities from the missing data phylo-HMM were converted into state assignments using a similar method. However, the initial seeds were defined with a cutoff of 0.75, and the seeds were expanded outward to the first non-gap symbol or until the posterior probability of the "missing data" state was below 0.05. These assignments, which are available in the supplementary data, can be used to filter segments or entire sequences from downstream analyses.

1.4.9 Inference of species trees

The orthology inference pipeline was first repeated with the outgroup species *Scaptodrosophila lebanonensis*. Orthologous groups with one sequence for each species were aligned, and 100 meta-

alignments were constructed by randomly sampling 10,000 columns from these 9,435 alignments. (The alignments were not refined before sampling.) To determine the effect of invariant columns and gaps, two sampling strategies were used where invariant columns were allowed or disallowed and the maximum fraction of gaps was set at 0, 50, and 100%. Their combination yielded six different sets of meta-alignments. A tree was fit to each meta-alignment with the LG substitution model [86], four discrete gamma rate categories [102], and optimized state frequencies using IQ-TREE 1.6.12 [103]. If the sampling strategy allowed invariant columns, an invariant rate category was included. The resulting trees from each set were merged into a majority consensus tree (Fig. A8). All figures are derived from the maximum 50% gap fraction meta-alignment set unless otherwise noted.

To fit trees using the GTR model of nucleotide substitution, the protein alignments were converted to nucleotide alignments using the corresponding coding sequences in the genome annotations. Some protein sequences were "low quality," meaning their coding sequences contained frameshifts, premature stop codons, or other errors even though they were strong hits to known protein-coding genes. The NCBI annotation pipeline corrects some of these defects in the protein sequences, which can complicate a simple "reverse translation" of the alignment. After rejecting alignments where the expected translation from a coding sequence differed from its corresponding protein sequence, 3,425 alignments remained. Consensus tree were derived from meta-alignments sampled from these alignments using the approach described previously except the GTR model was used in place of the LG model.

To fit trees using the two-state GTR model of substitution, the protein alignments were first coded into gap or non-gap symbols. As before, 100 meta-alignments were constructed from these coded alignments for each sampling strategy. In this case, only the presence of invariant columns was varied, yielding two sets of meta-alignments. Trees were fit using the GTR2 model with no rate categories. An invariant category, however, was included if invariant columns were allowed. Since the bootstrap confidences were sometimes lower than 50%, the resulting trees from each set were merged into a loose consensus tree to prevent multifurcations (Fig. A9).

1.4.10 Code and data availability

The code used to produce the results and analyses is available at `https://github.com/marcsingleton/orthology_inference2023`. HMM algorithms were implemented in the standalone package Homomorph which is available at `https://github.com/marcsingleton/homomorph` and on the Python Package Index (PyPI). The following Python libraries were used: matplotlib [104], NumPy [105], pandas [106], and SciPy [107]. Relevant output files are available in the supporting information. There are no primary data associated with this manuscript. All primary data are available from publicly accessible sources described in their corresponding sections.

CHAPTER 2

Evolutionary analyses of IDRs reveal patterns of conserved features

Abstract

Intrinsically disordered regions (IDRs) are segments of proteins without stable three-dimensional structures. As this flexibility allows them to interact with diverse binding partners, IDRs play key roles in cell signaling and gene expression. Despite the prevalence and importance of IDRs in eukaryotic proteomes and various biological processes, associating them with specific molecular functions remains a significant challenge due to their high rates of sequence evolution. However, by comparing the observed values of various IDR-associated properties against those generated under a simulated model of evolution, a recent study found most IDRs across the entire yeast proteome contain conserved features. Furthermore, it showed clusters of IDRs with common "evolutionary signatures," *i.e.* patterns of conserved features, were associated with specific biological functions. To determine if similar patterns of conservation are found in the IDRs of other systems, in this work we apply a series of phylogenetic models to over 8,500 orthologous IDRs identified in the *Drosophila* genome to dissect the forces driving their evolution. By comparing models of constrained and unconstrained continuous trait evolution using the Brownian motion and Ornstein-Uhlenbeck models, respectively, we identify specific clusters of IDRs with shared patterns of constraint. As in yeast, these clusters are enriched for proteins with specific functional annotations, which suggests the preservation of distributed features and their associated functions is a widespread mechanism of IDR evolution.

2.1 Introduction

Intrinsically disordered regions (IDRs) are segments of proteins which lack stable three-dimensional structures and instead exist as ensembles of rapidly interconverting conformations. As a result of this structural heterogeneity, IDRs can interact with diverse binding partners. Often these interactions have high specificity but moderate affinity, which permits the efficient propagation of signals by rapid binding and dissociation [22, 108]. Furthermore, as IDRs readily expose their polypeptide chains, they are enriched in recognition motifs for post-translational modifications which allow environmental or physiological conditions to modulate their interactions. Accordingly, IDRs often act as the "hubs" of complex signaling networks by integrating signals from diverse pathways and coordinating interactions [20, 21]. However, as IDRs are ubiquitous in eukaryotic proteomes, with estimates of the fractions of disordered residues in the human, mouse, and fruit fly proteomes ranging between 22 and 24% [109, 110], they are involved in diverse processes [17] including transcriptional regulation [23] and the formation of biomolecular condensates [111].

Despite the prevalence and importance of IDRs in eukaryotic proteomes, associating them with specific molecular functions or biological processes remains a significant challenge. The sequences

of IDRs are generally poorly conserved, so traditional bioinformatics approaches which rely on the conservation of amino acid sequences to identify homologous proteins and transfer annotations between them are largely unsuccessful when applied to IDRs. However, several recent studies have demonstrated evidence that IDRs are constrained to preserve "distributed features" such as flexibility [37], chemical composition [38], net charge [39], or charge distribution [40]. Because many sequences can yield a region with a specific composition, for example, this mode of constraint uncouples an IDR's fitness from its strict sequence of amino acids. Furthermore, in contrast to folded regions whose precise contacts and packing geometries are easily disrupted by amino acid substitutions, distributed features are robust to such changes, as individual residues only weakly contribute to a region's fitness. For example, a mutation at one site in an IDR that changes its net charge is easily reversed by subsequent compensatory mutations elsewhere in the region. Thus, under this model the sequences of IDRs can rapidly diverge and still preserve their structural or functional properties.

This form of selective constraint can also describe the evolution of more "localized" features in IDRs such as short linear motifs (SLiMs). Because SLiMs are composed of fewer than 12 residues, they form limited interfaces that frequently mediate the transient binding events involved in signaling pathways [19]. Accordingly, they are highly enriched in IDRs, which provide an accessible and flexible scaffold for these interactions [112, 113]. While some SLiMs in IDRs are strongly conserved at specific positions, these constitute a small fraction of disordered residues, estimated at roughly 17% in the yeast proteome [114]. Instead, as SLiMs are compact and often highly degenerate at some positions, they can arise de novo from a small number of mutations and therefore have high rates of turnover. Furthermore, when IDRs contain multiple copies of a motif that jointly mediate a high-avidity interaction [19] or a graded response to a signal via the accumulation of multiple phosphorylations [22, 115], the individual motifs are under weak selective constraints. As a result, though SLiMs are encoded by specific sequences, in some contexts they may evolve as distributed features that characterize IDRs as a whole rather than specific sites within them [116].

The initial studies demonstrating evidence of constraint were generally restricted to specific features or proteins. However, by comparing the observed values of various IDR-associated properties against those generated under a simulated model of evolution, Zarin *et al.* showed most IDRs across the entire yeast proteome contain conserved features. Furthermore, they identified clusters of IDRs with common "evolutionary signatures," *i.e.* patterns of conserved features, which were associated with specific biological functions. This analysis for the first time provided a global view of the relationship between sequence and function in IDRs. A follow-up study then expanded on this initial finding by applying techniques from machine learning and statistics to predict the functions of individual IDRs using their evolutionary signatures [117].

However, no known subsequent studies have determined if similar patterns of conservation are found in the IDRs of other systems. As another foundational model organism with abundant genomic information across many evolutionary lineages [41–44], the fruit fly, *Drosophila melanogaster*, is a natural choice for subsequent investigation. Furthermore, given its complex multicellular development process and shared signaling pathways with humans, the findings of such a study would significantly advance our understanding of the role of IDRs in gene regulation as well as human health and disease. The concordance of these results with the previously identified IDR clusters would also have profound implications for the broader mechanisms of IDR evolution. For example, the absence of global patterns of evolutionary signatures across IDRs in *Drosophila* would suggest they are property of IDRs which is unique to yeast. In contrast, the identification of clusters similar

to those in yeast would indicate the existence of a taxonomy of IDRs which is conserved across the tree of life. The latter result would represent a significant step towards the creation of resources for the classification of IDRs analogous to those for folded domains such as Pfam [35], CATH [118], or SCOP [119, 120].

Therefore, in this work we apply a series of phylogenetic models to a set of orthologous IDRs identified in the *Drosophila* genome to dissect the forces driving their evolution. Our analyses span multiple levels, ranging from the sequences that compose these regions to the distributed features that characterize them as a whole. For the latter, though the previous approach relied on simulations to generate the null distribution for a hypothesis of no constraint, we instead leverage a fully statistical phylogenetic comparative framework [121]. By comparing models of constrained and unconstrained continuous trait evolution, *i.e.* the Brownian motion and Ornstein-Uhlenbeck models, respectively, we can demonstrate evidence of selective constraint on features independent of any assumptions about the underlying process of sequence evolution. However, we also propose hybrid approaches that combine simulations with phylogenetic comparative methods to test increasingly refined models of IDR evolution. We find that IDRs exhibit unique patterns of amino acid substitution and that in some proteins disorder itself is a dynamically evolving property. Furthermore, though IDRs are broadly unconstrained along several axes of feature evolution, we identify specific clusters of IDRs with shared patterns of constraint. As in yeast, these clusters are enriched for proteins with specific functional annotations, which suggests the preservation of distributed features and their associated functions is a widespread mechanism of IDR evolution.

2.2 Results

2.2.1 IDRs are shorter and more divergent than non-disordered regions

We identified regions with high levels of inferred intrinsic disorder in over 8,500 alignments of single copy orthologs from 33 species in the *Drosophila* genus using the disorder predictor AUCPreD [122]. To highlight the unique features of IDR evolution in subsequent analyses, we also extracted a complementary set of regions with low levels of inferred disorder. Both sets were filtered on several criteria, including the lengths of their sequences and their phylogenetic diversity, which yielded 11,445 and 14,927 regions, respectively, from 8,466 unique alignments. In the subsequent discussion, we refer to these sets as the "disorder" and "order" regions, respectively. To investigate the differences in basic sequence statistics between the two region sets, we first generated histograms from the average length of each region (Fig. B1). Although both distributions span several orders of magnitude, the order regions are generally longer than the disorder regions, with means of 105 and 245 residues, respectively. We then quantified the sequence divergence in each region by fitting phylogenetic trees to the alignments using amino acid and indel substitution models. The average rates of substitution are significantly larger in the disorder regions, demonstrating that while both sets contain conserved and divergent regions, IDRs are enriched in more rapidly evolving sequences (Fig. B1).

2.2.2 IDRs have distinct patterns of residue substitution

To gain insight into the substitution patterns of amino acid residues in the disorder and order regions, we fit substitution models to meta-alignments sampled from the respective regions. These models are probabilistic descriptions of sequence evolution and are parameterized in terms of the one-way rates of change from one residue to another. Thus, the rates are not necessarily equal for

a given pair when the initial and target residues are swapped. For example, the rate of change of valine to tryptophan can be distinct from that of tryptophan to valine. In practice, substitution models are typically constrained to fulfill a condition called time-reversibility, as this converts a difficult multivariate optimization of the tree's branch lengths into a series of simpler univariate optimizations [100]. A common method for fulfilling this condition is parameterizing the model in terms of a frequency vector, $\boldsymbol{\pi}$, and an exchangeability matrix, S. The frequency vector determines the model's expected residue frequencies at equilibrium, meaning the model dictates that all sequences eventually approach this distribution, no matter their initial composition. The exchangeability matrix is symmetric ($s_{ij} = s_{ji}$) and encodes the propensity for two residues to interconvert. Because the rate of change from residue i to residue j is given by $r_{ij} = s_{ij}\pi_j$, higher exchangeability coefficients yield higher rates of conversion. Thus, exchangeability coefficients are frequently interpreted as a measure of biochemical similarity between residues.

To highlight the differences in patterns of residue substitution between the disorder and order regions, the parameters in each model are directly compared in Fig. 2.1, beginning with the frequency vectors. The disorder regions show an enrichment of "disorder-promoting" residues such as serine, proline, and alanine, and a depletion of hydrophobic and bulky residues such as trytophan and phenylalanine (Fig. 2.1A). The exchangeability matrices fit to the disorder and order regions have similar overall patterns of high and low coefficients (Fig. 2.1B-C). However, the log ratios of the disorder to the order exchangeability coefficients show clear differences within and between the disorder-enriched and -depleted residues. The disorder-enriched residues are less exchangeable with each other, whereas disorder-depleted residues are more exchangeable with each other and with disorder-enriched residues (Fig. 2.1D). Likewise, we observe a trend in the log ratios of the rate coefficients where the coefficients above the diagonal are generally positive, and those below the diagonal are generally negative. As the coefficients model the one-way rates of substitution between residues with the vertical and horizontal axes indicating the initial and target residues, respectively, this suggests a net flux towards a more disorder-like composition. However, the coefficients between the disorder-depleted and -enriched classes of residues for both the exchangeability and rate matrices should be interpreted with caution, as they are estimated with a high amount of uncertainty (Fig. B5-B6).

2.2.3 Intrinsic disorder is poorly conserved in some proteins

Though the substitution models reveal specific patterns of evolution at the level of individual residues, the large amounts of sequence divergence between many orthologous IDRs implies their evolution is not well-described by fine-scale models of residue substitution. Given the growing evidence that IDRs are constrained to conserve distributed properties, we instead turned towards characterizing their evolution in terms of 82 disorder-associated "molecular features" obtained from the previous study of IDRs in the yeast proteome. However, before conducting an in-depth analysis of these features, we examined the disorder score traces in greater detail and were struck by the significant variability between species. For each residue in the input sequence, AUCPreD returns a score between 0 and 1 where higher values indicate higher confidence in a prediction of intrinsic disorder. In some alignments, the scores vary by nearly this entire range at a given alignment position even when there is a relatively high level of sequence identity (Fig. 2.2A).

To better understand the relationship of this variability to differences in the regions' biophysical properties, we sought to correlate the average disorder score of the segments in a region with their molecular features. However, as the sequences are not independent but instead related by a

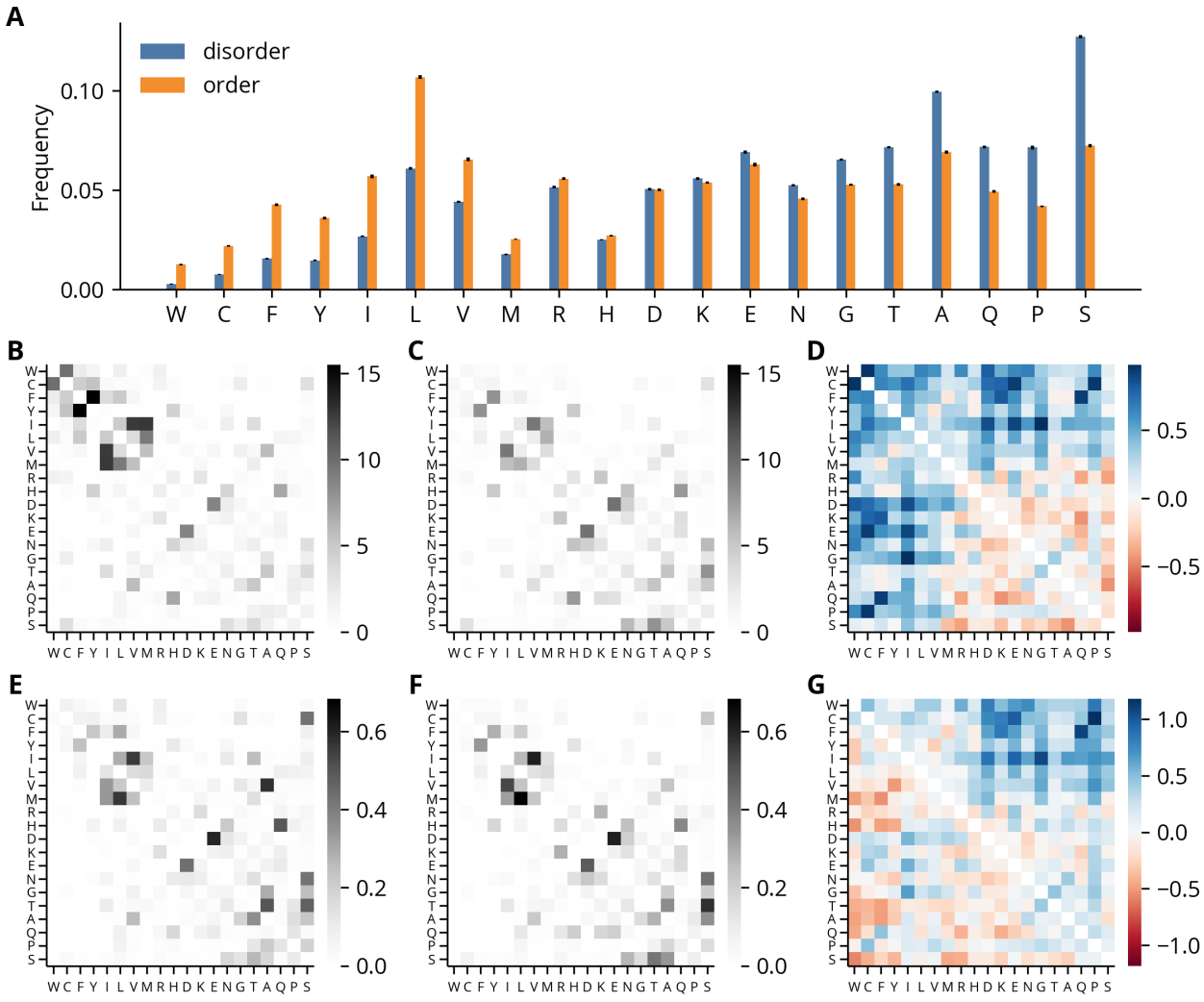

Figure 2.1. Amino acid substitution models fit to disorder and order regions. **(A)** Amino acid frequencies of substitution models. Amino acid symbols are ordered by their enrichment in disorder regions, calculated as the disorder-to-order ratio of their frequencies. Error bars represent standard deviations over models fit to different meta-alignments ($n = 25$). **(B-C)** Exchangeability coefficients of disorder and order regions, respectively, averaged over meta-alignments. **(D)** $\log_{10}$ disorder-to-order ratios of exchangeability coefficients. **(E-F)** Rate coefficients of disorder and order regions, respectively, averaged over meta-alignments. The vertical and horizontal axes indicate the initial and target amino acids, respectively. **(G)** $\log_{10}$ disorder-to-order ratios of rate coefficients.

hierarchical structure which reflects their evolutionary relationships, any features derived from them are unsuitable for direct use in many standard statistical procedures. In the most severe cases, traits derived from clades of closely-related species can effectively act as duplicate observations, which can yield spurious correlations. We therefore applied the method of contrasts to both the scores and the features. This algorithm takes differences between adjacent nodes in the phylogenetic tree relating the species to generate "contrasts," which, under some general assumptions of the underlying evolutionary process, are independent and identically-distributed and therefore appropriate for use in correlation analyses. The resulting feature contrasts have varying degrees of correlation with the score contrasts (Fig. 2.2B-C). Some, like isopoint, are uncorrelated, but most are significantly,

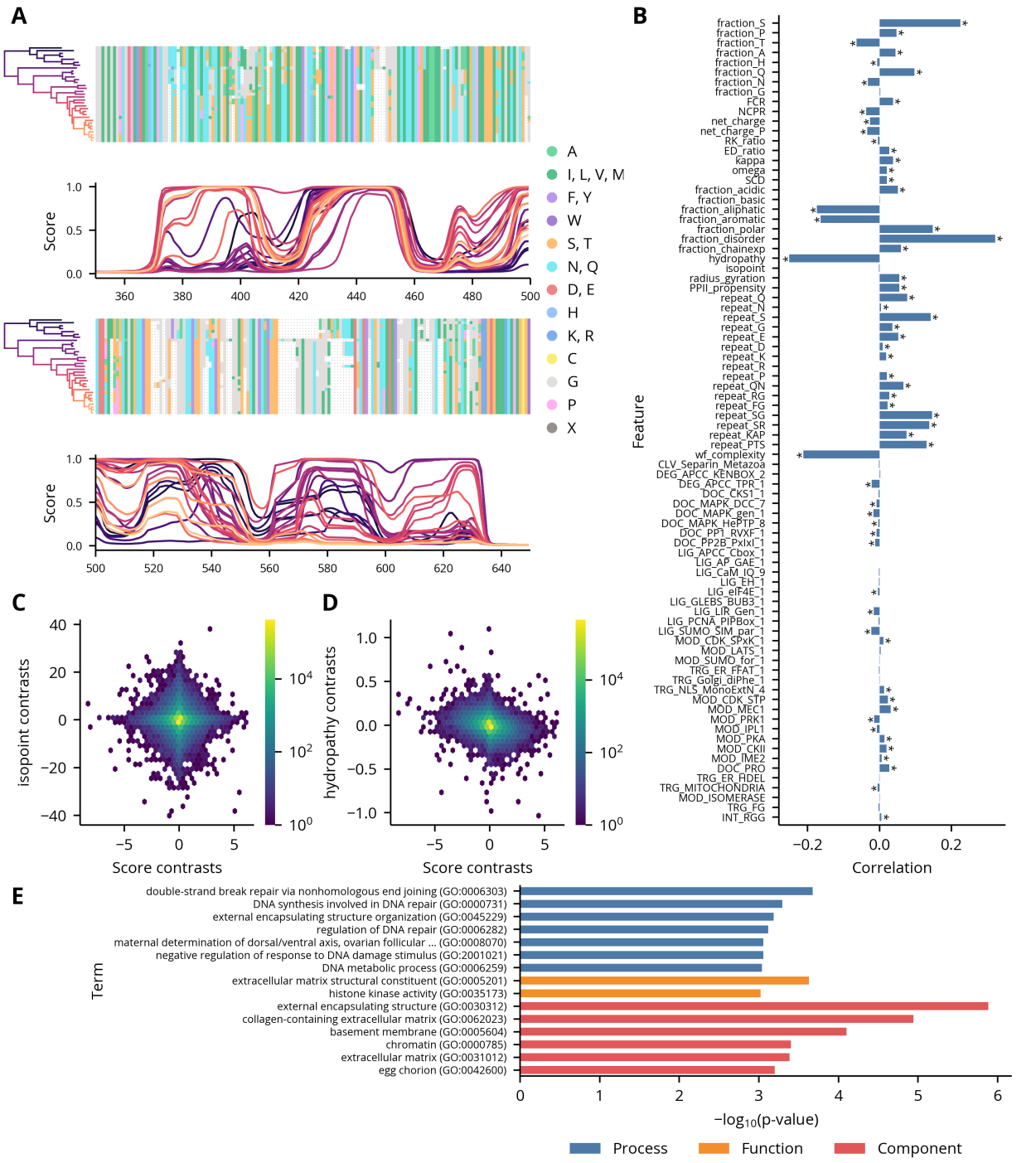

Figure 2.2. Analyses of disorder scores. **(A)** Example region in the alignment of the sequences in orthologous group 07E3 with their corresponding disorder scores. Higher scores indicate a higher probability of intrinsic disorder. Disorder score traces are colored by the position of their associated species on the phylogenetic tree. **(B)** Correlations between disorder scores and feature contrasts in regions. Asterisks indicate statistically significant correlations as computed by permutation tests ($p < 0.001$). **(C-D)** Example scatter plots showing correlations given in panel B. **(E)** GO term analysis of regions with rapidly evolving disorder scores. Only terms where $p < 0.001$ are shown.

if weakly, correlated. In general, the strongest correlations are observed for features which have a direct biophysical relationship to the presence or absence of disorder, such as disorder_fraction or hydrophobicity. Interestingly, the correlations with many motifs were statistically significant, though small in magnitude relative to the non-motif features. However, a more detailed analysis of this observation is presented in the discussion. To determine if regions with rapidly evolving disorder scores are associated with particular functions, processes, or compartments, we then extracted the regions in the upper decile of the rate distribution and performed a term enrichment analysis on their associated annotations (Fig. B7). The most significant terms are generally related to DNA repair or extracellular structure, which suggests these processes and components are enriched in proteins whose structural state is rapidly evolving (Fig. 2.2E).

2.2.4 IDRs have three axes of unconstrained variation

Having calculated the features associated with the sequence segments composing each region in our data set, we then sought to determine if their distributions contained any global structure which would enable us to identify classes with distinct biophysical or functional properties. These distributions are generated by a complex underlying evolutionary process which reflects the combined effects of selection, drift, and mutation. However, to leverage a statistical framework to infer the properties of this process, we fit Brownian motion (BM) models to the features calculated from the segments in each region. BM is a simple model of evolution where continuous traits change through a series of small, undirected steps. Thus, the traits accumulate variation at a constant rate over time but do not on average deviate from their original values. BM models are therefore specified by two parameters: a rate, which describes the speed at which trait variation accumulates, and a root, which describes the ancestral trait value.

We then applied principal components analyses (PCAs) to visualize the major axes of variation of the root and rate parameters for each feature and region. A difficulty with a direct analysis of the parameter estimates, however, is PCAs are sensitive to differences in scaling between variables, and some features have dramatically different intrinsic scales. For example, many compositional features, like fraction_S, are restricted to the interval [0, 1], whereas SCD is unbounded and can vary from negative to positive infinity. As a result, SCD is responsible for a significant fraction of the overall variance in both parameter distributions (Fig. B8-B9). Therefore, we first normalized the parameters associated with each feature by transforming them into z-scores relative to their proteome-wide distributions.

The first two principal components of the root distributions show little overall structure, though there is a slight enrichment of regions along two axes that correlate with acidic and polar features, respectively (Fig. 2.3). Likewise, the projections of the rates onto the first two components are largely distributed along the first principal component (Fig. 2.4A). This and the variable amounts of sequence divergence in the regions led us to suspect the first principal component was a measure of the overall rate of sequence evolution. Plotting the first principal component against the sum of the average amino acid and indel rates as measured by substitution models revealed a strong association (Fig. 2.4B). We then projected the rates along second and third principal components to determine if these higher order components contained any additional structure. The resulting distribution is roughly triangular and contains three major axes of variation, corresponding to rapid changes in the regions' proportions of acidic, glutamine, and glycine residues (Fig. 2.4C-D). Inspection of regions selected along these axes confirmed the high rates of evolution of these features (Fig. 2.4E-G). Furthermore, we observe a similar distribution when the rates of the order

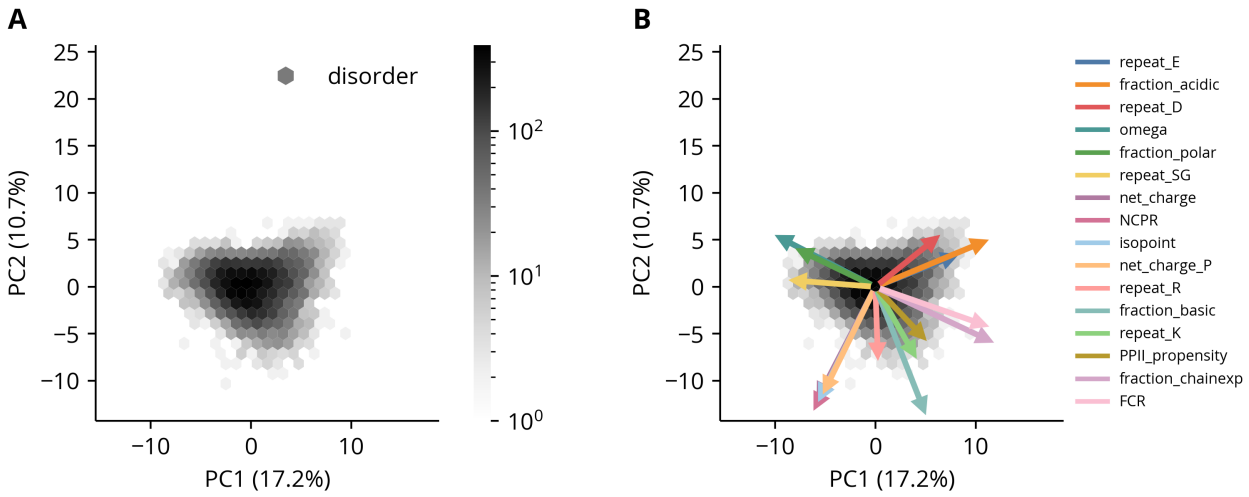

Figure 2.3. PCA of disorder regions' feature roots. (A) The first two PCs of the disorder regions' feature root distributions. The explained variance percentage of each component is indicated in parentheses in the axis labels. **(B)** The same plot as panel A with the projections of original variables onto the components shown as arrows. Only the 16 features with the largest projections are shown. Scaling of the arrows is arbitrary.

regions were projected along their second and third principal components, which suggests a lack of constraint along these axes is a general property of rapidly evolving proteins (Fig. B10).

2.2.5 A model of constrained evolution reveals patterns of conserved features

Though the BM process permits the inference of the rates of feature evolution after accounting for the phylogenetic relationships between species, it does not directly test for their conservation. In fact, under the BM model, trait variation is unconstrained and will increase without bound over time. Instead, evidence of conservation requires comparison to a model where trait variation is constrained. A common choice for modeling the effect of selection on the evolution of a continuous trait is the Ornstein-Uhlenbeck (OU) model. The OU model is similar to the BM model where a trait accumulates variation through a series of small, undirected steps. However, it differs in that the trait is also attracted towards an optimal value where the attraction is proportional to a parameter α and the trait's distance from this value. Under an additional assumption of stationarity that ensures parameter identifiability and estimate consistency, the OU model is therefore specified with three total parameters: the optimal value, the fluctuation magnitude, and the selection strength [123, 124]. While the first two parameters are analogous to the root and rate parameters in the BM model, respectively, the selection strength has no equivalent.

We therefore fit OU models to the features calculated from the segments in each region to detect evidence of their conservation. A strength of probabilistic models of trait evolution is they permit the use of standard statistical methods to compare the support for different hypotheses. Thus, the goodness of fit of the OU model relative to that of the BM model is a measure of the evidence for selective constraint. However, because the OU model is specified with an additional parameter and has a greater capacity to fit the data, we compared their fits using the difference in the Akaike information criterion (AIC), which accounts for the model complexity, rather than the likelihood ratio. We chose not to treat these differences in a strict statistical sense but instead as qualitative "evolutionary signatures" as in Zarin *et al.* [125]. Accordingly, we clustered the signatures to identify

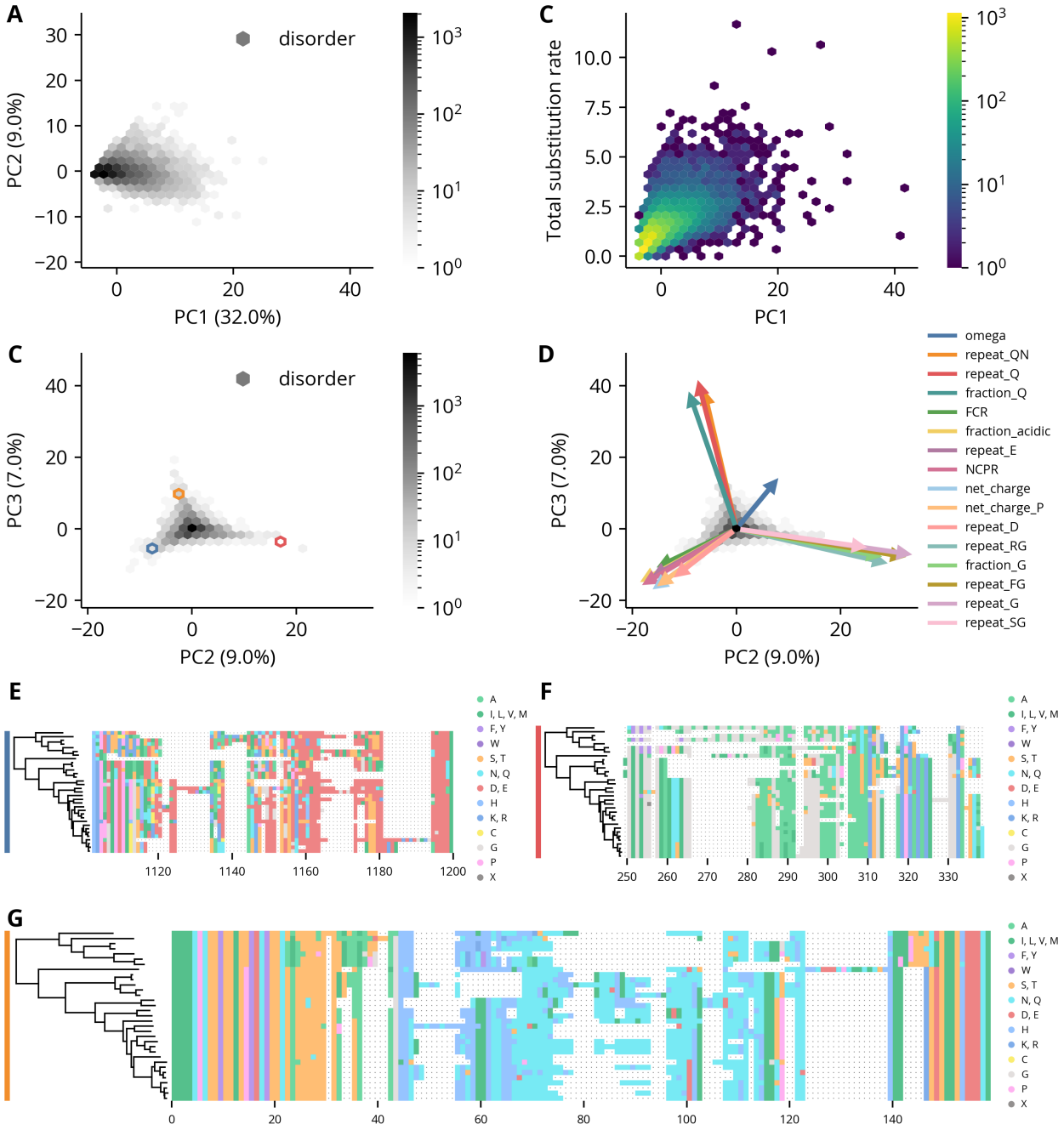

Figure 2.4. PCA of disorder regions' feature rates. **(A)** The first two PCs of the disorder regions' feature rate distributions. The explained variance percentage of each component is indicated in parentheses. **(B)** Scatter plot of the disorder regions' feature rates along the first PC against the sum of the average amino acid and indel substitution rates in those regions. **(C)** The second and third PCs of the disorder regions' feature rate distributions. The explained variance percentage of each component is indicated in parentheses in the axis labels. **(D)** The same plot as panel C with the projections of original variables onto the components shown as arrows. Only the 16 features with the largest projections are shown. Scaling of the arrows is arbitrary. **(E-F)** Example alignments of disorder regions from the orthologous groups 0A8A, 3139, 04B0, respectively. The colored bars on the left indicate the hexbin containing that region in panel C.

patterns of feature conservation across the proteome. To ensure the clusters were enriched in regions with a high likelihood of feature conservation despite low levels of sequence identity, we restricted this analysis to regions with a minimum amount of divergence as measured by substitution models (Fig. B11).

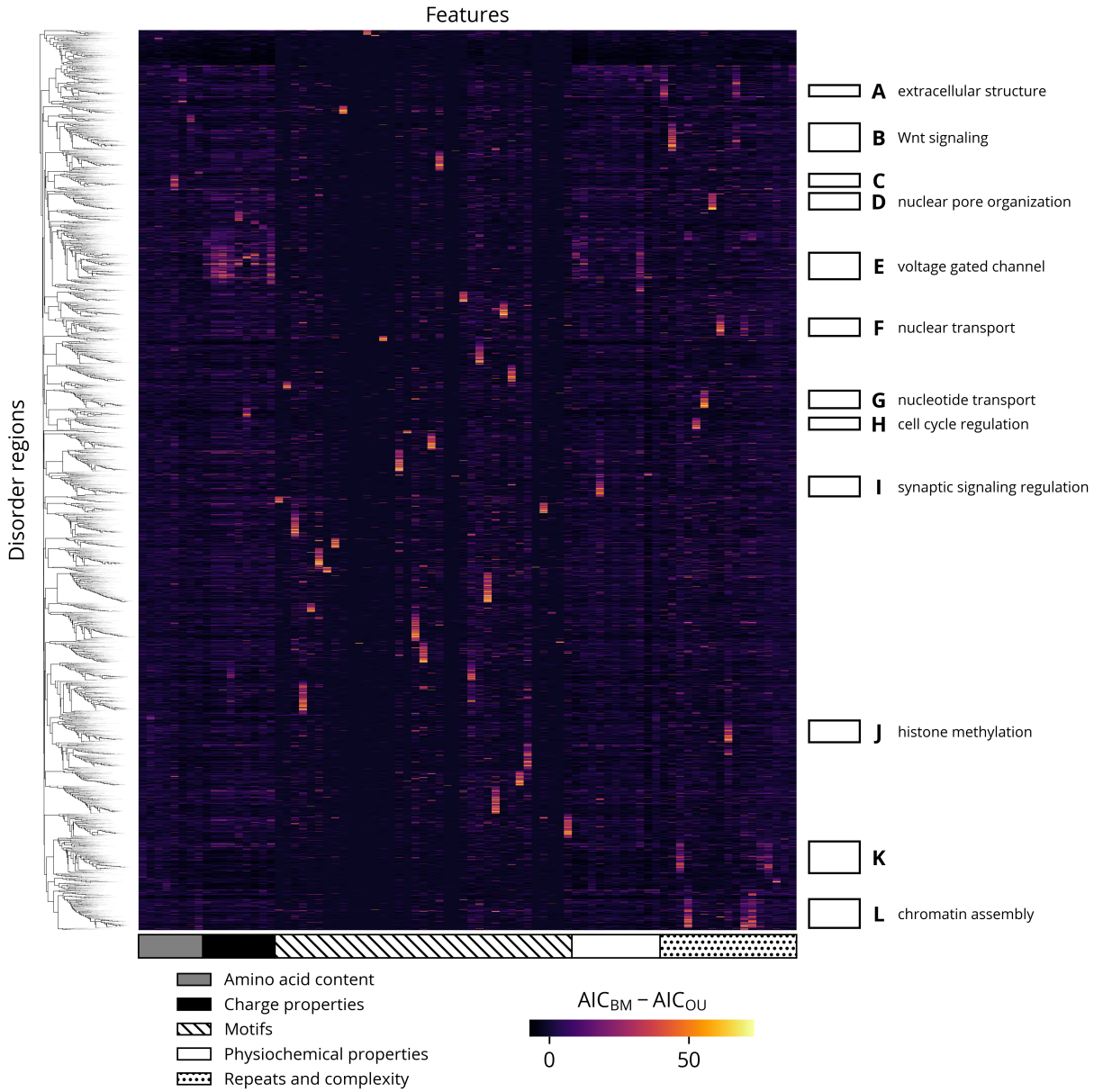

Figure 2.5. Hierarchical clustering of evolutionary signatures. The AIC difference between the BM and OU models is measure of their relative goodness of fit to the data with a penalty for the number of parameters in each. Larger values indicate a better fit by the OU model. Clusters are indicated by rectangles on the right. The cluster descriptions are summaries of selected significantly enriched annotations ($p < 0.01$) and do not necessarily correspond to specific terms.

The resulting heatmap reveals patterns of similar signatures interspersed among a high background of noise (Fig. 2.5). However, we identify at least 12 clusters with a strong and consistent patterns of

constraint, with many having significant associations with certain processes, functions, or compartments. For example, cluster B is strongly enriched in proteins associated with the Wnt signaling pathway, and cluster F contains many proteins involved in nuclear transport. (Selected annotations corresponding to the summaries in Fig. 2.5 are given in Table B1.) Though these preliminary results suggest the existence of a high-level relationship between certain patterns of conserved features and function, further insight into the mechanisms that underpin these associations will rely on more in-depth analyses of specific clusters and the properties of their constituent IDRs.

2.3 Discussion

2.3.1 IDRs have distinct patterns of sequence and feature evolution

In this study, we applied several phylogenetic models to IDRs to interrogate the evolution of their sequences and molecular features. Most significantly, through a comparison of two models of continuous trait evolution we demonstrate evidence of widespread constraint in IDRs within the *Drosophila* proteome. Furthermore, using evolutionary signatures derived from these models, we identify several clusters of IDRs with shared patterns of constraint and associations with specific biological functions. Most immediately, this work generates hypotheses on the importance of various molecular features that will aid in the functional dissection of IDRs in specific proteins. More broadly, though, it suggests that constraint of distributed features is a mechanism of IDR evolution common to multiple biological systems. However, in the absence of more detailed analyses of individual clusters, it remains unclear if any are homologous or analogous to those identified in yeast. Additionally, the clusters' functional associations require careful interpretation. For example, the cluster descriptions summarize a subset of the enriched annotations which were selected for their related functions. Because the significance tests were not corrected for multiple testing or controlled for their false discovery rate, some annotations with significant enrichment, which may include the subset selected for the cluster descriptions, are likely spurious. Thus, while these initial results are promising, further investigation is necessary to corroborate them.

In addition to these global clusters of conserved features, we found IDRs exhibit other distinct patterns of evolution. For example, a comparison of the exchangeability matrices fit to the disorder and order regions shows that, relative to the order regions, the disorder regions have decreased exchangeability coefficients between the disorder-enriched residues. Conversely, the disorder-depleted residues have increased exchangeability coefficients with each other. As a residue's enrichment in IDRs is generally interpreted as a measure of its ability to promote intrinsic disorder, these results indicate that within IDRs and relative to folded domains, disorder-promoting residues are subject to stricter constraints, whereas structure-promoting residues are more biochemically interchangeable. A potential weakness of this analysis is its dependence on sequence alignments which were created using scoring matrices that are in turn derived from other substitution models. Previous studies have attempted to minimize the impact of this circular dependency through an EM-like procedure where substitution models are first fit to alignments, and the sequences in the alignments are then re-aligned with scoring matrices derived from the fit models in alternating rounds until convergence [126, 127]. Because our analyses fit the substitution models directly from alignments, the observed patterns are possibly an artifact of using a scoring matrix derived from folded domains to align IDRs. However, as our matrices reproduce the trends reported in these prior studies, they likely reflect true differences in the patterns of residue substitution within IDRs.

This result is a partial reversal of the typical pattern observed in folded proteins where the gen-

erally larger and more hydrophobic structure-promoting residues are subject to strict geometric constraints imposed by the tightly packed hydrophobic core. In contrast, the smaller and more hydrophilic disorder-promoting residues are more variable, as they often occur in flexible, solvent-exposed regions. It is, however, consistent with other analyses of sequence-function relationships in IDRs. For example, several studies demonstrated that acidic activation domains of transcription factors, which are usually disordered, contain clusters of hydrophobic residues interspersed throughout their largely acidic chains [28–30]. Additionally, these studies showed that many distinct sequences can yield similar levels of transcriptional activity. Together, these findings suggest a model of transcriptional activation where the repulsions between acidic residues maintain the bulky hydrophobic residues in accessible conformations that in turn allow the activation domains to bind their targets through non-specific hydrophobic interactions. As these interactions do not require highly complementary interfaces, the observed increase in exchangeability coefficients between hydrophobic residues is consistent with this model and may reflect the prevalence of such "fuzzy complexes" in IDR interactions. Furthermore, other studies have shown that different disorder-promoting residues have specific effects on the material properties of condensates formed by phase-separating IDRs. For example, in FUS family proteins glycine residues enhance fluidity, whereas glutamine and serine residues promote hardening [128]. Even glutamine and asparagine residues, which differ by a single methylene group, can have disparate effects on the conformational preferences of IDRs. While glutamine-rich sequences are conformationally heterogeneous and form toxic aggregates, asparagine-rich sequences instead assemble into benign amyloids, as asparagine's shorter side chain promotes the formation of turns and β-sheets [129]. Thus, these observations along with the decreased exchangeability coefficients between disorder-promoting residues suggest that subtle differences in their biochemical properties may constrain patterns of residue substitution in IDRs.

2.3.2 Disorder is correlated with many molecular features

Though the mutations generated by evolution are not a random or exhaustive sample of sequence space, they are perturbations of a common ancestor which can reveal the relationship between a region's biophysical properties and its propensity for disorder. Thus, the analysis of feature and score contrasts is effectively a natural "mutational scanning" experiment. We found that disorder scores have the strongest correlations with features that measure a region's overall polarity and hydrophobicity, *e.g.* fraction_disorder and hydropathy. As the formation of a hydrophobic core is a major driving force in protein folding, this relationship is expected. However, the strength of these correlations indicate that a region's relative proportion of hydrophilic and hydrophobic residues is, to a first approximation, the largest determinant of predicted intrinsic disorder.

Excluding these hydrophobicity-related features, the next strongest association is a negative correlation with wf_complexity, demonstrating the predictor strongly associates low complexity with intrinsic disorder. However, sequence complexity is a statistical rather than a biophysical criterion, and while many disordered regions have low levels of complexity, some low-complexity regions, like collagen, are structured. This suggests that while disorder predictors are in general accurate classifiers of a residue's structural state [32], they can conflate the correlates of intrinsic disorder with their causes. Therefore, in some cases their predictions may require careful interpretation.

The remaining significant correlations are generally weak and likely reflect a partial redundancy with the more strongly correlated features discussed previously. Interestingly, though, disorder scores are weakly correlated with many motifs, with the signs largely reflecting their class. For example,

the correlations with docking (DOC) and ligand binding (LIG) sites are largely negative, whereas those with modification (MOD) sites are generally positive. However, this analysis does not indicate whether the predictor responds to these motifs directly or to features that are correlated with them. For example, docking and ligand binding sites are generally mediated by small hydrophobic patches, so the correlations could reflect an increase in hydrophobicity caused by an additional hydrophobic residue "completing" the motif rather than the motif itself. Likewise, IDRs are highly enriched in phosphorylation sites, many of which are targeted to disorder-promoting residues like serine or threonine. As the disorder scores and features are calculated at the level of regions, whose lengths can exceed 1,000 residues, this analysis is limited in its ability to distinguish these possibilities. However, a more targeted *in silico* mutational analysis would yield further insights.

The GO annotation enrichment analysis indicates that proteins involved in DNA repair and extracellular structures contain a disproportionate number of regions whose disorder scores are rapidly evolving. Because the significance tests were not corrected for multiple testing or controlled for their false discovery rate, we caution against over-interpreting this result and instead consider it as a hypothesis for further investigation. In general, however, the regions with rapidly evolving disorder scores may correspond to molecular recognition features (MoRFs), which are modules in IDRs that undergo a disorder-to-order transition on binding their targets [17, 130]. Because MoRFs already exist on the boundary between disorder and structure, small changes in the biophysical properties of these regions may have large effects on their structural ensembles. Thus, the most variable disorder scores may reflect instances where a mutation triggered a "phase transition" between largely structured or disordered native states.

2.3.3 Future evolutionary analyses of IDRs will require a multimodal approach

As discussed by Zarin *et al.*, the interpretation of evolutionary signatures is complicated by several methodological limitations [125]. For example, because IDRs are identified as contiguous segments of high predicted disorder, their boundaries are defined by adjacent structural elements. This approach can therefore split an IDR that is a single evolutionary or functional unit if it contains a semi-disordered module that scores below the threshold. Conversely, it can also merge two distinct IDRs if they are not separated by at least one folded domain. Another challenge is the significant overlap in the definitions of many features induces strong correlations that preclude straightforward quantitative manipulations or interpretations of an IDR's evolutionary signature. The original authors have since addressed this in subsequent studies by applying machine learning methods to perform feature selection or learn features directly from alignments of IDRs [117, 131]. However, integrating these methods into a unified phylogenetic comparative framework will require further effort.

By fitting the BM and OU models to molecular features calculated from alignments of IDRs, we were able to quantify the relative support for constrained and unconstrained models of IDR evolution using a statistical framework. As the BM and OU models describe the evolution of arbitrary continuous traits, a strength of this approach is its independence from assumptions about the underlying process of sequence evolution. In contrast, the previous study used simulations to generate null distributions for a model of no constraint and defined an IDR's evolutionary signature as its deviation from these distributions. However, these comparisons do not directly demonstrate evidence of stabilizing selection but instead test for differences from the null hypothesis. Thus, this approach is highly dependent on the specification and parameterization of these simulated models. Accordingly, an error in either can yield evidence of constraint for an IDR even if none of

its molecular features are under selection.

However, the comparative phylogenetics methodology applied here also has limitations. As many features have strict boundaries or cannot vary continuously, they violate one or more of the underlying assumptions of the BM and OU models. Fortunately, for many features these inconsistencies likely do not seriously compromise the analysis. For example, though compositional features like fraction_S are mathematically restricted to the interval between zero and one, they are likely constrained by much narrower selective regimes, and within these regimes, their behavior is effectively described by an OU model. For other features, however, the deviations are more consequential. For example, net_charge and the motif features can only assume integer and non-negative values, respectively, which imposes significant restrictions on their allowed increments that are not reflected in the BM and OU models. Instead, more appropriate models for count data are birth-death processes, which are Markov chains defined on the natural numbers. However, though linear birth-death processes are well-studied and widely applied in biology [132], to our knowledge there are no simple parameterizations which describe a mean-reverting behavior analogous to the OU model. Thus, further theoretical developments are needed to apply birth-death processes as a model of stabilizing selection in studies of IDR evolution.

While the BM and OU models are powerful tools for studying trait evolution, their generality limits the specificity of the hypotheses they can test. In contrast, because simulation-based approaches can specify arbitrary constraints, they permit investigations of increasingly refined models of IDR evolution. We therefore view the two approaches as complementary and propose the use of hybrid methods where test statistics are derived from phylogenetic comparative methods like the BM model, and simulations generate the null distributions for those test statistics. While simulations can eliminate specific hypotheses, the substantial resources involved both in designing them and generating samples make exhaustively testing mechanisms of feature constraint by simulation impractical. We instead recommend a workflow that begins with an analysis using general models of trait evolution to suggest specific hypotheses of constraint that are then tested with a simulation-based approach. Another hybrid method involves using sequence permutations to test for the conservation of motifs or patterned features like kappa. In this method, a comparative model like BM provides the test statistic as before, and a sample of shuffled sequences approximates the null distribution. Because the background distribution of residues is preserved, this procedure can specifically test for the conservation of motifs or patterned features in an IDR independent of the conservation of its composition.

However, as IDRs are likely subject to multiple selective pressures where the constraints on different compositional, patterned, or motif features are highly specific to each, we anticipate a range of computational and experimental methods will be needed to disentangle the complex forces driving their evolution. Accordingly, while these results represent a significant step forward in relating sequence to function in IDRs, further studies exploring these and other approaches will undoubtedly reveal new insights into these ubiquitous but poorly understood regions of proteins.

2.4 Materials and methods

2.4.1 Alignment and species tree provenance

Alignments of 8,566 single copy orthologs and the corresponding outputs of the missing data phyloHMM were obtained from the analyses conducted in chapter 1. Likewise, the LG consensus tree

generated by the "non-invariant, 100% redundancy" sampling strategy was used as the input or reference where indicated in subsequent phylogenetic analyses.

2.4.2 IDR prediction and filtering

Based on its strong performance in a recent assessment of disorder predictors, AUCPreD was chosen to identify regions with a high probability of intrinsic disorder [32, 122]. After removing the gap symbols from the sequences in the alignments, the disorder scores of each sequence were predicted individually. (Alignments 0204 and 35C2 contained sequences which exceeded the 10,000-character limit and were excluded from subsequent analyses.) The resulting scores were then aligned using the original alignment. The average score for each position was calculated using Gaussian process sequencing weighting over the LG consensus tree [99]. Any positions inferred as "missing" by the missing data phylo-HMM or to the left or right of the first or last non-gap symbol, respectively, were excluded. For simplicity, the Gaussian process weights were not re-calculated from a tree pruned of the corresponding tips, and instead the weights corresponding to the remaining sequences were re-normalized. The scores at any remaining positions with gap symbols were inferred by linear interpolation from the nearest scored position.

The average disorder scores were converted into contiguous regions with the following method. Two binary masks were defined as positions where the average score exceeded high and low cutoffs of 0.6 and 0.4, respectively. The low-cutoff mask was subjected to an additional binary dilation with a structuring element of size three to merge any contiguous regions separated by a small number of positions with scores below the cutoff. "Seed" regions were then defined as 10 or more contiguous "true" positions in the high-cutoff mask, and "disorder" regions were obtained by expanding the seeds to the left and right until the first "false" position in the low-cutoff mask or the end of the alignment. "Order" regions were taken as the complement of the disorder regions in each alignment.

The regions were filtered with the following criteria. First, segments with non-standard amino acid symbols, which overlapped with any position labeled as "missing" by the missing data phylo-HMM, or whose number of non-gap symbols was below a length cutoff of 30 residues were removed. Regions whose remaining segments failed the set of phylogenetic diversity criteria detailed in Table A2 were excluded. The final set contained 11,445 and 14,927 disorder and order regions, respectively, from 8,466 distinct alignments.

2.4.3 Fitting substitution models and trees

To fit amino acid substitution matrices to disorder and order regions, 25 meta-alignments for each were constructed by randomly sampling 100,000 columns from the respective regions. To determine the effect of gaps, the maximum fraction of gaps was set at 0, 50, 100%. The combination of the region types and sampling strategy yielded six different sets of meta-alignments. A GTR20 substitution model with four FreeRate categories and optimized state frequencies was fit to each meta-alignment using IQ-TREE 1.6.12 [103]. Exchangeability and rate coefficients were normalized, so the average rate of each model was equal to 1. Because exchangeability and rate coefficients are highly correlated across meta-alignments of the same region type, all figures are derived from the maximum 50% gap fraction meta-alignment sets unless otherwise noted (Fig. B2-B4).

To obtain estimates of the average substitution rates in each region, separate amino acid and indel models were fit to each alignment. For the amino acid substitution models, the columns in the alignments were manually segregated into disorder and order partitions using the regions derived

from the AUCPreD scores. However, to prevent poor fits from a lack of data, a partition was created only if it contained a minimum of 20 sequences with at least 30 non-gap symbols. If one partition met these conditions but the other did not, the disallowed partition was consolidated into the allowed one. If neither partition passed, the alignment was skipped. These rules ensured that the regions represented in the final set were fit with substitution models which were concordant with their predicted disorder states. Trees were fit to each partition with an invariant and four discrete gamma rate categories using IQ-TREE 1.6.12 [102]. The disorder partition used a substitution model derived from the average of the state frequencies and exchangeability coefficients fit to the 50% gap fraction meta-alignment sets sampled from the disorder regions. The order partition used the LG substitution model [86]. To prevent overfitting of branch lengths, the trees were restricted to scaled versions of the reference species tree using the --blscale option.

As inference with models that allow insertions and deletions of arbitrary lengths is computationally intractable, a more heuristic approach was taken to quantify the amount of evolutionary divergence resulting from indels in the alignments. For a given alignment, all contiguous subsequences of gap symbols with unique start or stop positions in any sequence were defined as binary characters. Then for each character a sequence was coded with the symbol 1 if the character was contained in that sequence, or it was nested in another contiguous subsequence of gap symbols in that sequence. Otherwise the sequence was coded with the symbol 0. GTR2 models with optimized state frequencies and ascertainment bias corrections were fit to the resulting character alignments. A discrete gamma rate category was added for every five character columns, up to a maximum of four. To prevent overfitting of branch lengths, the trees were restricted to scaled versions of the reference species tree using the --blscale option.

Because the rate and branch lengths of a phylogenetic substitution model always appear as products in the likelihood expression, they are not jointly identifiable parameters. Instead, the rate is conventionally taken as equal to one (with inverse count units), and the branch lengths are expressed in terms of the expected number of substitution events per column. For models with multiple rate categories, the equivalent condition is that the mean of the prior distribution over the rate categories is equal to one. This effectively makes each rate category a scaling factor of the branch lengths. The inferred rate of a column, calculated as the mean of the posterior distribution over the rate categories, is therefore relative to the average across all columns in the alignment. Thus, an absolute measure of the evolutionary divergence of a column can be obtained by multiplying the inferred rate by the total branch length of the tree. However, as the alignments contain variable numbers of species, this total branch length represents the contribution of both the rate and the tree topology. To normalize for this effect, the total branch length for each tree fit to an alignment was divided by the total branch length of the reference species tree including only the species in that alignment. The reported substitution rate is therefore the product of this scaling factor and the inferred column rate. The average amino acid or indel substitution rate for a region was calculated as the mean of the respective rates across all columns. Because the indel rates were associated with columns in character alignments, they were mapped back to the original sequence alignment by assigning half of a character's rate to its start and stop positions. Since indel models with limited data were prone to overfitting, rates obtained from character alignments with fewer than five columns were set to zero.

2.4.4 Definition and calculation of features

Features were calculated as in Zarin *et al.* with the following modifications [125]. The regular expression for polar residue fraction was [QNSTCH], which, in contrast to the original study, excludes glycine residues. Additionally, length, expressed in log scale, was replaced with a feature proportional to the radius of gyration for an excluded-volume polymer [133]. Because the radii of gyration of chemically denatured proteins closely match the values expected for equivalent random coils [134], we felt this feature would better capture the relationship between an IDR's length and its biophysical properties. Finally, several motifs from ELM were replaced with their metazoan counterparts or updated versions of the same entries [135]. These differences are noted in the supplementary data. Furthermore, unlike the previous work, motifs were left as counts and not normalized to the proteome-wide average. Kappa, omega, SCD, hydropathy, PPII propensity, and Wootton-Federhen sequence complexity were calculated with localCIDER 0.1.19 [136]. Isoelectric point was calculated with the Python package isoelectric, which is available on PyPI or at `https://isoelectric.org/` [137]. Otherwise, features were implemented with custom code. A full list of features and their definitions is given in Table B2 and Table B3.

2.4.5 Brownian motion and Ornstein-Uhlenbeck analyses

Brownian motion (BM) model parameters were calculated with two methods. The first used Felsenstein's contrasts algorithm to efficiently calculate roots and contrasts for the disorder scores and features of each region [138, 139]. Rates were calculated as the mean of the squares of the contrasts. Though these values are unbiased, they are not maximum likelihood estimates and are inappropriate for use with the Akaike information criterion (AIC) [140]. Thus, they were used for analyses involving only the BM model. For comparison with the Ornstein-Uhlenbeck (OU) model, the BM parameters were calculated by maximizing the likelihood. The OU model parameters were also calculated via maximum likelihood estimation as described in Butler *et al.* [141]. To ensure parameter identifiability and estimate consistency, the root was treated as a random variable [123, 124]. Thus, the covariance matrix, V, was parameterized as $V_{ij} = e^{\alpha d_{ij}}$ where d_{ij} is the tree distance between tips i and j, and α is the selection strength [123].

The AICs were calculated for the models of each feature using their maximized likelihoods and two and three parameters for the BM and OU models, respectively. The pairwise differences in the AICs yielded a vector with 82 components, each representing the relative goodness of fit of the OU model over the BM model after accounting for their difference in complexity. The vectors were clustered using the correlation distance metric and the UPGMA algorithm. Clusters were manually chosen for subsequent GO analyses. To enrich these clusters for regions with a high likelihood of feature conservation despite low levels of sequence identity, this analysis was restricted to the 7,645 regions whose amino acid and indel substitution rates exceeded 1 and 0.1, respectively (Fig. B11).

2.4.6 GO term analyses

The 2022-03-22 go-basic release of the Gene Ontology was obtained from the GO Consortium website [142, 143]. The gene association file for the 2022_02 release of the *D. melanogaster* genome annotation was obtained from FlyBase [44]. Obsolete annotations were dropped, and the remaining annotations were filtered by qualifiers and evidence code. The allowed qualifiers were "enables," "contributes_to," "involved_in," "located_in," "part_of," and "is_active_in." The allowed evidence codes were all experimental sources, traceable author statement (TAS), and inferred by curator (IC). The annotations were propagated up the ontology graph and joined with the region sets, so

every annotation associated with a gene was associated with the regions derived from that gene. *P*-values were calculated with exact hypergeometric probabilities with regions considered as the sampling unit. For the disorder score analysis, the reference set was the filtered regions, and the enrichment set was the regions in the upper decile of the score rate distribution (Fig. B7). For the cluster analysis, the reference set was the regions after the additional filtering by substitution rates, and the enrichment sets were the regions in each cluster.

2.4.7 Code and data availability

The code used to produce the results and analyses is available at `https://github.com/marcsingleton/IDR_evolution2023`. The following Python libraries were used: matplotlib [104], NumPy [105], pandas [106], SciPy [107], and scikit-learn [144]. Relevant output files are available in the supporting information. There are no primary data associated with this manuscript. All primary data are available from publicly accessible sources described in their corresponding sections.

CHAPTER 3

Tools and tutorials for fitting mixture models and HMMs

Abstract

Fitting statistical models to data is often a key step in the scientific method because it can formalize hypotheses and conclusions as unambiguous and testable statements. The major scientific computing library for the programming language Python, SciPy, provides ready-to-use implementations of core statistical functions, which allows users with varying levels of expertise to easily apply them to their data. However, SciPy does not support two common and powerful types of models called mixture models and hidden Markov models (HMMs). Other more specialized packages such as hmm-learn and pomegranate provide implementations for a restricted subset of these models, but they use APIs which are not compatible with SciPy. This can pose a barrier to entry for beginners and prevent more advanced users from easily extending these packages' capabilities. We therefore created two packages, MixMod and Homomorph, that implement mixture models and HMMs, respectively, and conform to the SciPy API for specifying distributions. Each package is fully documented, and we wrote a set of tutorials which both introduce their APIs and illustrate various training techniques through a series of examples. These packages are available on the Python Package Index (PyPI) under the names mixmod and homomorph, and the source code is hosted alongside the tutorials on GitHub at `https://github.com/marcsingleton/mixmod` and `https://github.com/marcsingleton/homomorph`, respectively.

3.1 Overview of tools and tutorials

Most code written for data analysis is *ad hoc*, that is, it is intended to accomplish a single task and cannot be used for any other purpose. However, often solving one problem entails solving several other problems along the way, and sometimes those intermediate solutions are general enough to be widely useful. This happened twice over the course of this work, both times involving fitting probabilistic models to data. The first was mixture models, which describe data that contain several subpopulations, each with its own statistical properties, mixed together. For example, in exam scores there are often two clusters: the high-scoring group of students who understood the material and the low-scoring group who did not. The second was hidden Markov models (HMMs), which like mixture models, describe data with several subpopulations. However, in HMMs the data are ordered in a time series and observations from a given subpopulation tend to occur consecutively. These models are frequently used to analyze systems which toggle between different states over time, for example periods of growth and recession in the economy.

Both types of models are well-known and frequently used. Despite this, none of the major scientific computing libraries for Python such as SciPy or statistical modules like scikit-learn or statsmodels

contained generic implementations of either. A major factor in this exclusion is likely the high level of stability and consistency these packages guarantee. Mixture models and HMMs are not so much single models but rather recipes for creating models. As a result, implementing these models for arbitrary distributions is not trivial, so these packages often sacrifice generality to support training methods for common use cases. For example, scikit-learn implements mixture models where all subpopulations are restricted to normal distributions. Other more specialized packages like hmm-learn and pomegranate are more flexible, but they still limit their built-in support to a relatively small number of common distributions, including normal, exponential, categorical, and Poisson, among others. Furthermore, to support these additional features these packages implement custom APIs which may pose a barrier to users who are already comfortable with the interface of SciPy's statistical module.

We therefore sought to create lightweight implementations of mixture models and HMMs which are available in the packages MixMod and Homomorph, respectively. A key design goal was to ensure these packages were both immediately accessible but also easily extensible. Thus, both packages conform to the SciPy API for specifying distributions, which allows use of its large number of distributions but also permits advanced users to easily implement custom distributions as needed. Fitting models parameterized by arbitrary distributions to data remains a significant challenge, however. MixMod supports fitting models whose subpopulations are parameterized by roughly a dozen distinct distributions, including several common continuous and discrete distributions. Homomorph has no built-in methods for fitting models. We instead wrote an extensive tutorial that covers the theory and implementation of several model fitting approaches for specific distributions. This tutorial is the centerpiece of a series of tutorials for both MixMod which demonstrate their APIs and common applications through a series of examples. Our hope is together these packages and tutorials will bridge the gap between beginner and advanced users by illustrating how complex probabilistic models are constructed from simple pieces.

The tutorials are available alongside the source code for these packages on GitHub. Though each is largely independent of the others, they follow a logical progression. For example, both Mixmod and Homomorph have tutorials which serve as brief introductions to the theory, applications, and APIs for their respective models. Homomorph then has two additional tutorials. The first discusses a generalization of HMMs called autoregressive HMMs (ARHMMs), and the second covers methods for training HMMs. For brevity, only the training tutorial is adapted from its current form in the following section. As the tutorial is a self-contained document with an introduction and conclusion, it is presented without further commentary.

3.2 HMM training tutorial introduction

Welcome to the training tutorial! Since Homomorph doesn't have built-in methods for fitting HMMs to data, in this tutorial we'll cover examples of training HMMs where the hidden states are both known and unknown using maximum likelihood estimation and the estimation-maximization algorithm, respectively. We'll then discuss an advanced approach called discriminative training.

The material in sections four through six owes a heavy debt to two sources, respectively. The first is the book *Biological Sequence Analysis*, which is an excellent resource on HMMs and other probabilistic models and their applications [145]. The second is the paper Hidden Neural Networks by Anders Krogh and Søren Riism [101]. Many of the theoretical results for HMMs shown here are adapted or expanded from the derivations outlined in those references, so this tutorial wouldn't

have been possible without them.

Clearly we have a lot of ground to cover, so let's get started!

3.3 What is training?

3.3.1 Training, informally

Training and learning are jargon commonly used in machine learning. While convenient as shorthand, they obscure what's actually happening: parameter estimation or, more generally, optimization. Statistical models are specified by some number of parameters, so the name of the game is choosing parameters that fit the data the best. Depending on the model, this can be as simple as taking an average or as complex as needing specialized algorithms and thousands of computing hours. Note that the notion of a "best" fit to the data isn't always immediately obvious, and some applications will define it differently. (We'll see at least two distinct definitions in the following sections.) In every case, however, some quantity of interest is defined that is hopefully correlated with the ability to predict real-world outcomes, and then some computational method is used to find parameters that maximize or minimize that quantity.

3.3.2 Training, formally

Now that we understand what training is intuitively, let's briefly discuss how it's defined mathematically. This section will mainly serve to introduce some terminology used throughout this tutorial, but it will also highlight the features that are common to all optimization problems regardless of application or mathematical form.

At the core of every optimization problem is a function whose output is optimized with respect to one or more inputs. This is called the *objective function* or simply the *objective*. This terminology is common when discussing optimization generically, and the kind of extremum (minimum or maximum) is unstated. In machine learning and statistics, however, the objective is often framed as a kind of distance between the model's output and the actual data. Distance has a very specific meaning in mathematics, so instead this quantity is called *loss*. Naturally, then, the goal is to minimize loss. Unlike in many optimization problems where the optimal value of the objective is as important as the inputs that achieve that optimum, when fitting models the loss is often only a means to an end. Though the loss has applications when comparing the fits of different models, the optimized parameters are typically the ultimate goal.

The form of the loss function depends on the exact nature of the problem, so it's difficult to go any further without speaking in overly general terms. Thus, to illustrate these concepts mathematically, we'll use an extremely common loss function, the mean squared error. Let's now define the data, model, and loss precisely. The data, D, are composed of N examples which are the indexed ordered pairs $\{(x_i, y_i) : 1 \leq i \leq N\}$. Each x_i and y_i is an input and output, respectively. Though these quantities can be vector-valued, we'll keep our discussion general enough to not have to worry about these details. The model is a function, f, which accepts an input, x, and returns an output, $\hat{y}$. The output is designated with a hat to indicate it was calculated from the model rather than observed. This function also accepts a set of parameters, Θ, which can be tuned to better fit the data. Thus, we write $\hat{y} = f(x, \Theta)$. Finally the loss function, L, accepts the data, model, and parameters and returns a measure of the deviation from the data, $L(D, f, \Theta)$. For the mean squared error, this is written as

$$L(D, f, \Theta) = \frac{1}{N} \sum_{i=1}^{N} (\hat{y}_i - y_i)^2$$
$$= \frac{1}{N} \sum_{i=1}^{N} (f(x_i, \Theta) - y_i)^2 .$$

In this case, the loss is expressed as a sum over individual examples. This is extremely common, so losses are frequently written in terms of an individual input and output pair rather than the data as a whole. Furthermore, since the data and model are usually fixed, they are often dropped as arguments, making the loss a function of the parameters alone:

$$L(D, f, \Theta) = L(\Theta).$$

The optimized or learned parameters are then written as

$$\hat{\Theta} = \underset{\Theta}{\operatorname{argmin}}\, L(\Theta).$$

Finding these optimal parameters is not always straightforward. For simple models, such as one-dimensional linear regression where $f(x, \Theta) = \theta_1 x + \theta_0$, there are closed-form solutions. However, many modern machine learning models offer no such luxury, so other approaches are needed. There are various techniques for such cases depending on the structure of the model. However, all are usually iterative in nature, meaning they gradually decrease the loss in a series of steps. For complex models and large data sets, each step can involve significant computation, which is why these models are often trained on computational clusters with specialized hardware.

3.4 Training with known states

Sometimes the universe is kind and gives us data where the underlying states are known. This is by far the easiest case since all the information is available to us, and as HMMs are probabilistic models, we can rely on the rich theory of mathematical statistics to define optimality and identify the corresponding parameters. Depending on the emission distributions, there are even closed-form solutions for these optimal parameters!

3.4.1 Maximum likelihood estimation

The strength of probabilistic models is that for a given set of parameters, every possible input is associated with a probability or probability density, so objective functions are naturally defined in terms of these quantities. This doesn't answer the question of what probability we should try to optimize, however. There are several common approaches, but one of the most natural is to maximize the probability of the data with respect to the parameters. Let's clarify what this means by writing it mathematically. We call our data, which is a set of indexed observations $\{x_i : 1 \leq i \leq N\}$, D and the probability mass function $f(x, \Theta) = P(X = x|\Theta)$. (The right-hand

side translates to "the probability that the random variable called X assumes the value x given the set of parameters Θ." In probability, the random processes that generate observations are distinguished from the observations themselves.) The probability of the data is then written as

$$\begin{aligned} P(D|\Theta) &= \prod_{i=1}^{N} P(X = x_i|\Theta) \\ &= \prod_{i=1}^{N} f(x_i, \Theta) \end{aligned}$$

since each observation is independent and identically distributed. Sums are easier to work with, so it's common to take the logarithm of both sides and call the result

$$L(\Theta) = \log P(D|\Theta) = \sum_{i=1}^{N} \log f(x_i, \Theta)$$

the *log-likelihood function*. The original product then is the *likelihood function*; however, the logarithm doesn't change the position of the extrema, so this distinction is not very important for our purposes.

Before moving forward, let's discuss some nuances of the likelihood function. First, even though it's defined in terms of observations that assume discrete values (notice that f is probability rather than a probability density), the definition is the same for continuous observations. The only difference is the likelihood is no longer considered a probability since it's technically a probability density. However, this not a common interpretation anyway since even for discrete data the probability of any set of observations approaches zero as the number of observations increases. It's instead more useful to compare ratios of likelihoods under different models. That, however, is a topic for another time. Another subtle point is the likelihood function is not the probability that the parameters are correct. Instead a particular choice of parameters is viewed as certain, and then the probability of the data is calculated given that choice. Finally, as with the mean squared loss defined earlier, though the likelihood is technically a function of both the parameters and the data, the data are often dropped as an argument to emphasize that they are typically fixed.

Unlike for a loss function, we want to maximize the log-likelihood since this maximizes the probability of the data under the model. This defines the following set of parameters

$$\hat{\Theta} = \underset{\Theta}{\operatorname{argmax}}\, L(\Theta)$$

which are known as *maximum likelihood estimates* (MLEs). Though this objective isn't quite a loss in the sense of a distance from some desired outputs, it's similar in spirit. Since the model should assign common events high probabilities (and accordingly rare events low probabilities since the total probability is constrained to sum to one), the log-likelihood in effect penalizes deviations from the empirical distribution. In fact, simply negating the log-likelihood function converts the

maximization into a minimization, making it a kind of loss. Furthermore, for some models algebraic manipulations can reveal an expression which is more readily interpreted as a distance.

Calculus tells us that for differentiable functions local extrema are necessarily where the derivative relative to the input is zero. If Θ is a set of N parameters, this condition must occur simultaneously for the derivative relative to each. In other words,

$$\frac{\partial L}{\partial \theta_1} = 0, \quad \ldots, \quad \frac{\partial L}{\partial \theta_N} = 0$$

for each $\theta_i \in \Theta$. In some cases these equations can be solved explicitly, but often numerical techniques are needed. We'll see two examples of such approaches in later sections.

3.4.2 Maximum likelihood estimates for HMMs

Decomposition into independent products

Now we'll turn to HMMs and derive the MLEs for labeled data. Here the data, D, are again composed of N examples of ordered pairs $\{(x_i, y_i) : 1 \leq i \leq N\}$ where x_i is a sequence of states and y_i is a sequence of emissions, each with length T_i. The probability of the data given the parameters is then

$$\begin{aligned} P(D|\Theta) &= P(X_1 = x_1, Y_1 = y_1, \ldots, X_N = x_N, Y_N = y_N|\Theta) \\ &= \prod_{i=1}^{N} P(X_i = x_i, Y_i = y_i|\Theta). \end{aligned}$$

The joint probability expands into a product of the probabilities of individual examples since each is independent and identically distributed. Let's focus on one pair of state and emission sequences denoted x and y, each with length T. Using the Markov property of HMMs, we can derive an expression for their joint probability:

$$\begin{aligned} P(D|\Theta) &= P(X = x, Y = y|\Theta) \\ &= P(Y_1 = y_1|X_1 = x_1, \Theta)P(X_1 = x_1|\Theta) \\ &\quad \times \prod_{t=1}^{T-1} P(Y_{t+1} = y_{t+1}|X_{t+1} = x_{t+1}, \Theta)P(X_{t+1} = x_{t+1}|X_t = x_t, \Theta). \end{aligned}$$

(Note that here the subscripts refer to the index within a sequence rather than the index of the example.)

All these capital letters are cluttering this expression, so we'll make a few common substitutions to simplify it. First, we assume there are S states numbered from 1 to S and write the transition and

start probabilities as $P(X_{t+1} = j|X_t = i, \Theta) = a_{ij}$ and $P(X_1 = i|\Theta) = a_{0i}$, respectively. Second, we define $e_i(y_t) = P(Y_t = y_t|X_t = i, \Theta)$. We can think of each e_i as a function that accepts an emission y_t and outputs a probability or probability density. Putting all this together, we have

$$P(X = x, Y = y|\Theta) = e_{x_1}(y_1)a_{0x_1} \prod_{t=1}^{T-1} e_{x_{t+1}}(y_{t+1})a_{x_t x_{t+1}}.$$

Since log-likelihoods are easier to work with, we take the logarithm of both sides and write the product as a sum of log terms:

$$\begin{aligned}\log P(X = x, Y = y|\Theta) &= \log \left(e_{x_1}(y_1)a_{0x_1} \prod_{t=1}^{T-1} e_{x_{t+1}}(y_{t+1})a_{x_t x_{t+1}} \right) \\ &= \log a_{0x_1} + \sum_{t=1}^{T-1} \log a_{x_t x_{t+1}} + \sum_{t=1}^{T} \log e_{x_t}(y_t).\end{aligned}$$

This is now a fairly clean expression since at each step we pick the right transition probability and emission distribution using the state sequence. However, it will be useful both theoretically and computationally to write this expression in terms of the number of times each transition appears in the sequence. To do this, we first need the Kronecker delta function, which is defined as

$$\delta_{ij} = \begin{cases} 0 & \text{if } i \neq j \\ 1 & \text{if } i = j. \end{cases}$$

Then we can write the number of transitions between states i and j as

$$n_{ij} = \sum_{t=1}^{T-1} \delta_{ix_t}\delta_{jx_{t+1}}.$$

We can define a similar variable that counts the number of times each state starts the state sequence:

$$n_{0i} = \delta_{ix_1}.$$

For a single example, this might seem unnecessarily complex since one n_{0i} is equal to one and all others are zero. However, this form will be convenient for generalizing to data that contain multiple examples.

Inspection of the previous equation shows we can write it using the quantities we've defined and a similar trick with the Kronecker delta function for the emissions:

$$\log P(X = x, Y = y|\Theta) = \log a_{0x_1} + \sum_{t=1}^{T-1} \log a_{x_t x_{t+1}} + \sum_{t=1}^{T} \log e_{x_t}(y_t)$$
$$= \sum_{i=1}^{S} n_{0i} \log a_{0i} + \sum_{i=1}^{S} \sum_{j=1}^{S} n_{ij} \log a_{ij} + \sum_{i=1}^{S} \sum_{t=1}^{T} \delta_{ix_t} \log e_{x_t}(y_t).$$

(To ensure this expression is valid for forbidden start states or transitions, we define $0 \log 0 = 0$.)

While this may look complicated, it's the same sum of the log probabilities of each start state, transition, and emission. However, when it's written in this form, two things are clear. First, many calculations are expressed as the logarithm of a parameter multiplied by the number of times it appears in the training data. Second, each of these sums is independent of the others, meaning they have no parameters in common. In fact, the transition sum can be broken into independent sums for each initial state. The same is true for the emission sum if none of the emission distributions share parameters. This dramatically simplifies the optimization since we can maximize the probability of the entire expression by maximizing each sum separately. Finally, although we've derived this expression for a single pair of state and emission sequences, the form is identical for the data as a whole. The only differences are the counts are taken over all state sequences and the emission sum is taken over all emission sequences.

MLEs for categorical distributions

Now that we've broken the maximization problem into a set of simpler problems, let's review the solutions for each. The optimal parameters for the emissions will depend on their distributions, but the start and transition distributions will always take the form of a single choice from a set of options. This is formally called a *categorical distribution* which itself is a special case of the *multinomial distribution*. Fortunately, the MLEs for categorical distributions have a simple form when they are parameterized directly in terms of the probability of selecting each outcome. The derivation is somewhat involved, so we'll skip to the final result. Using the count variables defined earlier, the MLE for each a_{ij} is given as

$$\hat{a}_{ij} = \frac{n_{ij}}{\sum_{j=1}^{S} n_{ij}}.$$

The interpretation is intuitive. Our estimate of the probability of state i transitioning to state j is simply the fraction of times we observe this in the data! One problem with this equation, however, is if we're working with a relatively small amount of data, we may never observe a certain transition and estimate its probability as zero. This means according to the model the transition is impossible, which may be contrary to our hypothesis of the underlying process. In these cases, it's customary to add a small non-negative correction factor, r_{ij}, for each pair of states:

$$\hat{a}_{ij} = \frac{n_{ij} + r_{ij}}{\sum_{j=1}^{S} n_{ij} + r_{ij}}.$$

These corrections may look like a sloppy fix, but they have a natural Bayesian interpretation as the parameters of a Dirichlet prior on the transition probabilities. What this means in practice is the size of each r_{ij} reflects the prior expectation for the probability of that transition, with larger values indicating more certainty.

3.4.3 Examples

Let's now take what we've learned and apply it to some examples. We'll first write code to estimate the parameters for an HMM with categorical emission distributions since we've already reviewed the MLEs in the previous section. We'll then use the principle of maximum likelihood to derive the estimators for other common emission distributions and write implementations from scratch.

Categorical emission distribution

To get started, we'll first import the packages and some plotting settings used throughout this tutorial.

```
In: import pprint
    import random
    from functools import reduce
    from itertools import accumulate

    import homomorph
    import matplotlib.pyplot as plt
    import numpy as np
    import scipy.stats as stats
    from numpy import exp, log
    from sklearn.metrics import roc_curve
    from utils import fit_CML

    legend_kwargs = {'frameon': False,
                     'loc': 'center left',
                     'bbox_to_anchor': (1, 0.5)}
```

Let's create our HMM. Since the purpose of this tutorial is to illustrate training techniques rather than to motivate the applications of HMMs with relevant examples, we'll arbitrarily label the states with numbers and the emissions with letters.

```
In: t_dists = {1: {1: 0.95, 2: 0.05},
               2: {1: 0.05, 2: 0.9, 3: 0.05},
               3: {2: 0.35, 3: 0.65}}
    e_dists = {1: {'A': 1},
               2: {'A': 0.5, 'B': 0.5},
               3: {'B': 1}}
    start_dist = {1: 0.2, 2: 0.5, 3: 0.3}

    model = HMM(t_dists=t_dists, e_dists=e_dists, start_dist=start_dist)
    model
```

```
Out: HMM(states={1, 2, 3},
         stop_states=[],
         name='hmm')
```

We'll now generate 10 examples, each with length 200. The simulations are returned as a single sequence of (state, emission) tuples. However, since in the theory section we defined the states and emissions as separate sequences, we'll do a bit of Python magic to put the data in this form.

```
In: data = [model.simulate(200, random_state=i) for i in range(10)]
    print('Original form:', data[0][:5])
    data = [list(zip(*example)) for example in data]
    print('New form:', [seq[:5] for seq in data[0]])
```

```
Out: Original form: [(2, 'A'), (1, 'A'), (1, 'A'), (1, 'A'), (1, 'A')]
     New form: [(2, 1, 1, 1, 1), ('A', 'A', 'A', 'A', 'A')]
```

We're now ready to implement the MLEs for the transition probabilities. Before, though, we should discuss selection of the model structure, that is, the number of states and the allowed transitions between those states. Since in this case the data are simulated, we know the structure exactly. However, modeling real-world data is often far more complicated since it's rare to have perfect knowledge of the data generating process even if the states are labeled. Thus, it's tempting to use a fully connected model that allows transitions between each pair of states and let the model learn what transitions are actually used from the data. That said, constraining the allowed transitions can lead to better models, particularly if the constraints reflect a feature of the underlying process.

For this example, we'll assume that we have some domain knowledge that permits us to know the states and their allowed transitions. For example, state 2 can transition to every state, but states 1 and 3 can only transition to themselves and state 2. It's also customary to add a small pseudocount to the allowed transitions to ensure they're permitted by our model in the rare chance that we don't observe them in the data. There are a variety of ways to implement this, but in the approach shown below we first instantiate a transition count dictionary with the pseudocounts. We then iterate over the data to add the observed transitions and afterwards normalize the counts by the total number for each initial state to obtain the estimated transition probabilities.

The strength of this approach is it yields a nested dictionary which we can use as an input to the `HMM` class. We'll actually use the original `t_dists` to establish the model structure, but if it weren't available, we could create a similar nested object which encodes the same information. (Unfortunately, it's hard to avoid specifying at least some portions of the model manually unless it's fully-connected or its structure is highly modular.)

```
In: # Make transition count dicts and add pseudocounts
    t_pseudo = 0.1
    t_counts = {}
    for state1, t_dist in t_dists.items():
        t_count = {}
        for state2 in t_dist:
            t_count[state2] = t_pseudo
        t_counts[state1] = t_count

    # Add observed counts
```

```
for example in data:
    xs, ys = example
    state0 = xs[0]
    for state1 in xs[1:]:
        t_counts[state0][state1] += 1
        state0 = state1

# Normalize counts
t_dists_hat = {}
for state1, t_count in t_counts.items():
    t_sum = sum(t_count.values())
    t_dist_hat = {}
    for state2, count in t_count.items():
        t_dist_hat[state2] = count / t_sum
    t_dists_hat[state1] = t_dist_hat
t_dists_hat
```

```
Out: {1: {1: 0.9548785594639866,
          2: 0.0451214405360134},
      2: {1: 0.05571315102689209,
          2: 0.8965165097015771,
          3: 0.04777033927153069},
      3: {2: 0.2924773022049287,
          3: 0.7075226977950714}}
```

So far so good! The estimated transition probabilities are extremely close to their actual values.

We'll now estimate the emission probabilities. Since the emission distributions are also categorical, the code has nearly the same structure. However, we'll make a small change to illustrate some choices inherent in model selection. Although we assumed we knew the states and allowed transitions perfectly, let's say this isn't true for the emissions. For example, even though we never observe states 1 and 3 emitting an A and B, respectively, we still aren't 100% convinced that it's impossible. Thus, we'll first gather all the possible emission types from the data and instantiate the emission distributions with a small pseudocount for each type. From there the code is largely the same.

```
In: # Collect all possible emissions
    e_set = set()
    for example in data:
        xs, ys = example
        e_set.update(ys)

    # Make emission count dicts and add pseudocounts
    e_pseudo = 0.1
    e_counts = {}
    for state in t_dists:
        e_counts[state] = {emit: e_pseudo for emit in e_set}

    # Add observed counts
```

```
for example in data:
    xs, ys = example
    for state, emit in zip(xs, ys):
        e_counts[state][emit] += 1

# Normalize counts
e_dists_hat = {}
for state, e_count in e_counts.items():
    e_sum = sum(e_count.values())
    e_dist_hat = {}
    for emit, count in e_count.items():
        e_dist_hat[emit] = count / e_sum
    e_dists_hat[state] = e_dist_hat
e_dists_hat
```

```
Out: {1: {'A': 0.999896071502806, 'B': 0.00010392849719393058},
      2: {'A': 0.48755937570685365, 'B': 0.5124406242931463},
      3: {'A': 0.000648508430609598, 'B': 0.9993514915693904}}
```

Again the estimates are very close!

Let's finish this out with the start distribution. The overall idea is exactly the same, except now we're working with a single distribution rather than a dictionary of distributions. Technically, we can only estimate the start distribution from the initial state of each example. Since this severely limits the amount of data relative to the transitions, it may be tempting to use the state counts over all time steps instead. However, this quantity will estimate the equilibrium distribution of the underlying Markov process, which is a function of the transition probabilities and independent of the start distribution. However, there may be data-specific reasons to think these quantities are equal, so this is again an example of a model selection decision.

```
In: # Make start count dicts and add pseudocounts
    start_pseudo = 0.1
    start_count = {}
    for state in start_dist:
        start_count[state] = start_pseudo

    # Add observed counts
    for example in data:
        xs, ys = example
        start_count[xs[0]] += 1

    # Normalize counts
    start_sum = sum(start_count.values())
    start_dist_hat = {}
    for state, count in start_count.items():
        start_dist_hat[state] = count / start_sum
    start_dist_hat
```

```
Out: {1: 0.10679611650485439, 2: 0.5922330097087379, 3: 0.3009708737864078}
```

We're now ready to combine all these individual parameter estimates to create an estimated model.

```
In: model_hat = HMM(t_dists=t_dists_hat,
                    e_dists=e_dists_hat,
                    start_dist=start_dist_hat)
    model_hat
```

```
Out: HMM(states={1, 2, 3},
         stop_states=[],
         name='hmm')
```

Though the estimates match the parameters closely, to really see how well they compare, let's make some predictions using both. We'll use posterior decoding to obtain a distribution over states at each time step since this will give us a more nuanced picture of how each model interprets the data.

```
In: xs, ys = data[0]
    fbs = model.forward_backward(ys)
    fbs_hat = model_hat.forward_backward(ys)

    fig, axs = plt.subplots(4, 1, figsize=(6.4, 9.6), sharex=True)

    axs[0].plot(ys)
    for state in t_dists:
        axs[1].plot([x == state for x in xs], label=state)
    for state, line in sorted(fbs.items()):
        axs[2].plot(line, label=state)
    for state, line in sorted(fbs_hat.items()):
        axs[3].plot(line, label=state)
    axs[3].set_xlabel('Time step')
    axs[0].set_ylabel('Emission')
    axs[1].set_ylabel('Label')
    axs[2].set_ylabel('Probability')
    axs[3].set_ylabel('Probability')
    axs[1].legend(title='true states', **legend_kwargs)
    axs[2].legend(title='model', **legend_kwargs)
    axs[3].legend(title='model_hat', **legend_kwargs);
```

Out:

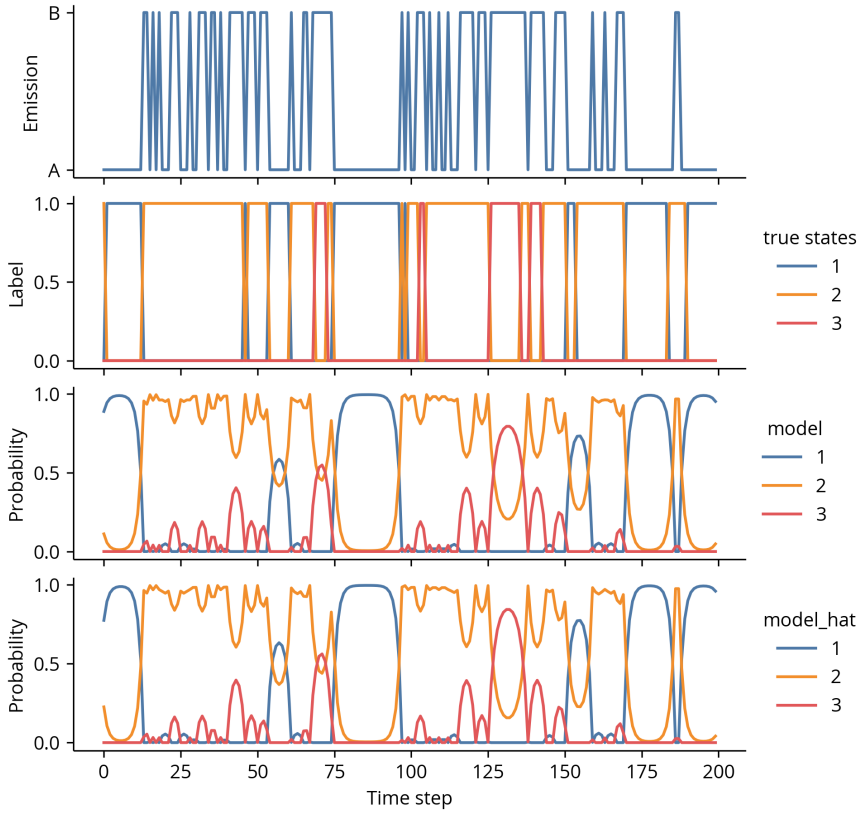

The posterior decoding curves are effectively identical. There are, of course, some minor differences but no outstanding patterns. Generally these models are good at detecting the time steps corresponding to state 1 but much worse at distinguishing between states 2 and 3. We can understand this qualitatively by examining the original model parameters. State 1 is highly "sticky" and only emits As, so long runs of As are extremely likely to correspond to state 1. State 3 only emits Bs, but it's fairly likely to switch to state 2. Since state 2 is equally likely to emit an A as a B, it's difficult to know if a B was emitted because the model remained in state 3 or because it switched to state 2. This shows that state inference can be highly variable even if the parameters are known exactly.

Discrete emission distribution

For the next example, we'll derive and implement the MLE for the parameter of a *Poisson distribution*. Poisson distributions are commonly used to model count data with no upper bound. The underlying assumptions are the counts represent events that occur with some average rate over time and the number of events in one interval is independent of the number of events in any other non-overlapping interval. These conditions impose few restrictions, so Poisson distributions are used to model a variety of phenomena, ranging from the number of particle decays in a radioactive sample to the number of requests arriving at a web server.

If the events of a Poisson process X occur at an average rate of λ, then the probability that x events are observed in an interval of length t is given by

$$\begin{aligned} P(X = x|\lambda, t) &= f(x, \lambda, t) \\ &= e^{-\lambda t}\frac{(\lambda t)^x}{x!}. \end{aligned}$$

The rate λ and length of the interval t always appear as the product λt, so Poisson distributions are often parameterized in terms of λ only. Confusingly, this is frequently still called a rate even though it's actually a unitless quantity. To match these conventions, we'll also drop t as a parameter, although we'll avoid referring to λ as a rate.

We can now write the log-likelihood function explicitly:

$$\begin{aligned} L(\lambda) &= \sum_{i=1}^{N} \log f(x_i, \lambda) \\ &= \sum_{i=1}^{N} \log\left(e^{-\lambda}\frac{\lambda_i^x}{x_i!}\right) \\ &= \sum_{i=1}^{N} -\lambda + x_i \log\lambda - \log(x_i!) \\ &= -N\lambda + \sum_{i=1}^{N} x_i \log\lambda - \log(x_i!). \end{aligned}$$

To find the MLE for λ, we 1) take the derivative relative to λ and 2) solve for λ when this expression is zero. Since in the second step we solve for specific values where the derivative is zero, we replace λ with $\hat{\lambda}$ to clarify this distinction.

Step 1: Differentiate the log-likelihood function

$$\frac{dL(\lambda)}{d\lambda} = -N + \sum_{i=1}^{N}\frac{x_i}{\lambda}$$

Step 2: Solve for the MLE

$$\begin{aligned} 0 &= -N + \sum_{i=1}^{N}\frac{x_i}{\hat{\lambda}} \\ N &= \frac{\sum_{i=1}^{N} x_i}{\hat{\lambda}} \\ \hat{\lambda} &= \frac{\sum_{i=1}^{N} x_i}{N} = \bar{x} \end{aligned}$$

Pleasingly, the MLE for λ is the average of the observations. Now let's implement this in code using a model with two arbitrary states. This will follow the same format as the previous section, so we'll proceed with little comment.

In:
```
t_dists = {1: {1: 0.95, 2: 0.05},
           2: {1: 0.25, 2: 0.75}}
e_dists = {1: stats.poisson(3),
           2: stats.poisson(0.5)}
start_dist = {1: 0.5, 2: 0.5}

model = HMM(t_dists=t_dists, e_dists=e_dists, start_dist=start_dist)

data = [model.simulate(200, random_state=i) for i in range(10)]
data = [list(zip(*example)) for example in data]
```

The estimate for each state's λ is simply the average of the emissions associated with that state. However, the emissions are separated across multiple examples and not organized by state, so we'll first gather them in a dictionary keyed by state and then take the average.

In:
```
# Make emission dicts keyed by state
state2emits = {}
for state in t_dists:
    state2emits[state] = []

# Add emissions
for example in data:
    xs, ys = example
    for state, emit in zip(xs, ys):
        state2emits[state].append(emit)

# Average emissions
lambda_hats = {}
for state, emits in state2emits.items():
    lambda_hat = sum(emits) / len(emits)
    lambda_hats[state] = lambda_hat
lambda_hats
```

Out:
```
{1: 2.991077119184194, 2: 0.46635730858468677}
```

Though this form of the parameter estimates is convenient for inspection, discrete emission distributions over an infinite domain are implemented as SciPy random variables in Homomorph.

In:
```
e_dists_hat = {}
for state, lambda_hat in lambda_hats.items():
    e_dists_hat[state] = stats.poisson(lambda_hat)
```

The estimators for the transition and start distributions are the same, so we can copy those cells from the previous example.

In:
```
# Make transition count dicts and add pseudocounts
t_pseudo = 0.1
t_counts = {}
for state1, t_dist in t_dists.items():
    t_count = {}
    for state2 in t_dist:
        t_count[state2] = t_pseudo
    t_counts[state1] = t_count

# Add observed counts
for example in data:
    xs, ys = example
    state0 = xs[0]
    for state1 in xs[1:]:
        t_counts[state0][state1] += 1
        state0 = state1

# Normalize counts
t_dists_hat = {}
for state1, t_count in t_counts.items():
    t_sum = sum(t_count.values())
    t_dist_hat = {}
    for state2, count in t_count.items():
        t_dist_hat[state2] = count / t_sum
    t_dists_hat[state1] = t_dist_hat
t_dists_hat
```

Out:
```
{1: {1: 0.9487589559877175, 2: 0.0512410440122825},
 2: {1: 0.19452247191011232, 2: 0.8054775280898876}}
```

In:
```
# Make start count dicts and add pseudocounts
start_pseudo = 0.1
start_count = {}
for state in start_dist:
    start_count[state] = start_pseudo

# Add observed counts
for example in data:
    xs, ys = example
    start_count[xs[0]] += 1

# Normalize counts
start_sum = sum(start_count.values())
start_dist_hat = {}
for state, count in start_count.items():
    start_dist_hat[state] = count / start_sum
start_dist_hat
```

Out: {1: 0.303921568627451, 2: 0.696078431372549}

With the parameter estimates in hand, we can instantiate an estimated model and compare the decoded states to those from the actual model and the true states.

In:
```
model_hat = HMM(t_dists=t_dists_hat,
                e_dists=e_dists_hat,
                start_dist=start_dist_hat)

xs, ys = data[0]
fbs = model.forward_backward(ys)
fbs_hat = model_hat.forward_backward(ys)

fig, axs = plt.subplots(4, 1, figsize=(6.4, 9.6), sharex=True)

axs[0].plot(ys)
for state in t_dists:
    axs[1].plot([x == state for x in xs], label=state)
for state, line in sorted(fbs.items()):
    axs[2].plot(line, label=state)
for state, line in sorted(fbs_hat.items()):
    axs[3].plot(line, label=state)
axs[3].set_xlabel('Time step')
axs[0].set_ylabel('Emission')
axs[1].set_ylabel('Label')
axs[2].set_ylabel('Probability')
axs[3].set_ylabel('Probability')
axs[1].legend(title='true states', **legend_kwargs)
axs[2].legend(title='model', **legend_kwargs)
axs[3].legend(title='model_hat', **legend_kwargs);
```

Out:

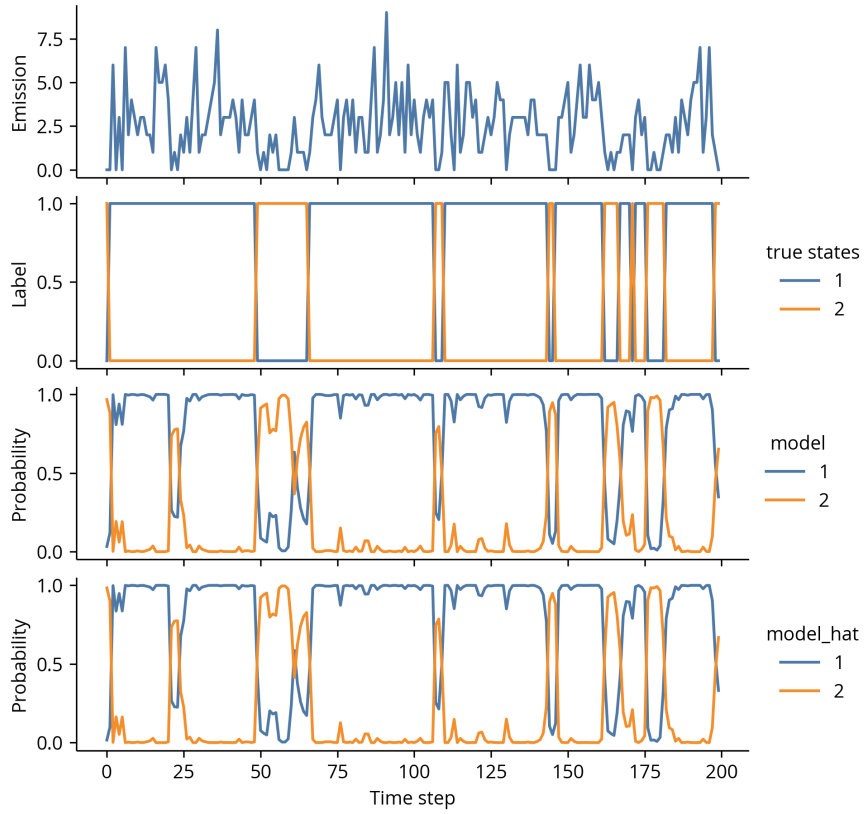

Continuous emission distribution

The normal distribution, with its iconic bell-shaped density curve, is practically synonymous with statistics. This association is deserved as the normal distribution is the foundation of many significant results and methods in both mathematical and applied statistics. For our purposes, however, we only need to know that the normal distribution is a common and robust model for continuous measurements, so in this example we'll derive the MLEs for its parameters.

As seen in the previous example, once the MLEs are derived, the implementations are often straightforward translations from mathematical symbols to code. In fact, for many common distributions, including the normal distribution, the MLEs have closed-form expressions that can be interpreted in terms of familiar statistical quantities like the mean or variance. Thus, for this example we'll skip the implementations and only present the derivations.

Let's first review the probability density function of a normal distribution:

$$f(x, \mu, \sigma^2) = \frac{1}{\sqrt{2\pi\sigma^2}} e^{-\frac{(x-\mu)^2}{2\sigma^2}}.$$

Though the expression may look intimidating, the important take-away is the distribution has two parameters μ and σ^2, which are equal to its mean and variance, respectively. In qualitative terms, μ controls the position of the peak of the curve and σ^2 controls its width.

We will now substitute the density into the log-likelihood function:

$$\begin{aligned} L(\mu, \sigma^2) &= \sum_{i=1}^{N} \log f(x_i, \mu, \sigma^2) \\ &= \sum_{i=1}^{N} -\frac{1}{2}\log(2\pi) - \frac{1}{2}\log(\sigma^2) - \frac{(x_i - \mu)^2}{2\sigma^2} \\ &= -\frac{N}{2}\log(2\pi) - \frac{N}{2}\log(\sigma^2) - \sum_{i=1}^{N} \frac{(x_i - \mu)^2}{2\sigma^2}. \end{aligned}$$

As the density function has two parameters, μ and σ^2, the log-likelihood is a function of these variables. This changes the next step slightly from the previous example since we have to take the partial derivative relative to each and solve the resulting system of equations. In this case the algebra works out nicely, but sometimes numerical optimization techniques are required.

We'll start with the partial derivative for μ. A subtle point for distributions with multiple parameters is in the second step when the derivative is set to zero, we replace each parameter with its estimated counterpart since we're solving for specific points where the derivatives relative to each parameter are simultaneously zero.

Step 1: Differentiate the log-likelihood function

$$\frac{\partial L}{\partial \mu} = \sum_{i=1}^{N} \frac{(x_i - \mu)}{\sigma^2}$$

Step 2: Solve for the MLE

$$\begin{aligned} 0 &= \sum_{i=1}^{N} \frac{(x_i - \hat{\mu})}{\hat{\sigma}^2} \\ N\hat{\mu} &= \sum_{i=1}^{N} x_i \\ \hat{\mu} &= \frac{\sum_{i=1}^{N} x_i}{N} = \bar{x} \end{aligned}$$

Now let's find the MLE for σ^2. Another nuance for the normal distribution in particular is the derivative is taken relative to the variance, σ^2, and not the standard deviation, σ. Though this choice does not impact the resulting formula, it both simplifies the calculation and reflects the natural role of the variance as the more fundamental statistical quantity.

Step 1: Differentiate the log-likelihood function

$$\frac{\partial L}{\partial \sigma^2} = -\frac{N}{2\sigma}^2 + \sum_{i=1}^{N} \frac{(x_i - \mu)^2}{2\sigma^4}$$

Step 2: Solve for the MLE

$$
\begin{aligned}
0 &= -\frac{N}{2\hat{\sigma}^2} + \sum_{i=1}^{N} \frac{(x_i - \hat{\mu})^2}{2\hat{\sigma}^4} \\
\frac{N}{\hat{\sigma}^2} &= \sum_{i=1}^{N} \frac{(x_i - \hat{\mu})^2}{\hat{\sigma}^4} \\
\hat{\sigma}^2 &= \frac{\sum_{i=1}^{N} (x_i - \hat{\mu})^2}{N}
\end{aligned}
$$

As hinted in the introduction for this section, the MLEs for μ and σ^2 are simply the mean and variance of the data! Notice the MLE for σ^2 includes $\hat{\mu}$, so in practice we would calculate $\hat{\mu}$ first and substitute that value in the expression for $\hat{\sigma}^2$. Those with some background in statistics might notice the formula for $\hat{\sigma}^2$ has a factor of N rather than $N-1$ in the denominator. This is no typo. It turns out that while MLEs are optimal in many ways, they are not always unbiased, meaning they can on average be higher or lower than the true value. In this case, the MLE for σ^2 is low by a factor of exactly $\frac{N-1}{N}$ on average, so some formulas divide by this quantity to remove the bias. This actually makes our estimate more imprecise, so there are some trade-offs involved in using one formula over the other. The good news is the difference is trivial for most data sets of realistic size, so the choice is largely inconsequential.

3.5 Training with unknown states

3.5.1 Estimation-maximization, informally

When we knew the states, we could assign each emission to a log-likelihood function and optimize the parameters of these functions separately. However, when the states are unknown, the problem of estimating parameters is much harder because we can't decompose the log-likelihood into independent terms. (We'll see this formally in the next section.) Not all hope is lost though. Remember that we can estimate parameters when we know the states, and when we know parameters we can estimate state probabilities. While this may seem like a chicken and egg problem, we can use this relationship as an iterative method for estimating parameters when the states are unknown. In practice, it works as the following:

1. Make an informed guess of the initial parameters.
2. Use the current parameters to estimate posterior state probabilities.
3. Use the posterior state probabilities to improve the parameter estimates.
4. Repeat steps 2 and 3 a fixed number of times or until some convergence criteria is met.

In the context of HMMs, this procedure is known as the *Baum-Welch algorithm*, but it's a special case of a more general technique called *estimation-maximization* (EM). Though it intuitively makes sense, it's not at all clear that it will work in practice. For example, the likelihood function could ping-pong up and down without ever settling down to a single value. Fortunately, each iteration is guaranteed to improve the likelihood. Unfortunately, the sequence may converge to a local rather than a global maximum, *i.e.* a good answer but not necessarily the best. Thus, it's common to

run the algorithm multiple times with different initial parameters and choose the final parameters as those with the largest likelihood.

Hopefully this discussion has given a conceptual overview of the Baum-Welch algorithm. Clearly we've skipped many details, so in the next section we'll implement it from scratch for categorical distributions. Then in the following sections, we'll introduce the EM algorithm formally and use it to derive the update equations for a normal distribution.

3.5.2 Implementing Baum-Welch for categorical distributions

The steps in the Baum-Welch algorithm as presented above should at this point make sense except step 3. How exactly do we use posterior decoding to improve the parameter estimates? For a generic distribution, we'll need the EM formalism to derive the update equations properly, but for a categorical distribution we can intuit our way to the answer. We'll start with the transition distributions since we've already seen their MLEs, but then we'll derive a similar result for the emission distributions. Recall that the MLEs for the parameters of a transition distribution are written in terms of the number of observed transitions between states i and j, n_{ij}:

$$\hat{a}_{ij} = \frac{n_{ij}}{\sum_{j=1}^{S} n_{ij}}.$$

Unfortunately, we don't have access to these counts since the states are unknown. However, what if we replaced these counts with how often we thought they happened under our current parameter estimates? For example, if between time t and $t+1$, we calculate there's a 75% chance the process remained in state 1 and a 25% chance it transitioned to state 2, that's effectively a 0.75 count towards n_{11} and a 0.25 count towards n_{12}. Although we originally defined the n_{ij} variables in terms of whole numbers, the equations still yield valid estimates with fractional counts.

Now the name of the game is to calculate these probabilities over all time steps. Formally we're looking for:

$$\begin{aligned}
n_{ij} &= \sum_{t=1}^{T-1} P(X_t = i, X_{t+1} = j | Y = y, \Theta) \\
&= \frac{1}{P(Y = y|\Theta)} \sum_{t=1}^{T-1} P(X_t = i, X_{t+1} = j, Y = y|\Theta) \\
&= \frac{1}{P(Y = y|\Theta)} \sum_{t=1}^{T-1} \Big[P(X_t = i, Y_1 = y_1, \ldots, Y_t = y_t|\Theta) \\
&\quad \times P(X_{t+1} = j, Y_{t+1} = y_{t+1}, \ldots, Y_T = y_T | X_t = i, Y_1 = y_1, \ldots, Y_t = y_t, \Theta) \Big] \\
&= \frac{1}{P(Y = y|\Theta)} \sum_{t=1}^{T-1} \Big[P(X_t = i, Y_1 = y_1, \ldots, Y_t = y_t|\Theta) \\
&\quad \times P(X_{t+1} = j, Y_{t+1} = y_{t+1}, \ldots, Y_T = y_T | X_t = i, \Theta) \Big].
\end{aligned}$$

The first term is the forward variable evaluated at time t and state i, which we'll denote by $f_i(t)$. We haven't formally introduced this quantity in this tutorial, but we can easily obtain these values with the `forward` method of an `HMM` instance. Incidentally, $P(Y = y|\Theta) = \sum_i f_i(T)$ since this sums the probability of the entire emission sequence over all possible final states. Let's now focus on the second term in the sum and define the following events to clean up the notation:

- $A : Y_{t+2} = y_{t+2}, \ldots, Y_T = y_t$
- $B : Y_{t+1} = y_{t+1}$
- $C : X_{t+1} = j$
- $D : X_t = i$.

Thus, we have

$$\begin{aligned} P(X_{t+1} = j, Y_{t+1} = y_{t+1}, \ldots, Y_T = y_T | X_t = i, \Theta) &= P(A, B, C|D, \Theta) \\ &= P(A|B, C, D, \Theta) \cdot P(B|C, D, \Theta) \cdot P(C|D, \Theta) \\ &= P(A|C, \Theta) \cdot P(B|C, \Theta) \cdot P(C|D, \Theta). \end{aligned}$$

From right to left, the third term is a_{ij}, the second term is $e_j(y_{t+1})$, and the first term is the backward variable evaluated at time $t + 1$ and state j, which we'll denote by $b_j(t + 1)$. Analogous to the forward variable, the backward variable is available via the `backward` method of an `HMM` instance.

Putting everything together we have

$$n_{ij} = \frac{1}{P(Y = y|\Theta)} \sum_{t=1}^{T-1} f_i(t) a_{ij} e_j(y_{t+1}) b_j(t + 1).$$

Now let's tackle the emission distributions. When the states are known, the MLEs are the same, but instead of counting transitions between states, we count emissions. (The emissions essentially take on the role of the target state j.) When the states are unknown, we replace these counts with how much we think each state is responsible for each emission. In other words, if at time t we observe emission i and we calculate an 90% chance of state 1 and a 10% chance of state 2, we assign a 0.9 count towards n_{1i} and a 0.1 count towards n_{2i}. Written mathematically,

$$
\begin{aligned}
n_{ij} &= \sum_{t:y_t=j} P(X_t = i|Y = y, \Theta) \\
&= \frac{1}{P(Y = y|\Theta)} \sum_{t:y_t=j} P(X_t = i, Y = y|\Theta) \\
&= \frac{1}{P(Y = y|\Theta)} \sum_{t:y_t=j} P(Y_1 = y_1, \ldots, Y_t = y_t, X_t = i|\Theta) P(Y_{t+1} = y_{t+1}, \ldots, Y_T = y_T|X_t = i, \Theta) \\
&= \frac{1}{P(Y = y|\Theta)} \sum_{t:y_t=j} f_i(t) b_i(t).
\end{aligned}
$$

With these results, we can implement the Baum-Welch algorithm. For continuity, we'll use the same example from the MLE section.

```
In: t_dists = {1: {1: 0.95, 2: 0.05},
               2: {1: 0.05, 2: 0.9, 3: 0.05},
               3: {2: 0.35, 3: 0.65}}
    e_dists = {1: {'A': 1},
               2: {'A': 0.5, 'B': 0.5},
               3: {'B': 1}}
    start_dist = {1: 0.2, 2: 0.5, 3: 0.3}

    model = HMM(t_dists=t_dists, e_dists=e_dists, start_dist=start_dist)

    data = [model.simulate(200, random_state=i) for i in range(10)]
    data = [list(zip(*example)) for example in data]
```

To start the algorithm, we first need a model structure and initial estimates for its parameters. To keep the Baum-Welch approach on equal footing with the previous example, we'll assume we know the disallowed transitions but not the disallowed emissions. For the initial estimates, we'll use uniform random values to keep the code simple, but more sophisticated approaches can use specific distributions for each parameter. Though it's good practice to use the best result from several different random initializations, if the initial parameters are hard coded, the states must be different from each other in some way. If the states are all identical, there's no way for the model to break symmetry, and all the updates will yield parameters that are the same as the initial ones.

```
In: random.seed(1)

    # Make transition count dicts and add pseudocounts
    t_counts = {}
    for state1, t_dist in t_dists.items():
        t_count = {}
        for state2 in t_dist:
            t_count[state2] = random.random()
        t_counts[state1] = t_count

    # Normalize counts
```

```
t_dists_hat = {}
for state1, t_count in t_counts.items():
    t_sum = sum(t_count.values())
    t_dist_hat = {}
    for state2, count in t_count.items():
        t_dist_hat[state2] = count / t_sum
    t_dists_hat[state1] = t_dist_hat
t_dists_hat
```

Out:
```
{1: {1: 0.13685528663315571,
     2: 0.8631447133668443},
 2: {1: 0.5043817911017634,
     2: 0.16844258615115162,
     3: 0.3271756227470851},
 3: {2: 0.4082259386891194,
     3: 0.5917740613108805}}
```

In:
```
random.seed(2)

# Collect all possible emissions
e_set = set()
for example in data:
    xs, ys = example
    e_set.update(ys)

# Make emission count dicts and add pseudocounts
e_counts = {}
for state in t_dists:
    e_counts[state] = {emit: random.random() for emit in e_set}

# Normalize counts
e_dists_hat = {}
for state, e_count in e_counts.items():
    e_sum = sum(e_count.values())
    e_dist_hat = {}
    for emit, count in e_count.items():
        e_dist_hat[emit] = count / e_sum
    e_dists_hat[state] = e_dist_hat
e_dists_hat
```

Out:
```
{1: {'A': 0.5021552995618842, 'B': 0.49784470043811585},
 2: {'A': 0.39987288219487493, 'B': 0.6001271178051251},
 3: {'A': 0.531667470841593, 'B': 0.4683325291584069}}
```

In:
```
random.seed(3)

# Make start count dicts and add pseudocounts
start_count = {}
for state in start_dist:
```

```
    start_count[state] = random.random()

# Normalize counts
start_sum = sum(start_count.values())
start_dist_hat = {}
for state, count in start_count.items():
    start_dist_hat[state] = count / start_sum
start_dist_hat
```

```
Out: {1: 0.2065397992628295, 2: 0.47236009956297115, 3: 0.32110010117419935}
```

Let's now code the main loop, beginning with the definition of the stopping conditions. We can operationally define convergence as when the improvement in the log-likelihood is below some threshold, `epsilon`. In practice, this may take too long, so we'll also define a maximum number of iterations, `maxiter`. What follows, then, is a fairly straightforward implementation of the equations we derived previously. There are two nuanced points, however. First, to preserve the model structure, the counts are always taken over the allowed transitions or emissions. (In theory, disallowed transitions or emissions should always have a probability of zero, but floating point errors may yield unexpected results.) Second, the forward and backward variables are scaled to sum to one at each time step for numerical stability. Thus, the true value at time t is a product of the raw value and all scaling factors up to and including time t. (Since the backward variable is calculated recursively from the final instead of the first observation, the product is taken from t to T.) A side effect of this representation is $P(Y = y|\Theta)$ is simply the product of all scaling factors.

For brevity, the input code is given in Appendix C, and only the final values are shown below.

```
Out: FINAL VALUES
     log-likelihood: -906.2061302148018
     delta log-likelihood: 0.009596164686740849
     t_dists: {1: {1: 0.19048033686643145,
                   2: 0.8095196631335685},
               2: {1: 0.730991899350023,
                   2: 0.168079808479332,
                   3: 0.10092829217064504},
               3: {2: 0.04584548747372808,
                   3: 0.9541545125262719}}
     e_dists: {1: {'A': 0.28936393517521436,
                   'B': 0.7106360648247857},
               2: {'A': 0.48150408200102607,
                   'B': 0.5184959179989739},
               3: {'A': 0.9999943519811173,
                   'B': 5.648018882737235e-06}}
     start_dist: {1: 0.7875017247391405,
                  2: 0.005518967674210817,
                  3: 0.20697930758664865}
```

Based on the results, the algorithm seems to have merged states 2 and 3 into a single state that emits a mixture of A and B. State 1 was largely estimated correctly, but it's labeled as state 3 in the estimated model. There are two factors which may explain this result. First, the initial values were chosen poorly. We generated them randomly, so we were potentially unlucky, and there was

a "bad" local maximum near those initial values. Additionally, since we didn't prime the initial values with any information that state 1 only emits A and state 3 only emits B, the algorithm exchanged them. For both these reasons, it's best practice to use multiple initializations that are random but still encode the expected behavior for each state. Try playing around with different random seeds or initialization schemes to see if the fit improves!

The second reason why the algorithm merged states 2 and 3 is state 2 is inherently difficult to fit. Under the current parameters, state 2 is just as likely to emit an A as a B, which maximizes the uncertainty associated with its emissions. (Compare this to states 1 or 3 whose emissions we know with certainty.) While this example is highly artificial, it illustrates that although we can define an HMM however we like, its emission distribution may be well-described by multiple sets of parameters, *i.e.*, the likelihood surface is broad and flat or has multiple peaks.

3.5.3 Estimation-maximization, formally

Though what we've done so far makes sense intuitively, let's look at what's happening more formally in order to generalize this approach to other emission distributions. Recall that in maximum likelihood estimation, we find parameters $\hat{\Theta}$ that maximize the logarithm of probability of the data, D:

$$\begin{aligned}\hat{\Theta} &= \underset{\Theta}{\operatorname{argmax}}\, L(\Theta) \\ &= \underset{\Theta}{\operatorname{argmax}} \log P(D|\Theta).\end{aligned}$$

In the HMM setting with known states, the data are composed of N examples of ordered pairs $\{(x_i, y_i) : 1 \leq i \leq N\}$ where x_i is a sequence of states and y_i is a sequence of emissions, each with length T_i. For simplicity, however, we will only consider a single example (x, y) where x_t and y_t indicate the tth state and emission in those sequences, respectively. The log-likelihood function is then written as $L(\Theta) = \log P(X = x, Y = y|\Theta)$. So far this is all review from the previous section. What about the case when we only know the emissions, y? Then the log-likelihood is $L(\Theta) = \log P(Y = y|\Theta)$. Though we can calculate this quantity directly with the forward algorithm and thus in principle apply a number of optimization algorithms, we instead will take a probabilistic approach and write the log-likelihood function as a sum over all possible state sequences:

$$\begin{aligned}L(\Theta) &= \log P(Y = y|\Theta) \\ &= \log \sum_x P(Y = y, X = x|\Theta).\end{aligned}$$

The only problem is that for an emission sequence of length T and a model with S hidden states, there are S^T possible state sequences. This sum therefore has an exponential number of terms and is intractable for any data of realistic size.

Thus, this expression hasn't gotten us anywhere yet. However, it's possible to derive a related but more tractable quantity whose improvements lower bound improvements for the log-likelihood. This quantity, commonly denoted as $Q(\Theta|\Theta_n)$, is defined as the expectation of the log-likelihood function with respect to the conditional distribution of the states, X, given the emissions, y:

$$\begin{aligned} Q(\Theta|\Theta_n) &= E_{X|Y=y,\Theta_n} \log P(Y = y, X|\Theta) \\ &= \sum_x P(X = x|Y = y, \Theta_n) \log P(Y = y, X = x|\Theta). \end{aligned}$$

This is a confusing expression, especially since the notation for conditional expectation is dense. However, in the second line the expectation is written explicitly, showing it is simply a sum of the joint log-likelihoods of the states and emissions given the parameters where each is weighted by the quantity $P(X = x|Y = y, \Theta_n)$. Notice that $P(X = x|Y = y, \Theta_n)$ is constant for a given Θ_n, so $Q(\Theta|\Theta_n)$ is function only of the log-likelihood terms.

Next we define the new estimates of the parameters as

$$\Theta_{n+1} = \underset{\Theta}{\operatorname{argmax}}\, Q(\Theta|\Theta_n).$$

These two steps are where the name expectation-maximization is derived since the first is the calculation of an expectation, and the second is a maximization of that expectation. It may seem like we haven't done much to simplify the problem since we're still dealing with sums over all state sequences. However, by moving the sum outside the logarithm, we've greatly simplified the maximization step as we will see in the next section.

By repeating this process, we can iteratively improve our estimates of the parameters. As mentioned earlier, these improvements in $Q(\Theta|\Theta_n)$ lower bound improvements in the log-likelihood. We won't show the derivation here, but formally this means

$$\log P(Y|\Theta) - \log P(Y|\Theta_n) \geq Q(\Theta|\Theta_n) - Q(\Theta_n|\Theta_n).$$

Since in each step $Q(\Theta|\Theta_n)$ is maximized, the right quantity is always non-negative. Thus, the log-likelihood of the emissions is improved by at least that much as well. Written mathematically,

$$Q(\Theta_{n+1}|\Theta_n) - Q(\Theta_n|\Theta_n) \geq 0 \implies \log P(Y|\Theta_{n+1}) - \log P(Y|\Theta_n) \geq 0.$$

3.5.4 Deriving the update equations for a normal distribution

We'll now apply this theory to the HMM context. First we'll show not only that $Q(\Theta|\Theta_n)$ is tractable to calculate but also that it decomposes into independent terms. Then we'll derive the update equations for normal emission distributions. Let's get started!

We first expand the expression for $Q(\Theta|\Theta_n)$ using the probabilistic structure of an HMM:

$$
\begin{aligned}
Q(\Theta|\Theta_n) &= \sum_x P(X = x|Y = y, \Theta_n) \log P(Y = y, X = x|\Theta) \\
&= \sum_x P(X = x|Y = y, \Theta_n) \log \Big[P(Y_1 = y_1|X_1 = x_1, \Theta) P(X_1 = x_1|\Theta) \\
&\quad \prod_{t=1}^{T-1} P(Y_{t+1} = y_{t+1}|X_{t+1} = x_{t+1}, \Theta) P(X_{t+1} = x_{t+1}|X_t = x_t, \Theta) \Big] \\
&= \sum_x P(X = x|Y = y, \Theta_n) \Big[\log P(X_1 = x_1|\Theta) \\
&\quad + \sum_{t=1}^{T} \log P(Y_t = y_t|X_t = x_t, \Theta) + \sum_{t=1}^{T-1} \log P(X_{t+1} = x_{t+1}|X_t = x_t, \Theta) \Big] \\
&= \sum_i P(X_1 = i|Y = y, \Theta_n) \log P(X_1 = i|\Theta) \\
&\quad + \sum_i \sum_{t=1}^{T} P(X_t = i|Y = y, \Theta_n) \log P(Y_t = y_t|X_t = i, \Theta) \\
&\quad + \sum_{i,j} \sum_{t=1}^{T-1} P(X_t = i, X_{t+1} = j|Y = y, \Theta_n) \log P(X_{t+1} = j|X_t = i, \Theta).
\end{aligned}
$$

In the final step, the outer sum was distributed over each term and exchanged with the inner sum. This step is shown explicitly for the second term below:

$$
\begin{aligned}
&\sum_x P(X = x|Y = y, \Theta_n) \sum_{t=1}^{T} \log P(Y_t = y_t|X_t = x_t, \Theta) \\
&= \sum_x \sum_{t=1}^{T} P(X = x|Y = y, \Theta_n) \log P(Y_t = y_t|X_t = x_t, \Theta) \\
&= \sum_i \sum_{x \setminus x_t} \sum_{t=1}^{T} P(X = x|Y = y, \Theta_n) \log P(Y_t = y_t|X_t = i, \Theta) \\
&= \sum_i \sum_{t=1}^{T} \log P(Y_t = y_t|X_t = i, \Theta) \sum_{x \setminus x_t} P(X = x|Y = y, \Theta_n) \\
&= \sum_i \sum_{t=1}^{T} P(X_t = i|Y = y, \Theta_n) \log P(Y_t = y_t|X_t = i, \Theta).
\end{aligned}
$$

(The final line used that the probability of a state sequence with a fixed state $X_t = i$ is the sum of the probabilities of all state sequences that include that fixed state.)

Though moving the sum over all state sequences outside the logarithm seemed like a minor mathematical detail, it, in combination with the probabilistic structure of an HMM, makes its com-

putation tractable. Another consequence is that if all transitions and emissions are governed by different parameters, we can maximize the entire expression by optimizing the corresponding sum for each state or pair of states individually. The fractional "counts" $P(X_t = i|Y = y, \Theta)$ and $P(X_t = i, X_{t+1} = j|Y = y, \Theta)$ defined in the previous section are even the coefficients of the log-likelihood terms, which is directly related to their appearance in the update equations.

Now that we've demonstrated that each term can be optimized separately, we'll derive the update equations for a normal emission distribution. We begin by writing the term we wish to optimize for a fixed state i, which we call $q(\Theta)$:

$$q(\Theta) = \sum_{t=1}^{T} P(X_t = i|Y = y, \Theta_n) \log P(Y_t = y_t|X_t = i, \Theta).$$

We'll write $w_{it} = P(X_t = i|Y = y, \Theta_n)$ to simplify the notation and to emphasize this quantity is fixed during the maximization step. We'll also substitute the expression for a normal density with mean μ_i and variance σ_i^2:

$$\begin{aligned} q(\mu_i, \sigma_i^2) &= \sum_{t=1}^{T} P(X_t = i|Y = y, \Theta_n) \log P(Y_t = y_t|X_t = i, \Theta) \\ &= \sum_{t=1}^{T} w_{it} \log \left(\frac{1}{\sqrt{2\pi\sigma^2}} e^{-\frac{(y-\mu)^2}{2\sigma^2}} \right) \\ &= \sum_{t=1}^{T} w_{it} \left(-\frac{1}{2} \log \sigma^2 - \frac{1}{2} \log 2\pi - \frac{(y_t - \mu_i)^2}{2\sigma^2} \right). \end{aligned}$$

This quantity should look extremely familiar from the section on deriving the MLEs for a normal distribution! However, let's bring it home and take some derivatives. We'll start with the parameter for the mean.

Step 1: Differentiate the log-likelihood function

$$\frac{\partial q}{\partial \mu_i} = \sum_{t}^{T} w_{it} \frac{(y_t - \mu_i)}{\sigma_i^2}$$

Step 2: Solve for the MLE

$$\begin{aligned}
0 &= \sum_{t=1}^{T} w_{it} \frac{(y_t - \hat{\mu}_i)}{\hat{\sigma}_i^2} \\
0 &= \sum_{t=1}^{T} w_{it} (y_t - \hat{\mu}_i) \\
\sum_{t=1}^{T} w_{it} \hat{\mu}_i &= \sum_{t=1}^{T} w_{it} y_t \\
\hat{\mu}_i &= \frac{\sum_{t=1}^{T} w_{it} y_t}{\sum_{t=1}^{T} w_{it}}
\end{aligned}$$

The resulting formula is very similar to the corresponding MLE derived in the previous section. However, here each observation is multiplied by a weight, and the sum is divided by the total weight rather than the number of observations. (In fact, setting the weight for each observation to one recovers the original formula!) Since the weights for each observation must sum to one, we've essentially partitioned each observation across all states where the amount that an observation contributes to a state is given by our confidence that it was generated by that state.

Let's now derive the update equation for the variance.

Step 1: Differentiate the log-likelihood function

$$\frac{\partial q}{\partial \sigma_i^2} = \sum_{t=1}^{T} w_{it} \left(-\frac{1}{2\sigma_i^2} + \frac{(y_t - \mu_i)^2}{2\sigma_i^4} \right)$$

Step 2: Solve for the MLE

$$\begin{aligned}
0 &= \sum_{t=1}^{T} w_{it} \left(-\frac{1}{2\hat{\sigma}_i^2} + \frac{(y_t - \hat{\mu}_i)^2}{2\hat{\sigma}_i^4} \right) \\
\frac{1}{\hat{\sigma}_i^2} \sum_{t=1}^{T} w_{it} &= \frac{1}{\hat{\sigma}_i^4} \sum_{t=1}^{T} w_{it} (y_t - \hat{\mu}_i)^2 \\
\hat{\sigma}_i^2 &= \frac{\sum_{t=1}^{T} w_{it} (y_t - \hat{\mu}_i)^2}{\sum_{t=1}^{T} w_{it}}
\end{aligned}$$

Again, the update equation has the same form as the corresponding MLE except each term in the sum is weighted. This is a common occurrence when using the EM algorithm and is a consequence of the construction of the objective function as a weighted sum of log-likelihood functions. Thus, when the MLEs are interpretable as quantities like counts or averages, the corresponding update equations are often weighted versions of those estimators. Of course, it's not always obvious how the weights will come into play, especially for MLEs which don't have an obvious interpretation, so it's good idea to solve the equations or look up a reference rather than guessing.

3.6 Discriminative training

In this next section, we'll cover discriminative training, which is sometimes called conditional maximum likelihood (CML) estimation. Technically the discriminative training method falls under the heading of training with known states since it requires labeled data. However, there are enough differences in the objective function and the optimization algorithm that it deserves its own treatment. As before, the material is largely divided between a section that motivates the problem and develops the theory and a section that translates that theory into code.

3.6.1 Discriminative training theory

Previously, we saw that maximum likelihood estimation and the EM algorithm often obtained parameter estimates which were reasonably close to their true values. However, what if we don't really care about the parameters, and we're instead more interested in using an HMM to predict the hidden states? What if the model we've chosen for our data is wrong, or, even worse, the data are so messy that no tractable statistical model could ever hope to describe it?

The bad news is all these things are frequently true when working with HMMs. While sometimes the parameters are inherently meaningful, more often than not HMMs are a tool to label data. In these cases, it's more important to accurately predict the states than to estimate the underlying parameters. If the data are actually described by the model, this distinction isn't as relevant because with enough data the parameters that yield the most accurate predictions will converge to the true parameters. However, real-world data are almost never fully described by statistical models, and in these cases the parameters that best fit the data are often not those that best predict the states. Furthermore, the phrase "with enough data" is actually a sneaky way of saying "as the number of observations approaches infinity," so for all practical purposes the two parameter sets are solving distinct problems.

Let's clarify these distinctions by writing them formally. Recall that in maximum likelihood estimation for HMMs with known states, we solve the following optimization:

$$\begin{aligned}\hat{\Theta}_{ML} &= \underset{\Theta}{\operatorname{argmax}}\, L(\Theta) \\ &= \underset{\Theta}{\operatorname{argmax}} \log P(X = x, Y = y|\Theta)\end{aligned}$$

where Θ is the set of model parameters and x and y are sequences of states and emissions, respectively, with lengths T. In general, the optimization is conducted over a set of paired state and emission sequences, but since this won't change the key features of the following discussion, for simplicity we'll consider only a single state-emission sequence pair.

In contrast, conditional maximum likelihood solves the following optimization:

$$\begin{aligned}\hat{\Theta}_{CML} &= \underset{\Theta}{\operatorname{argmax}} \log P(X = x|Y = y, \Theta) \\ &= \underset{\Theta}{\operatorname{argmax}} \log \frac{P(X = x, Y = y, \Theta)}{P(Y = y|\Theta)} \\ &= \underset{\Theta}{\operatorname{argmax}} \log P(X = x, Y = y, \Theta) - \log P(Y = y|\Theta).\end{aligned}$$

It's clear the ML and CML objectives are closely related, so let's use this relationship to gain a deeper understanding of how CML parameter estimates differ from their ML counterparts. To ease the following discussion, we'll make the substitutions

$$\log P(X = x, Y = y|\Theta) = L_c(\Theta)$$

and

$$\log P(Y = y|\Theta) = L_f(\Theta).$$

L_c is the joint log-likelihood of the state and emission sequences, so the term is "clamped" by the true states. L_f is the log-likelihood of the emission sequences only, so the term is "free" to account for all possible state sequences. To maximize the difference between L_c and L_f, it seems the optimized parameters should make L_c as large as possible and L_f as small as possible. However, $L_f \geq L_c$ for any choice of Θ because L_f includes the contributions of all possible state sequences. Thus, the best we can do is to make L_c as close as possible to L_f, and this only happens if we minimize the contribution of state sequences which are not the true sequence. In other words, conditional maximum likelihood is maximum likelihood with an added penalty for parameter choices that favor alternate state sequences.

In the maximum likelihood case, we were able to decompose the optimization into independent products under some fairly general assumptions because when the state sequence was known the likelihood was a single product of transition and emission probabilities. Here, however, the free term, L_f, forces us to consider all possible state sequences. As noted in the previous section, the number of state sequences grows exponentially with length, so even if we derived a closed-form solution, we would still have to contend with an intractable number of terms. We can't apply the EM algorithm either because this optimization doesn't depend on any hidden variables.

We'll instead take a route distinct from all the approaches seen so far by using a method called gradient descent. Gradient descent is the workhorse for many modern machine learning techniques, so there are numerous online resources which explain it in detail. However, the basic idea is since the derivative of a function relative to some input is a measure of its response to a change in that input, we can use that information to iteratively improve an initial guess until we reach a minimum. For functions of two variables, the process is often visualized as progressively climbing down a mountain by taking small steps in the direction of steepest descent. The power of this technique is that it's much easier to take derivatives than it is to identify their zeros, so gradient descent can be applied to almost any optimization problem.

Thus, we need to compute derivatives of the conditional likelihood function. Because gradient descent is for finding minima, however, we redefine our maximization as a minimization by multiplying by negative one:

$$\begin{aligned}
\hat{\Theta}_{CML} &= \operatorname*{argmin}_{\Theta} -\log P(X = x|Y = y, \Theta) \\
&= \operatorname*{argmin}_{\Theta} \log P(Y = y|\Theta) - \log P(X = x, Y = y|\Theta) \\
&= \operatorname*{argmin}_{\Theta} L_f(\Theta) - L_c(\Theta) \\
&= \operatorname*{argmin}_{\Theta} L(\Theta).
\end{aligned}$$

It's a small change, but when we write the update equations, we can use the conventional form instead of having to flip the sign of the derivatives.

We're now ready to take derivatives. We'll start with L_f for a generic parameter $\theta \in \Theta$:

$$\begin{aligned}
\frac{\partial L_f}{\partial \theta} &= \frac{1}{P(Y = y|\Theta)} \frac{\partial P(Y = y|\Theta)}{\partial \theta} \\
&= \sum_x \frac{1}{P(Y = y|\Theta)} \frac{\partial P(X = x, Y = y|\Theta)}{\partial \theta} \\
&= \sum_x \frac{P(X = x, Y = y|\Theta)}{P(Y = y|\Theta)} \frac{\partial \log P(X = x, Y = y|\Theta)}{\partial \theta} \\
&= \sum_x P(X = x|Y = y, \Theta) \frac{\partial \log P(X = x, Y = y|\Theta)}{\partial \theta}.
\end{aligned}$$

This expression is almost identical in structure to the function $Q(\Theta|\Theta_n)$ used in the EM algorithm. We can therefore use a similar series of tricks, namely expanding the log of a product as a sum of log terms and exchanging the order of summation, to obtain a tractable expression. To reduce the clutter, we'll also use the shorthand defined in the section on maximum likelihood estimation where $P(X_{t+1} = j|X_t = i) = a_{ij}$ and $e_i(y_t) = P(Y_t = y_t|X_t = i, \Theta)$. After all the algebraic dust settles, we obtain the equation

$$\frac{\partial L_f}{\partial \theta} = \sum_{t,i} \frac{n_i(t)}{e_i(y_t)} \frac{\partial e_i(y_t)}{\partial \theta} + \sum_{t,i,j} \frac{n_{ij}(t)}{a_{ij}} \frac{\partial a_{ij}}{\partial \theta}.$$

The variables $n_i(t)$ and $n_{ij}(t)$ are defined as $P(X_t = i|Y = y, \Theta)$ and $P(X_t = i, X_{t+1} = j|Y = y, \Theta)$. Though this may look like new notation, they are nearly identical to quantities defined in the section on the EM algorithm and can be efficiently calculated with the forward and backward variables.

A similar computation shows the derivative of the clamped log-likelihood is

$$\frac{\partial L_c}{\partial \theta} = \sum_{t,i} \frac{m_i(t)}{e_i(y_t)} \frac{\partial e_i(y_t)}{\partial \theta} + \sum_{t,i,j} \frac{m_{ij}(t)}{a_{ij}} \frac{\partial a_{ij}}{\partial \theta}.$$

$m_i(t)$ and $m_{ij}(t)$ are defined like $n_i(t)$ and $n_{ij}(t)$. However, because the clamped log-likelihood is taken only over the true state sequence, they are in practice indicators of the state or transition at each time step. This means they are one if a state i or transition from state i to state j occurred at time t and zero otherwise.

HMMs are typically parameterized directly in terms of their transition probabilities. In this case, the derivative of the loss function simplifies to

$$\frac{\partial L}{\partial a_{ij}} = -\frac{m_{ij} - n_{ij}}{a_{ij}}$$

where n_{ij} and m_{ij} are sums over all time steps of the previously defined quantities. While this is the derivative we're seeking, there is one issue. For a generic parameter, gradient descent updates are written in the form

$$\theta_{t+1} = \theta_t - \eta \frac{\partial L}{\partial \theta_t}$$

where η is the *learning rate*, which controls the size of the steps down the mountain. When η is large, we make bold steps at the cost of sometimes going uphill if the loss landscape is bumpy. By making η small, we can ensure we always go downhill but potentially at a glacial pace. Our problem is this update equation does not incorporate the constraints $a_{ij} \geq 0$ and $\sum_j a_{ij} = 1$. In other words, there's nothing stopping a gradient descent update from making a transition probability greater than one or, even worse, negative. If that happens, we've moved outside the parameter space of our model, so there's no guarantee the gradient descent updates would remain meaningful for our optimization even if every mathematical operation were defined.

This is a fundamental shortcoming of derivative-based methods, and there are many variants of gradient descent, *e.g.* projected gradient descent, which address constrained optimization. Fortunately, in this case the constraints allow us to still use vanilla gradient descent via a clever variable transformation. We instead define

$$a_{ij} = \frac{e^{z_{ij}}}{\sum_{j'} e^{z_{ij'}}}$$

and perform gradient descent on the auxiliary variables z_{ij}. (Note that the symbol e without any subscripts refers to the constant and not an emission distribution.) The derivative relative to z_{ij} is then given by

$$\frac{\partial L}{z_{ij}} = -\left[m_{ij} - n_{ij} - a_{ij} \sum_{j'} \left(m_{ij'} - n_{ij'} \right) \right].$$

Further manipulations can yield an update equation that eliminates the auxiliary variables. However, in our implementation we'll work with the auxiliary variables directly, so this is sufficient for our needs.

3.6.2 Deriving the update equations for normal distributions

This is about as far as we can go without specifying the model further, so let's now consider the case where the emission distributions are normal and each state is governed by different parameters. If f_i is the probability density function for state i with mean μ_i and variance σ_i^2, then its derivative relative to μ_i is

$$\begin{aligned}\frac{\partial f_i(y)}{\partial \mu_i} &= \frac{1}{\sqrt{2\pi\sigma_i^2}} e^{-\frac{(y-\mu_i)^2}{2\sigma_i^2}} \frac{y-\mu_i}{\sigma_i^2} \\ &= f_i(y)\frac{y-\mu_i}{\sigma_i^2},\end{aligned}$$

and the derivative relative to σ_i^2 is

$$\begin{aligned}\frac{\partial f_i(y)}{\partial \sigma_i^2} &= \frac{1}{\sqrt{2\pi}} \cdot -\frac{1}{2}\left(\sigma_i^2\right)^{-\frac{3}{2}} e^{-\frac{(y-\mu_i)^2}{2\sigma_i^2}} + \frac{1}{\sqrt{2\pi}}\left(\sigma_i^2\right)^{-\frac{1}{2}} e^{-\frac{(y-\mu_i)^2}{2\sigma_i^2}} \cdot -\frac{(y-\mu_i)^2}{2} \cdot -\left(\sigma_i^2\right)^{-2} \\ &= \frac{f_i(y)}{2}\left[\left(-\sigma_i^2\right)^{-1} + (y-\mu_i)^2\left(\sigma_i^2\right)^{-2}\right].\end{aligned}$$

Because the variance is non-negative, we define

$$\sigma_i^2 = e^{z_i}$$

and perform gradient descent on the auxiliary variable z_i. The new derivative is then easily calculated as

$$\frac{\partial f_i(y)}{\partial z_i} = \frac{\partial f_i(y)}{\partial \sigma_i^2}\frac{\partial \sigma_i^2}{\partial z_i}$$

using the chain rule.

The final step is to put all these pieces together by substituting the above expressions into the derivatives of the free and clamped log-likelihoods and taking their difference. For μ_i, this is

$$\frac{\partial L}{\partial \mu_i} = -\left[\sum_t \left(m_i(t) - n_i(t)\right)\left(\frac{y_t - \mu_i}{\sigma_i^2}\right)\right].$$

3.6.3 Labeling data with a misspecified model

We're finally ready to see discriminative training in action! To illustrate the differences between maximum likelihood and conditional maximum likelihood, we'll examine a case of model misspecification. Specifically we'll fit normal distributions to data where the emissions of one state follow a gamma distribution. The gamma distribution is highly flexible, so its parameter `a` can dramatically impact the shape of its density curve. However, for many values of `a` the gamma distribution is roughly normal with a right skew. Thus, the goal of this example is to understand the impact of this skew on the parameter estimates and accuracy of state inference for each training method.

Let's start by creating the components of an HMM with two states and plotting the density functions of their emission distributions.

In:
```
t_dists = {1: {1: 0.95, 2: 0.05},
           2: {1: 0.1, 2: 0.9}}
e_dists = {1: stats.norm(loc=-2.5, scale=25**0.5),  # Scale is std dev
           2: stats.gamma(a=1.5, scale=16**0.5)}
start_dist = {1: 0.5, 2: 0.5}

xs = np.linspace(-25, 25, 250)
ys1 = e_dists[1].pdf(xs)
ys2 = e_dists[2].pdf(xs)

plt.plot(xs, ys1, label='1')
plt.plot(xs, ys2, label='2')
plt.ylabel('Density')
plt.legend(**legend_kwargs);
```

Out:

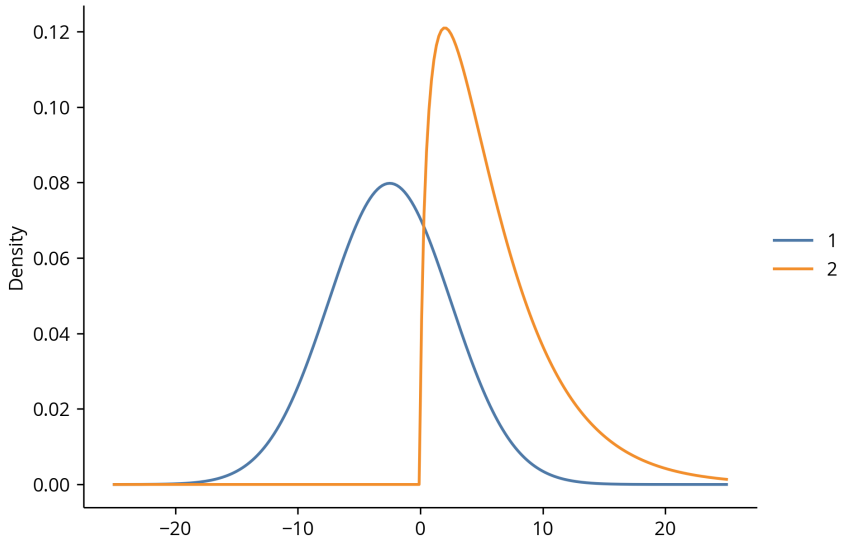

Though the densities are clearly distinct, they do have a non-trivial overlap.

Let's generate some data and look at a single example to get a sense of the kinds of sequences this

HMM produces.

```
In: model = HMM(t_dists=t_dists, e_dists=e_dists, start_dist=start_dist)

    data = [model.simulate(200, random_state=i) for i in range(10)]
    data = [list(zip(*example)) for example in data]

    xs, ys = data[0]
    lines = {}
    for state in t_dists:
        lines[state] = [x == state for x in xs]

    fig, axs = plt.subplots(2, 1, sharex=True)
    axs[0].plot(ys)
    for state, line in sorted(lines.items()):
        axs[1].plot(line, label=state)
    axs[1].set_xlabel('Time step')
    axs[0].set_ylabel('Emission')
    axs[1].set_ylabel('Label')
    axs[1].legend(**legend_kwargs);
```

Out:

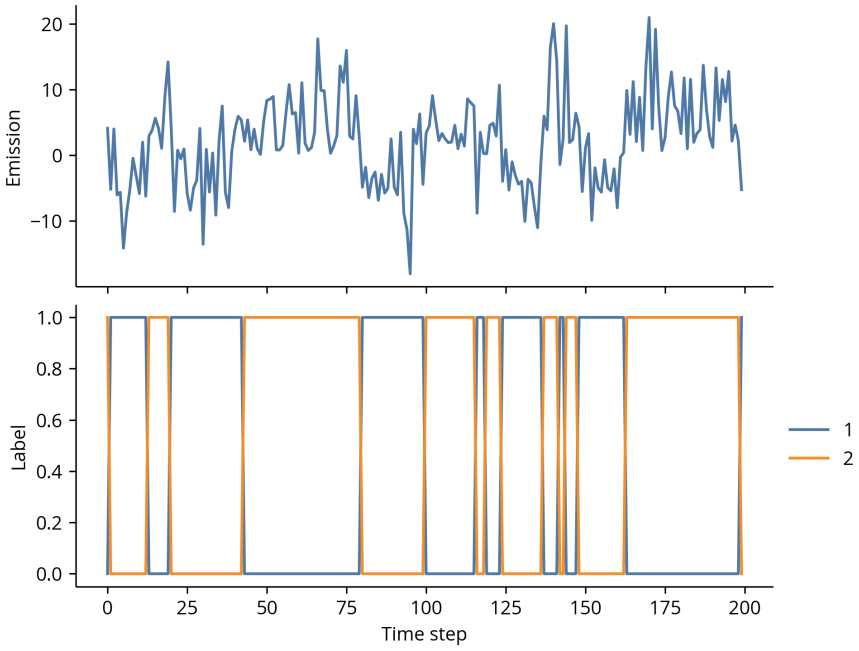

It's apparent there are alternating high and low intervals. However, as a result of the overlap between the emission distributions, the boundaries are not always clearcut.

We'll now fit models with normally distributed emissions using both training methods, beginning with maximum likelihood. The following code implements the same maximum likelihood estimators derived in previous sections. However, because this is an advanced example, we'll do the calculations with NumPy arrays. Because NumPy arrays vectorize operations, this is generally more efficient and cleaner than iterating over each state-emission pair in a for loop.

In:
```
xstack = np.stack([xs for xs, ys in data])
ystack = np.stack([ys for xs, ys in data])

# Make estimated transition distributions
t_dists_ML = {}
for state1, t_dist in t_dists.items():
    t_dist_ML = {}
    x1 = (xstack[:, :-1] == state1)
    x1_sum = x1.sum()
    for state2 in t_dist:
        x2 = (xstack[:, 1:] == state2)
        x12_sum = (x1 & x2).sum()
        t_dist_ML[state2] = x12_sum / x1_sum
    t_dists_ML[state1] = t_dist_ML
print('ML ESTIMATED T_DISTS')
for state, t_dist_ML in t_dists_ML.items():
    print(f'{state}: {t_dist_ML}')
print()

# Make estimated emission distributions
e_params_ML = {}
for state in e_dists:
    xs = xstack.ravel() == state
    ys = ystack.ravel()[xs]
    loc = ys.mean()
    scale = ys.var()
    e_params_ML[state] = {'mu': loc, 'sigma2': scale}
print('ML ESTIMATED E_PARAMS')
for state, e_param_ML in e_params_ML.items():
    print(f'{state}: {e_param_ML}')
print()

# Make estimated start distribution
start_dist_ML = {}
for state in start_dist:
    start_dist_ML[state] = (xstack[:, 0] == state).sum() / xstack.shape[0]
print('ML ESTIMATED START_DIST')
print(start_dist_ML)
```

Out:
```
ML ESTIMATED T_DISTS
1: {1: 0.9470684039087948, 2: 0.052931596091205214}
2: {1: 0.08923884514435695, 2: 0.910761154855643}

ML ESTIMATED E_PARAMS
1: {'mu': -2.708260094140367, 'sigma2': 24.878695602046125}
2: {'mu': 5.875899028606219, 'sigma2': 22.49724725215567}

ML ESTIMATED START_DIST
```

```
{1: 0.3, 2: 0.7}
```

Let's now tackle conditional maximum likelihood training, and after we'll compare the two. Because the implementation is somewhat lengthy, it's included as the function `fit_CML` in the accompanying `utils` module. We only have to supply all the pieces. First, each parameter requires an initial estimate. While it's best practice to inject some randomness into these initial values and choose the best result after several runs, for simplicity, we'll use the ML estimates directly. Because `t_dists` and `start_dist` will always take the form of a nested dictionary and dictionary, respectively, `fit_CML` accepts these objects as is. The emission distributions are more complex, however, because we need to provide the 1) parameter names and their initial estimates, 2) the emission probability or density functions, 3) their derivatives relative to each parameter, 4) functions which transform any constrained parameters to their auxiliary variables, and 5) corresponding functions which reverse the transformation. Accordingly, each of these is supplied as a separate argument in the form of simple or nested dictionaries.

Fortunately, the ML parameter estimates are already in the proper form, so we can go directly to the emission density functions. The hardest part here is choosing our parameters and their names since they must be consistent throughout all functions we define. We'll use the names `mu` and `sigma2`, so they correspond to the equations derived in the previous section. These parameters, however, differ slightly from those used by the SciPy statistics module, so we'll create a thin wrapper around its implementation of the normal density function.

```
In: def norm_pdf(y, mu, sigma2):
        return stats.norm.pdf(y, loc=mu, scale=sigma2**0.5)
```

After defining our new density function, we simply map the states to it in a dictionary.

```
In: e_funcs = {1: norm_pdf,
               2: norm_pdf}
```

The derivatives require more explanation. As we saw before, the derivative of the conditional log-likelihood function involves a sum over a function that includes n_i and m_i. However, the terms involving those variables are the same for any emission distribution whose parameters are not shared between states, so it would be redundant to include them every time. Instead, in `fit_CML` the derivative relative to the auxiliary variable z takes the form

$$\frac{\partial L}{\partial z} = -\left[\sum_t \left(m_i(t) - n_i(t)\right) f(y_t)\right],$$

and we only provide the function f as the "derivative." Note the derivative is relative to an unconstrained auxiliary variable. For unconstrained parameters, there is no difference, but the derivatives of constrained parameters must be relative to their unconstrained counterparts. These functions must also accept the emissions y as their first argument and the parameters by their names as subsequent arguments. Finally, because all parameters and their auxiliary variables are passed into the derivative functions, they must allow a variable number of keyword arguments with the `**kwargs` syntax to "catch" any unused arguments.

Though these requirements may sound complex, in practice they are fairly intuitive. For example, our derivatives are direct translations of the expressions we found earlier.

```
In: def norm_prime_mu(y, mu, sigma2, **kwargs):
        return (y - mu) / sigma2


    def norm_prime_sigma2(y, mu, sigma2, **kwargs):
        term1 = - 1 / sigma2
        term2 = (y - mu) ** 2 / sigma2 ** 2
        return 0.5 * (term1 + term2) * sigma2
```

These functions are then mapped to their corresponding state and parameter combination using a nested dictionary.

```
In: e_primes = {1: {'mu': norm_prime_mu, 'sigma2': norm_prime_sigma2},
                2: {'mu': norm_prime_mu, 'sigma2': norm_prime_sigma2}}
```

The two sets of variable transformation functions are defined and structured similarly. The auxiliary variables are named with the convention that the corresponding auxiliary variable for parameter `param` is called `param_aux`.

```
In: def mu2aux(mu, **kwargs):
        return mu


    def aux2mu(mu_aux, **kwargs):
        return mu_aux


    def sigma22aux(sigma2, **kwargs):
        return log(sigma2)


    def aux2sigma2(sigma2_aux, **kwargs):
        return exp(sigma2_aux)


    e_param2aux = {1: {'mu': mu2aux, 'sigma2': sigma22aux},
                   2: {'mu': mu2aux, 'sigma2': sigma22aux}}
    e_aux2param = {1: {'mu': aux2mu, 'sigma2': aux2sigma2},
                   2: {'mu': aux2mu, 'sigma2': aux2sigma2}}
```

We're finally ready to fit our model to the data! All we have to do now is pass our arguments into `fit_CML`. There are a few more optional parameters, but their meanings should be clear from the previous discussion.

```
In: params = fit_CML(data,
                     t_dists=t_dists_ML,
                     e_params=e_params_ML, e_funcs=e_funcs, e_primes=e_primes,
                     e_param2aux=e_param2aux, e_aux2param=e_aux2param,
                     start_dist=start_dist_ML, eta=0.3, maxiter=500, verbose=False)
    t_dists_CML, e_params_CML, start_dist_CML = params
```

```
print('CML ESTIMATED T_DISTS')
for state, t_dist_CML in t_dists_CML.items():
    print(f'{state}: {t_dist_CML}')
print()
print('CML ESTIMATED E_PARAMS')
for state, e_param_CML in e_params_CML.items():
    print(f'{state}: {e_param_CML}')
print()
print('CML ESTIMATED START_DIST')
print(start_dist_CML)
```

Out:
```
CML ESTIMATED T_DISTS
1: {1: 0.9485741440805543, 2: 0.05142585591944567}
2: {1: 0.09604341135218855, 2: 0.9039565886478114}

CML ESTIMATED E_PARAMS
1: {'mu': -2.7344728682990804, 'sigma2': 23.630241342073358}
2: {'mu': 5.990857687710255, 'sigma2': 12.528992301575078}

CML ESTIMATED START_DIST
{1: 0.014065968700277301, 2: 0.9859340312997227}
```

The parameter estimates don't appear to have changed too drastically, but let's plot the density functions with the true parameters against the two estimated densities to get a better sense of how they differ.

In:
```
fig, axs = plt.subplots(2, 1, figsize=(6.4, 7.2))
xs = np.linspace(-25, 25, 250)

ys1 = e_dists[1].pdf(xs)
ys2 = e_dists[2].pdf(xs)
for ax in axs:
    ax.plot(xs, ys1, label='true state 1')
    ax.plot(xs, ys2, label='true state 2')
    ax.set_ylabel('Density')

ys1 = stats.norm.pdf(xs,
                     loc=e_params_ML[1]['mu'],
                     scale=e_params_ML[1]['sigma2']**0.5)
ys2 = stats.norm.pdf(xs,
                     loc=e_params_ML[2]['mu'],
                     scale=e_params_ML[2]['sigma2']**0.5)
axs[0].plot(xs, ys1, label='ML state 1')
axs[0].plot(xs, ys2, label='ML state 2')
axs[0].legend(**legend_kwargs)

ys1 = stats.norm.pdf(xs,
                     loc=e_params_CML[1]['mu'],
```

```
                        scale=e_params_CML[1]['sigma2']**0.5)
ys2 = stats.norm.pdf(xs,
                        loc=e_params_CML[2]['mu'],
                        scale=e_params_CML[2]['sigma2']**0.5)
axs[1].plot(xs, ys1, label='CML state 1')
axs[1].plot(xs, ys2, label='CML state 2')
axs[1].legend(**legend_kwargs);
```

Out:

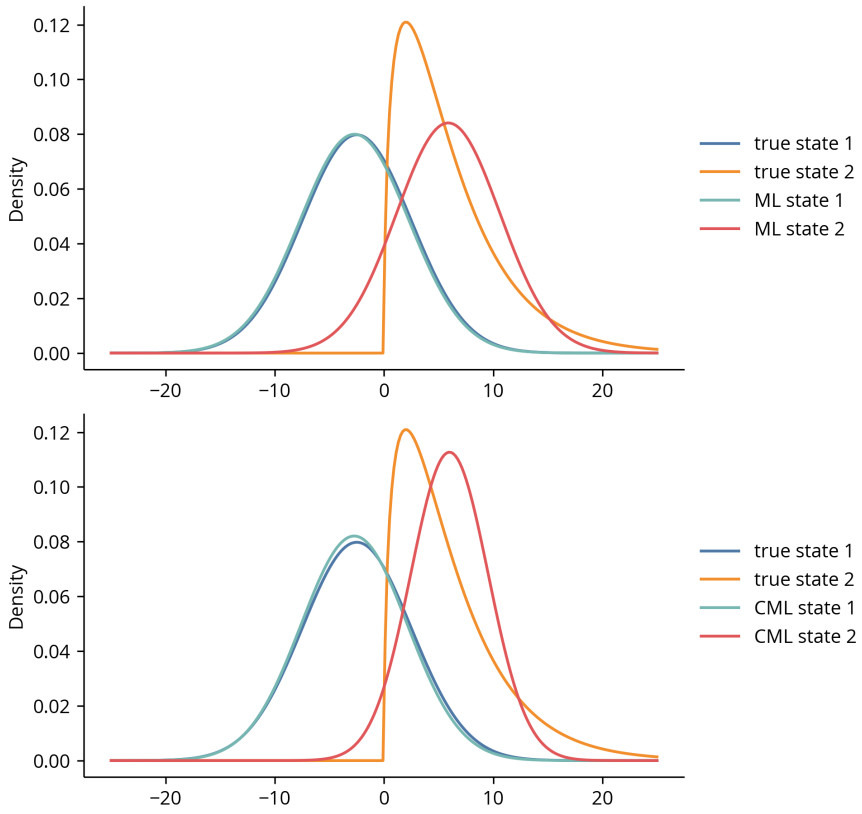

The change is most obvious for state 2 whose curve is much more peaked. However, even the state 1 curve has shifted slightly as well. These differences can be easily understood in terms of the objective functions. Maximum likelihood estimation chooses parameters that best describe the data, so the distribution is wider to account for the skew. In contrast, conditional maximum likelihood estimation chooses parameters that maximize prediction accuracy, so the distribution is narrower to better capture the decision boundary.

However, has all this work actually yielded an improvement in the accuracy of state inference? We can check by using the estimated models to calculate the probability of each state at each time step. Since these probabilities range continuously from zero to one, they are in a sense soft labels. Accuracy calculations, though, require hard state assignments. There are any number of methods to convert the probabilities into states, but the easiest is using a threshold of 0.5. This is a natural choice because we have no reason to favor one state over the other, but in general the threshold should reflect the costs of incorrect assignments for each state. For example, credit card companies err on the side of caution when alerting customers to potential fraud because the cost of confirming a valid transaction is much smaller than refunding a fraudulent one.

In:
```
e_dists_ML = {}
for state, e_param_ML in e_params_ML.items():
    e_dists_ML[state] = stats.norm(loc=e_param_ML['mu'],
                                   scale=e_param_ML['sigma2']**0.5)
e_dists_CML = {}
for state, e_param_CML in e_params_CML.items():
    e_dists_CML[state] = stats.norm(loc=e_param_CML['mu'],
                                    scale=e_param_CML['sigma2']**0.5)

model_ML = HMM(t_dists=t_dists_ML,
               e_dists=e_dists_ML,
               start_dist=start_dist_ML)
model_CML = HMM(t_dists=t_dists_CML,
                e_dists=e_dists_CML,
                start_dist=start_dist_CML)

xstack_ML = []
xstack_CML = []
for example in data:
    _, ys = example
    fbs_ML = model_ML.forward_backward(ys)
    fbs_CML = model_CML.forward_backward(ys)

    xstack_ML.append(fbs_ML[1])
    xstack_CML.append(fbs_CML[1])
xstack_ML = np.stack(xstack_ML)
xstack_CML = np.stack(xstack_CML)

threshold = 0.5
accuracy_ML = ((xstack_ML >= threshold) == (xstack == 1)).sum()
accuracy_CML = ((xstack_CML >= threshold) == (xstack == 1)).sum()
print('ML accuracy:', accuracy_ML / xstack.size)
print('CML accuracy:', accuracy_CML / xstack.size)
```

Out:
```
ML accuracy: 0.948
CML accuracy: 0.947
```

The CML model actually has a slight decrease in accuracy. However, we're not seeing the full picture by using a single threshold, and we should instead measure the models' responses as the threshold is varied continuously over the full range of the data. A common implementation of this idea is the *receiver operating characteristic* (ROC) curve which plots the true positive rate against the false positive rate at varying thresholds. It essentially measures the trade-off between the increases in true and false positives as the threshold is decreased. Thus, the curve of a model with good separation between classes should rise steeply and rapidly level off.

Let's plot the ROC curves for the two models.

In:
```
fpr_ML, tpr_ML, _ = roc_curve((xstack == 1).ravel(), xstack_ML.ravel())
fpr_CML, tpr_CML, _ = roc_curve((xstack == 1).ravel(), xstack_CML.ravel())

fig, ax = plt.subplots()
ax.plot(fpr_ML, tpr_ML, label='ML')
ax.plot(fpr_CML, tpr_CML, label='CML')
ax.set_xlabel('False positive rate')
ax.set_ylabel('True positive rate')
ax.legend(**legend_kwargs)

idx_ML = fpr_ML <= 0.1
idx_CML = fpr_CML <= 0.1
axins = ax.inset_axes([0.25, 0.1, 0.7, 0.5])
axins.plot(fpr_ML[idx_ML], tpr_ML[idx_ML], label='ML')
axins.plot(fpr_CML[idx_CML], tpr_CML[idx_CML], label='CML')
axins.set_xticklabels([])
axins.set_yticklabels([])
ax.indicate_inset_zoom(axins, edgecolor='black');
```

Out:

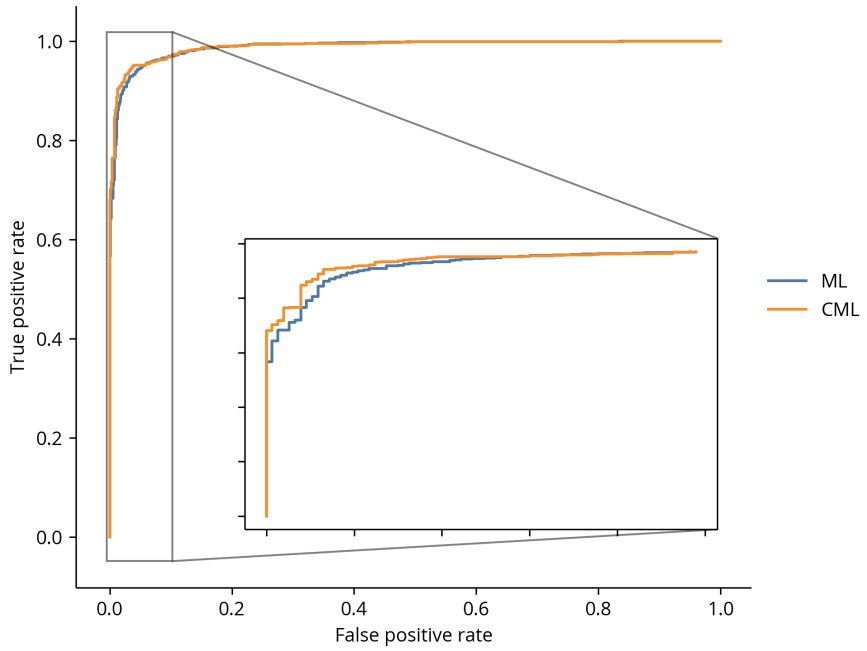

A small effect but an effect nonetheless! Because in this case the ML model was already close to the true model, the improvement in the discriminatively trained model was fairly marginal. However, the greater the mismatch between the data and a model, the greater the effect on state inference, so for real data the difference between the two approaches can be substantial.

3.7 Conclusion

We have at last reached the end of the training tutorial! It's been quite a tour through several fundamental concepts in statistics and machine learning. While many of these ideas seem complex, as shown throughout this tutorial, they can often be implemented in only a few dozen lines of code.

The previous examples have covered some of the most widely used distributions in statistics, but we've only scratched the surface of what is possible with probabilistic modeling. Fortunately, once the theoretical heavy lifting is out of the way, supporting a new distribution is often a relatively straightforward task of writing and solving a set of equations. Hopefully, then, these examples will inspire you to derive and implement your own MLEs and EM or gradient update equations if the need arises. Good luck!

References

1. Pierigè, F., Serafini, S., Rossi, L. & Magnani, M. Cell-based drug delivery. *Advanced Drug Delivery Reviews* **60,** 286–295 (Jan. 2008).
2. Kanias, T. & Acker, J. P. Biopreservation of red blood cells — the struggle with hemoglobin oxidation. *FEBS Journal* **277,** 343–356 (Nov. 2009).
3. Voet, D., Voet, J. G. & Pratt, C. W. *Fundamentals of biochemistry life at the molecular level 4E* (John Wiley & Sons, Chichester, England, July 2015).
4. Karush, F. Heterogeneity of the Binding Sites of Bovine Serum Albumin. *Journal of the American Chemical Society* **72,** 2705–2713 (June 1950).
5. Vrhovski, B. & Weiss, A. S. Biochemistry of tropoelastin. *European Journal of Biochemistry* **258,** 1–18 (Nov. 1998).
6. Alberts, B. *Molecular Biology of the Cell* 6th ed. (Garland Publishing, New York, NY, Nov. 2014).
7. Plaxco, K. W. & Gross, M. The importance of being unfolded. *Nature* **386,** 657–659 (Apr. 1997).
8. Wright, P. E. & Dyson, H. Intrinsically unstructured proteins: re-assessing the protein structure-function paradigm. *Journal of Molecular Biology* **293,** 321–331 (Oct. 1999).
9. Dunker, A. K. & Obradovic, Z. The protein trinity — linking function and disorder. *Nature Biotechnology* **19,** 805–806 (Sept. 2001).
10. Dunker, A. K., Obradovic, Z., Romero, P. & Garner, E. C. Intrinsic Protein Disorder in Complete Genomes. *Genome Informatics* **11,** 161–171 (Jan. 2000).
11. Ward, J., Sodhi, J., McGuffin, L., Buxton, B. & Jones, D. Prediction and Functional Analysis of Native Disorder in Proteins from the Three Kingdoms of Life. *Journal of Molecular Biology* **337,** 635–645 (Mar. 2004).
12. Finley, D., Chen, X. & Walters, K. J. Gates, Channels, and Switches: Elements of the Proteasome Machine. *Trends in Biochemical Sciences* **41,** 77–93 (Jan. 2016).
13. Bard, J. A. *et al.* Structure and Function of the 26S Proteasome. *Annual Review of Biochemistry* **87,** 697–724 (June 2018).
14. Bard, J. A., Bashore, C., Dong, K. C. & Martin, A. The 26S Proteasome Utilizes a Kinetic Gateway to Prioritize Substrate Degradation. *Cell* **177,** 286–298.e15 (Apr. 2019).
15. Uversky, V. N., Gillespie, J. R. & Fink, A. L. Why are "natively unfolded" proteins unstructured under physiologic conditions? *Proteins: Structure, Function, and Genetics* **41,** 415–427 (2000).
16. Mao, A. H., Crick, S. L., Vitalis, A., Chicoine, C. L. & Pappu, R. V. Net charge per residue modulates conformational ensembles of intrinsically disordered proteins. *Proceedings of the National Academy of Sciences* **107,** 8183–8188 (Apr. 2010).
17. Van der Lee, R. *et al.* Classification of Intrinsically Disordered Regions and Proteins. *Chemical Reviews* **114,** 6589–6631 (Apr. 2014).

18. Das, R. K., Ruff, K. M. & Pappu, R. V. Relating sequence encoded information to form and function of intrinsically disordered proteins. *Current Opinion in Structural Biology* **32,** 102–112 (June 2015).
19. Tompa, P., Davey, N. E., Gibson, T. J. & Babu, M. M. A Million Peptide Motifs for the Molecular Biologist. *Molecular Cell* **55,** 161–169 (July 2014).
20. Dunker, A. K., Cortese, M. S., Romero, P., Iakoucheva, L. M. & Uversky, V. N. Flexible nets. The roles of intrinsic disorder in protein interaction networks. *FEBS Journal* **272,** 5129–5148 (Oct. 2005).
21. Buljan, M. *et al.* Tissue-Specific Splicing of Disordered Segments that Embed Binding Motifs Rewires Protein Interaction Networks. *Molecular Cell* **46,** 871–883 (June 2012).
22. Wright, P. E. & Dyson, H. J. Intrinsically disordered proteins in cellular signalling and regulation. *Nature Reviews Molecular Cell Biology* **16,** 18–29 (Dec. 2014).
23. Liu, J. *et al.* Intrinsic Disorder in Transcription Factors. *Biochemistry* **45,** 6873–6888 (May 2006).
24. Ma, J. & Ptashne, M. A new class of yeast transcriptional activators. *Cell* **51,** 113–119 (Oct. 1987).
25. Sigler, P. B. Acid blobs and negative noodles. *Nature* **333,** 210–212 (May 1988).
26. Gerber, H.-P. *et al.* Transcriptional Activation Modulated by Homopolymeric Glutamine and Proline Stretches. *Science* **263,** 808–811 (Feb. 1994).
27. Arnold, C. D. *et al.* A high-throughput method to identify trans-activation domains within transcription factor sequences. *The EMBO Journal* **37** (July 2018).
28. Ravarani, C. N. *et al.* High-throughput discovery of functional disordered regions: investigation of transactivation domains. *Molecular Systems Biology* **14** (May 2018).
29. Staller, M. V. *et al.* A High-Throughput Mutational Scan of an Intrinsically Disordered Acidic Transcriptional Activation Domain. *Cell Systems* **6,** 444–455.e6 (Apr. 2018).
30. Erijman, A. *et al.* A High-Throughput Screen for Transcription Activation Domains Reveals Their Sequence Features and Permits Prediction by Deep Learning. *Molecular Cell* **78,** 890–902.e6 (June 2020).
31. Sanborn, A. L. *et al.* Simple biochemical features underlie transcriptional activation domain diversity and dynamic, fuzzy binding to Mediator. *eLife* **10** (Apr. 2021).
32. Necci, M. *et al.* Critical assessment of protein intrinsic disorder prediction. *Nature Methods* **18,** 472–481 (Apr. 2021).
33. Camacho, C. *et al.* BLAST+: architecture and applications. *BMC Bioinformatics* **10** (Dec. 2009).
34. Eddy, S. R. *A New Generation Of Homology Search Tools Based On Probabilistic Inference* in *Genome Informatics 2009* (Imperial College Press, Oct. 2009).
35. Mistry, J. *et al.* Pfam: The protein families database in 2021. *Nucleic Acids Research* **49,** D412–d419 (Oct. 2020).
36. Jumper, J. *et al.* Highly accurate protein structure prediction with AlphaFold. *Nature* **596,** 583–589 (July 2021).
37. Daughdrill, G. W., Narayanaswami, P., Gilmore, S. H., Belczyk, A. & Brown, C. J. Dynamic Behavior of an Intrinsically Unstructured Linker Domain Is Conserved in the Face of Negligible Amino Acid Sequence Conservation. *Journal of Molecular Evolution* **65,** 277–288 (Aug. 2007).
38. Moesa, H. A., Wakabayashi, S., Nakai, K. & Patil, A. Chemical composition is maintained in poorly conserved intrinsically disordered regions and suggests a means for their classification. *Molecular BioSystems* **8,** 3262 (2012).

39. Zarin, T., Tsai, C. N., Ba, A. N. N. & Moses, A. M. Selection maintains signaling function of a highly diverged intrinsically disordered region. *Proceedings of the National Academy of Sciences* **114** (Feb. 2017).
40. Beh, L. Y., Colwell, L. J. & Francis, N. J. A core subunit of Polycomb repressive complex 1 is broadly conserved in function but not primary sequence. *Proceedings of the National Academy of Sciences* **109** (Apr. 2012).
41. Yang, H. *et al.* Re-annotation of eight *Drosophila* genomes. *Life Science Alliance* **1,** e201800156 (Dec. 2018).
42. Miller, D. E., Staber, C., Zeitlinger, J. & Hawley, R. S. Highly Contiguous Genome Assemblies of 15 *Drosophila* Species Generated Using Nanopore Sequencing. *G3 Genes|Genomes|Genetics* **8,** 3131–3141 (Oct. 2018).
43. Kim, B. Y. *et al.* Highly contiguous assemblies of 101 drosophilid genomes. *eLife* **10** (July 2021).
44. Gramates, L. S. *et al.* FlyBase: a guided tour of highlighted features. *Genetics* **220** (Mar. 2022).
45. Hardison, R. C. Comparative Genomics. *PLoS Biology* **1,** e58 (Nov. 2003).
46. Fleischmann, R. D. *et al.* Whole-Genome Random Sequencing and Assembly of *Haemophilus influenzae* Rd. *Science* **269,** 496–512 (July 1995).
47. Goffeau, A. *et al.* Life with 6000 Genes. *Science* **274,** 546–567 (Oct. 1996).
48. Consortium, T. C. e. S. Genome Sequence of the Nematode *C. elegans*: A Platform for Investigating Biology. *Science* **282,** 2012–2018 (Dec. 1998).
49. Tatusov, R. L., Koonin, E. V. & Lipman, D. J. A Genomic Perspective on Protein Families. *Science* **278,** 631–637 (Oct. 1997).
50. Fitch, W. M. Distinguishing homologous from analogous proteins. *Systematic Zoology* **31,** 99–113 (June 1970).
51. Ohno, S. *Evolution by Gene Duplication* (Springer Berlin Heidelberg, 1970).
52. Nowak, M. A., Boerlijst, M. C., Cooke, J. & Smith, J. M. Evolution of genetic redundancy. *Nature* **388,** 167–171 (July 1997).
53. Altenhoff, A. M., Studer, R. A., Robinson-Rechavi, M. & Dessimoz, C. Resolving the Ortholog Conjecture: Orthologs Tend to Be Weakly, but Significantly, More Similar in Function than Paralogs. *PLoS Computational Biology* **8,** e1002514 (May 2012).
54. Pegueroles, C., Laurie, S. & Albà, M. M. Accelerated Evolution after Gene Duplication: A Time-Dependent Process Affecting Just One Copy. *Molecular Biology and Evolution* **30,** 1830–1842 (Apr. 2013).
55. Soria, P. S., McGary, K. L. & Rokas, A. Functional Divergence for Every Paralog. *Molecular Biology and Evolution* **31,** 984–992 (Jan. 2014).
56. Remm, M., Storm, C. E. & Sonnhammer, E. L. Automatic clustering of orthologs and inparalogs from pairwise species comparisons. *Journal of Molecular Biology* **314,** 1041–1052 (Dec. 2001).
57. Jensen, L. J. *et al.* eggNOG: automated construction and annotation of orthologous groups of genes. *Nucleic Acids Research* **36,** D250–D254 (Dec. 2007).
58. Train, C.-M., Glover, N. M., Gonnet, G. H., Altenhoff, A. M. & Dessimoz, C. Orthologous Matrix (OMA) algorithm 2.0: more robust to asymmetric evolutionary rates and more scalable hierarchical orthologous group inference. *Bioinformatics* **33,** i75–i82 (July 2017).
59. Linard, B., Thompson, J. D., Poch, O. & Lecompte, O. OrthoInspector: comprehensive orthology analysis and visual exploration. *BMC Bioinformatics* **12** (Jan. 2011).
60. Cosentino, S. & Iwasaki, W. SonicParanoid: fast, accurate and easy orthology inference. *Bioinformatics* **35,** 149–151 (July 2018).

61. Enright, A. J. An efficient algorithm for large-scale detection of protein families. *Nucleic Acids Research* **30,** 1575–1584 (Apr. 2002).
62. Li, L., Stoeckert, C. J. & Roos, D. S. OrthoMCL: Identification of Ortholog Groups for Eukaryotic Genomes. *Genome Research* **13,** 2178–2189 (Sept. 2003).
63. Emms, D. M. & Kelly, S. OrthoFinder: solving fundamental biases in whole genome comparisons dramatically improves orthogroup inference accuracy. *Genome Biology* **16** (Aug. 2015).
64. Thomas, G. W. C. *et al.* Gene content evolution in the arthropods. *Genome Biology* **21** (Jan. 2020).
65. Feng, S. *et al.* Dense sampling of bird diversity increases power of comparative genomics. en. *Nature* **587,** 252–257 (Nov. 2020).
66. Rhie, A. *et al.* Towards complete and error-free genome assemblies of all vertebrate species. *Nature* **592,** 737–746 (Apr. 2021).
67. Frankish, A. *et al.* Comparison of GENCODE and RefSeq gene annotation and the impact of reference geneset on variant effect prediction. *BMC Genomics* **16** (June 2015).
68. Dunne, M. P. & Kelly, S. OMGene: mutual improvement of gene models through optimisation of evolutionary conservation. *BMC Genomics* **19** (Apr. 2018).
69. Consortium, D. 1. G. Evolution of genes and genomes on the *Drosophila* phylogeny. *Nature* **450,** 203–218 (Nov. 2007).
70. Wiegmann, B. M. *et al.* Episodic radiations in the fly tree of life. *Proceedings of the National Academy of Sciences* **108,** 5690–5695 (Mar. 2011).
71. Obbard, D. J. *et al.* Estimating Divergence Dates and Substitution Rates in the Drosophila Phylogeny. *Molecular Biology and Evolution* **29,** 3459–3473 (Aug. 2012).
72. Thibaud-Nissen, F., Souvorov, A., Murphy, T., DiCuccio, M. & Kitts, P. in. Chap. Eukaryotic Genome Annotation Pipeline (National Center for Biotechnology Information, 2013).
73. Dobzhansky, T. *Drosophila miranda*, a new species. *Genetics* **20,** 377–391 (July 1935).
74. Katoh, K. & Standley, D. M. MAFFT Multiple Sequence Alignment Software Version 7: Improvements in Performance and Usability. *Molecular Biology and Evolution* **30,** 772–780 (Jan. 2013).
75. Katoh, K. & Standley, D. M. A simple method to control over-alignment in the MAFFT multiple sequence alignment program. *Bioinformatics* **32,** 1933–1942 (Feb. 2016).
76. Castresana, J. Selection of Conserved Blocks from Multiple Alignments for Their Use in Phylogenetic Analysis. *Molecular Biology and Evolution* **17,** 540–552 (Apr. 2000).
77. Capella-Gutierrez, S., Silla-Martinez, J. M. & Gabaldon, T. trimAl: a tool for automated alignment trimming in large-scale phylogenetic analyses. *Bioinformatics* **25,** 1972–1973 (June 2009).
78. Felsenstein, J. & Churchill, G. A. A Hidden Markov Model approach to variation among sites in rate of evolution. *Molecular Biology and Evolution* **13,** 93–104 (Jan. 1996).
79. Siepel, A. & Haussler, D. Combining Phylogenetic and Hidden Markov Models in Biosequence Analysis. *Journal of Computational Biology* **11,** 413–428 (Mar. 2004).
80. Lage, J.-L. D. *et al.* A phylogeny of Drosophilidae using the *Amyrel* gene: questioning the *Drosophila melanogaster* species group boundaries. *Journal of Zoological Systematics and Evolutionary Research* **45,** 47–63 (Feb. 2007).
81. Dunne, M. P. & Kelly, S. OrthoFiller: utilising data from multiple species to improve the completeness of genome annotations. *BMC Genomics* **18** (May 2017).
82. Sievers, F. & Higgins, D. G. Clustal Omega for making accurate alignments of many protein sequences. *Protein Science* **27,** 135–145 (Oct. 2017).

83. Edgar, R. C. MUSCLE: multiple sequence alignment with high accuracy and high throughput. *Nucleic Acids Research* **32,** 1792–1797 (Mar. 2004).
84. Notredame, C., Higgins, D. G. & Heringa, J. T-coffee: a novel method for fast and accurate multiple sequence alignment. *Journal of Molecular Biology* **302,** 205–217 (Sept. 2000).
85. Nord, A., Hornbeck, P., Carey, K. & Wheeler, T. *Splice-Aware Multiple Sequence Alignment of Protein Isoforms* in *Proceedings of the 2018 ACM International Conference on Bioinformatics, Computational Biology, and Health Informatics* (ACM, Aug. 2018).
86. Le, S. Q. & Gascuel, O. An Improved General Amino Acid Replacement Matrix. *Molecular Biology and Evolution* **25,** 1307–1320 (Apr. 2008).
87. Nevers, Y. *et al.* The Quest for Orthologs orthology benchmark service in 2022. *Nucleic Acids Research* **50,** W623–W632 (May 2022).
88. Kaduk, M. & Sonnhammer, E. Improved orthology inference with Hieranoid 2. *Bioinformatics,* btw774 (Jan. 2017).
89. Altenhoff, A. M. *et al.* OMA standalone: orthology inference among public and custom genomes and transcriptomes. *Genome Research* **29,** 1152–1163 (June 2019).
90. Emms, D. M. & Kelly, S. OrthoFinder: phylogenetic orthology inference for comparative genomics. *Genome Biology* **20** (Nov. 2019).
91. Linard, B. *et al.* OrthoInspector 2.0: Software and database updates. *Bioinformatics* **31,** 447–448 (Oct. 2014).
92. Zdobnov, E. M. *et al.* OrthoDB in 2020: evolutionary and functional annotations of orthologs. *Nucleic Acids Research* **49,** D389–D393 (Nov. 2020).
93. Galperin, M. Y. *et al.* COG database update: focus on microbial diversity, model organisms, and widespread pathogens. *Nucleic Acids Research* **49,** D274–D281 (Nov. 2020).
94. Herrero, J. *et al.* Ensembl comparative genomics resources. *Database* **2016,** bav096 (2016).
95. Huerta-Cepas, J. *et al.* eggNOG 5.0: a hierarchical, functionally and phylogenetically annotated orthology resource based on 5090 organisms and 2502 viruses. *Nucleic Acids Research* **47,** D309–D314 (Nov. 2018).
96. Altenhoff, A. M. *et al.* OMA orthology in 2021: website overhaul, conserved isoforms, ancestral gene order and more. *Nucleic Acids Research* **49,** D373–D379 (Nov. 2020).
97. Nevers, Y. *et al.* OrthoInspector 3.0: open portal for comparative genomics. *Nucleic Acids Research* **47,** D411–D418 (Oct. 2018).
98. Chen, F. OrthoMCL-DB: querying a comprehensive multi-species collection of ortholog groups. *Nucleic Acids Research* **34,** D363–D368 (Jan. 2006).
99. Altschul, S. F., Carroll, R. J. & Lipman, D. J. Weights for data related by a tree. *Journal of Molecular Biology* **207,** 647–653 (June 1989).
100. Felsenstein, J. Evolutionary trees from DNA sequences: A maximum likelihood approach. *Journal of Molecular Evolution* **17,** 368–376 (Nov. 1981).
101. Krogh, A. & Riis, S. K. Hidden Neural Networks. *Neural Computation* **11,** 541–563 (Feb. 1999).
102. Yang, Z. Maximum likelihood phylogenetic estimation from DNA sequences with variable rates over sites: Approximate methods. *Journal of Molecular Evolution* **39,** 306–314 (Sept. 1994).
103. Nguyen, L.-T., Schmidt, H. A., von Haeseler, A. & Minh, B. Q. IQ-TREE: A Fast and Effective Stochastic Algorithm for Estimating Maximum Likelihood Phylogenies. *Molecular Biology and Evolution* **32,** 268–274 (Nov. 2014).
104. Hunter, J. D. Matplotlib: A 2D Graphics Environment. *Computing in Science & Engineering* **9,** 90–95 (2007).
105. Harris, C. R. *et al.* Array programming with NumPy. *Nature* **585,** 357–362 (Sept. 2020).

106. McKinney, W. *Data Structures for Statistical Computing in Python* in *Proceedings of the Python in Science Conference* (SciPy, 2010).
107. Virtanen, P. *et al.* SciPy 1.0: fundamental algorithms for scientific computing in Python. *Nature Methods* **17,** 261–272 (Feb. 2020).
108. Zhou, H.-X. Intrinsic disorder: signaling via highly specific but short-lived association. *Trends in Biochemical Sciences* **37,** 43–48 (Feb. 2012).
109. Piovesan, D. *et al.* MobiDB: intrinsically disordered proteins in 2021. *Nucleic Acids Research* **49,** D361–D367 (Nov. 2020).
110. Piovesan, D. *et al.* MobiDB: 10 years of intrinsically disordered proteins. *Nucleic Acids Research* **51,** D438–D444 (Nov. 2022).
111. Banani, S. F., Lee, H. O., Hyman, A. A. & Rosen, M. K. Biomolecular condensates: organizers of cellular biochemistry. *Nature Reviews Molecular Cell Biology* **18,** 285–298 (Feb. 2017).
112. Fuxreiter, M., Tompa, P. & Simon, I. Local structural disorder imparts plasticity on linear motifs. *Bioinformatics* **23,** 950–956 (Mar. 2007).
113. Davey, N. E. *et al.* Attributes of short linear motifs. *Mol. BioSyst.* **8,** 268–281 (2012).
114. Ba, A. N. N. *et al.* Proteome-Wide Discovery of Evolutionary Conserved Sequences in Disordered Regions. *Science Signaling* **5** (Mar. 2012).
115. Roey, K. V., Gibson, T. J. & Davey, N. E. Motif switches: decision-making in cell regulation. *Current Opinion in Structural Biology* **22,** 378–385 (June 2012).
116. Tan, C. S. H., Jørgensen, C. & Linding, R. Roles of "junk phosphorylation" in modulating biomolecular association of phosphorylated proteins? *Cell Cycle* **9,** 1276–1280 (Apr. 2010).
117. Zarin, T. *et al.* Identifying molecular features that are associated with biological function of intrinsically disordered protein regions. *eLife* **10** (Feb. 2021).
118. Sillitoe, I. *et al.* CATH: increased structural coverage of functional space. *Nucleic Acids Research* **49,** D266–D273 (Nov. 2020).
119. Andreeva, A., Howorth, D., Chothia, C., Kulesha, E. & Murzin, A. G. SCOP2 prototype: a new approach to protein structure mining. *Nucleic Acids Research* **42,** D310–D314 (Nov. 2013).
120. Andreeva, A., Kulesha, E., Gough, J. & Murzin, A. G. The SCOP database in 2020: expanded classification of representative family and superfamily domains of known protein structures. *Nucleic Acids Research* **48,** D376–D382 (Nov. 2019).
121. Cornwell, W. & Nakagawa, S. Phylogenetic comparative methods. *Current Biology* **27,** R333–R336 (May 2017).
122. Wang, S., Ma, J. & Xu, J. AUCpreD: proteome-level protein disorder prediction by AUC-maximized deep convolutional neural fields. *Bioinformatics* **32,** i672–i679 (Aug. 2016).
123. Ho, L. S. T. & Ané, C. Asymptotic theory with hierarchical autocorrelation: Ornstein-Uhlenbeck tree models. *The Annals of Statistics* **41** (Apr. 2013).
124. Ho, L. S. T. & Ané, C. Intrinsic inference difficulties for trait evolution with Ornstein-Uhlenbeck models. *Methods in Ecology and Evolution* **5,** 1133–1146 (Nov. 2014).
125. Zarin, T. *et al.* Proteome-wide signatures of function in highly diverged intrinsically disordered regions. *eLife* **8** (July 2019).
126. Brown, C. J., Johnson, A. K. & Daughdrill, G. W. Comparing Models of Evolution for Ordered and Disordered Proteins. *Molecular Biology and Evolution* **27,** 609–621 (Nov. 2009).
127. Szalkowski, A. M. & Anisimova, M. Markov Models of Amino Acid Substitution to Study Proteins with Intrinsically Disordered Regions. *PLoS ONE* **6,** e20488 (May 2011).
128. Wang, J. *et al.* A Molecular Grammar Governing the Driving Forces for Phase Separation of Prion-like RNA Binding Proteins. *Cell* **174,** 688–699.e16 (July 2018).

129. Halfmann, R. *et al.* Opposing Effects of Glutamine and Asparagine Govern Prion Formation by Intrinsically Disordered Proteins. *Molecular Cell* **43,** 72–84 (July 2011).
130. Mohan, A. *et al.* Analysis of Molecular Recognition Features (MoRFs). *Journal of Molecular Biology* **362,** 1043–1059 (Oct. 2006).
131. Lu, A. X. *et al.* Discovering molecular features of intrinsically disordered regions by using evolution for contrastive learning. *PLOS Computational Biology* **18,** e1010238 (June 2022).
132. Crawford, F. W. & Suchard, M. A. Transition probabilities for general birth–death processes with applications in ecology, genetics, and evolution. *Journal of Mathematical Biology* **65,** 553–580 (Oct. 2011).
133. Flory, P. J. The Configuration of Real Polymer Chains. *The Journal of Chemical Physics* **17,** 303–310 (Mar. 1949).
134. Kohn, J. E. *et al.* Random-coil behavior and the dimensions of chemically unfolded proteins. *Proceedings of the National Academy of Sciences* **101,** 12491–12496 (Aug. 2004).
135. Kumar, M. *et al.* The Eukaryotic Linear Motif resource: 2022 release. *Nucleic Acids Research* **50,** D497–D508 (Oct. 2021).
136. Holehouse, A. S., Das, R. K., Ahad, J. N., Richardson, M. O. & Pappu, R. V. CIDER: Resources to Analyze Sequence-Ensemble Relationships of Intrinsically Disordered Proteins. *Biophysical Journal* **112,** 16–21 (Jan. 2017).
137. Kozlowski, L. P. IPC – Isoelectric Point Calculator. *Biology Direct* **11** (Oct. 2016).
138. Felsenstein, J. Maximum-likelihood estimation of evolutionary trees from continuous characters. *American Journal of Human Genetics* **25,** 471–492 (Sept. 1973).
139. Felsenstein, J. Phylogenies and the Comparative Method. *The American Naturalist* **125,** 1–15 (Jan. 1985).
140. Akaike, H. A new look at the statistical model identification. *IEEE Transactions on Automatic Control* **19,** 716–723 (Dec. 1974).
141. Butler, M. A. & King, A. A. Phylogenetic Comparative Analysis: A Modeling Approach for Adaptive Evolution. *The American Naturalist* **164,** 683–695 (Dec. 2004).
142. Ashburner, M. *et al.* Gene Ontology: tool for the unification of biology. *Nature Genetics* **25,** 25–29 (May 2000).
143. Consortium, G. O. The Gene Ontology resource: enriching a GOld mine. *Nucleic Acids Research* **49,** D325–D334 (Dec. 2020).
144. Pedregosa, F. *et al.* Scikit-learn: Machine Learning in Python. *Journal of Machine Learning Research* **12,** 2825–2830 (2011).
145. Durbin, R., Eddy, S. R., Krogh, A. & Mitchison, G. *Biological Sequence Analysis* (Cambridge University Press, Apr. 1998).

APPENDIX A

Supporting information for chapter 1

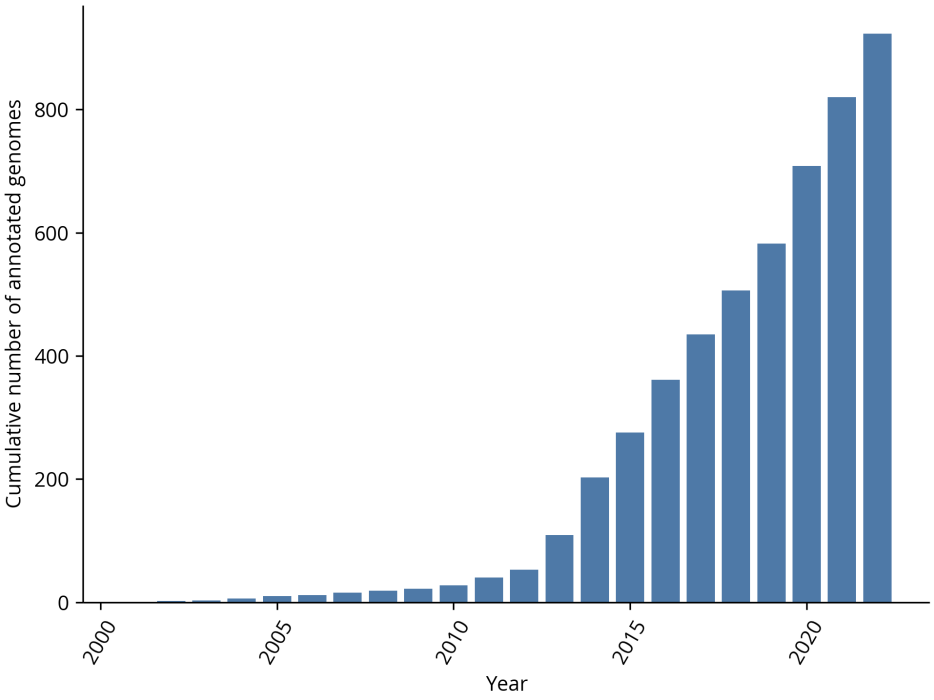

Figure A1. Cumulative number of different eukaryotic genomes annotated by NCBI.

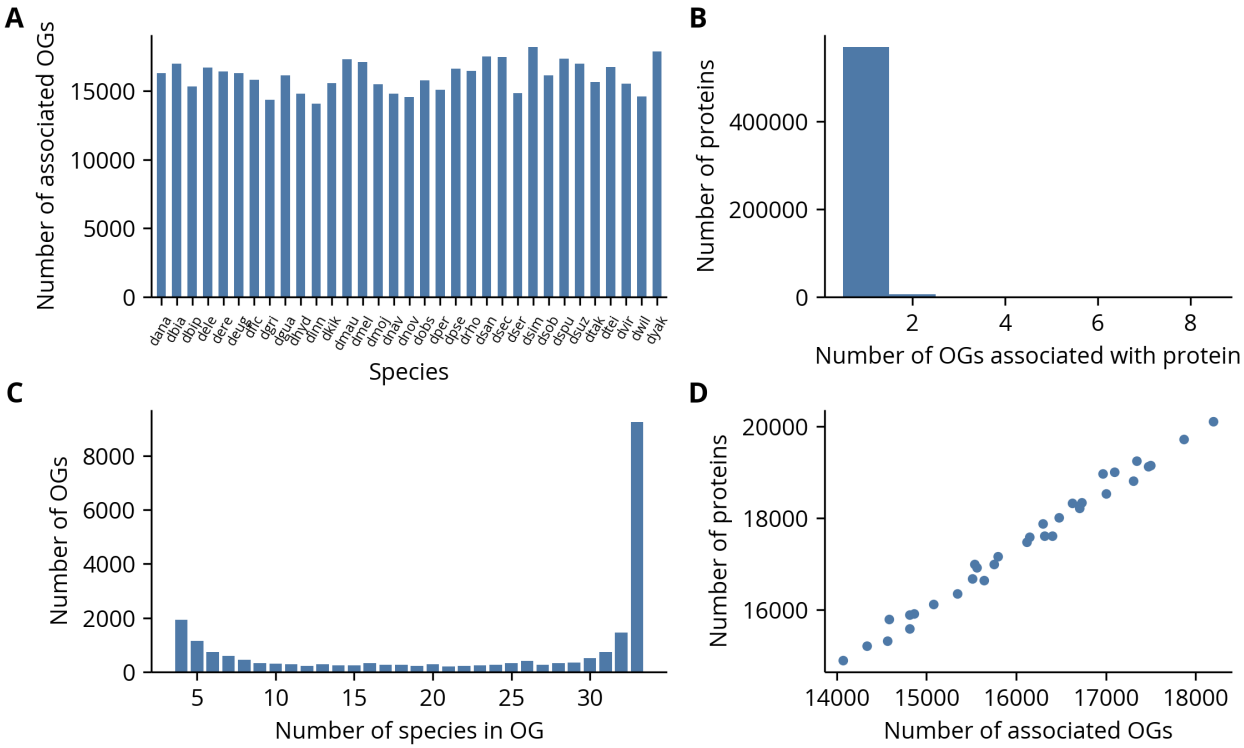

Figure A2. Statistics of orthologous groups. **(A)** Each species is equally represented in orthologous groups (OGs). **(B)** Nearly all proteins are associated with a single orthologous group. **(C)** A plurality of orthologous groups contain all species. **(D)** The number of orthologous groups associated with a species is strongly correlated with the number of unique annotated proteins, which suggests the annotation pipeline generally identifies conserved genes.

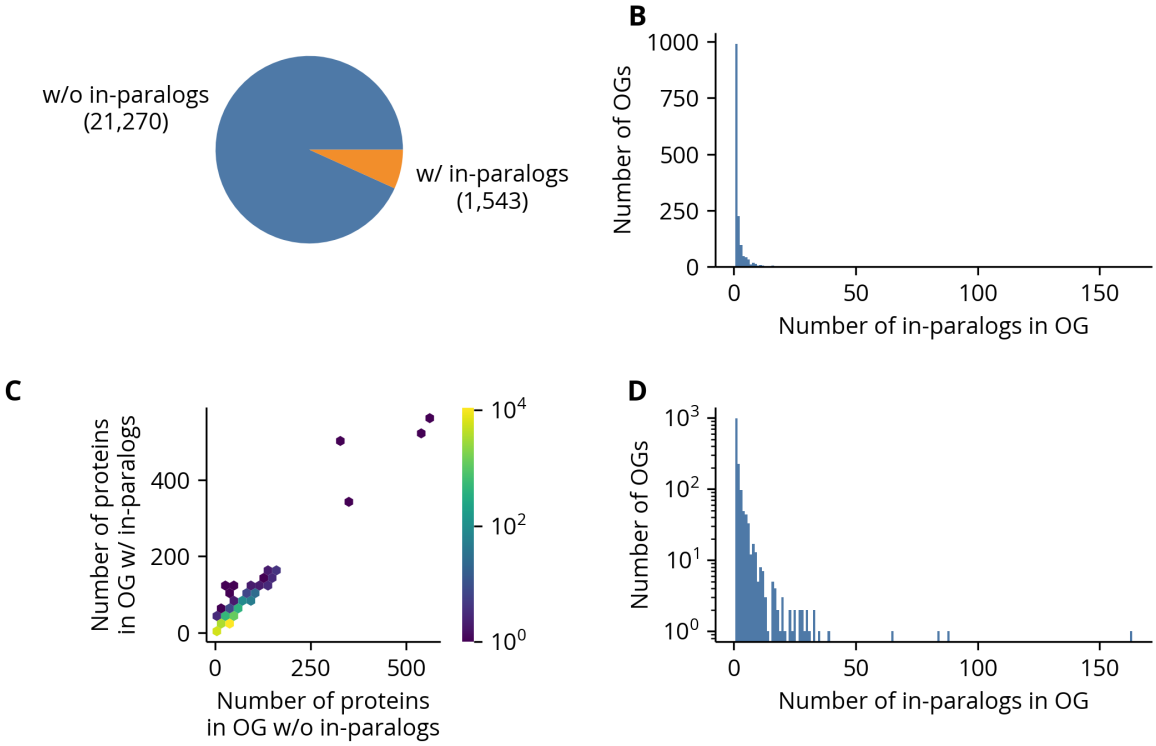

Figure A3. Addition of paralogs to orthologous groups. (A) Most orthologous groups (OGs) have no in-paralogs. **(B, D)** Of the groups with paralogs, most have fewer than five. **(C)** The in-paralogs are generally only a small fraction of the sequences in an orthologous group.

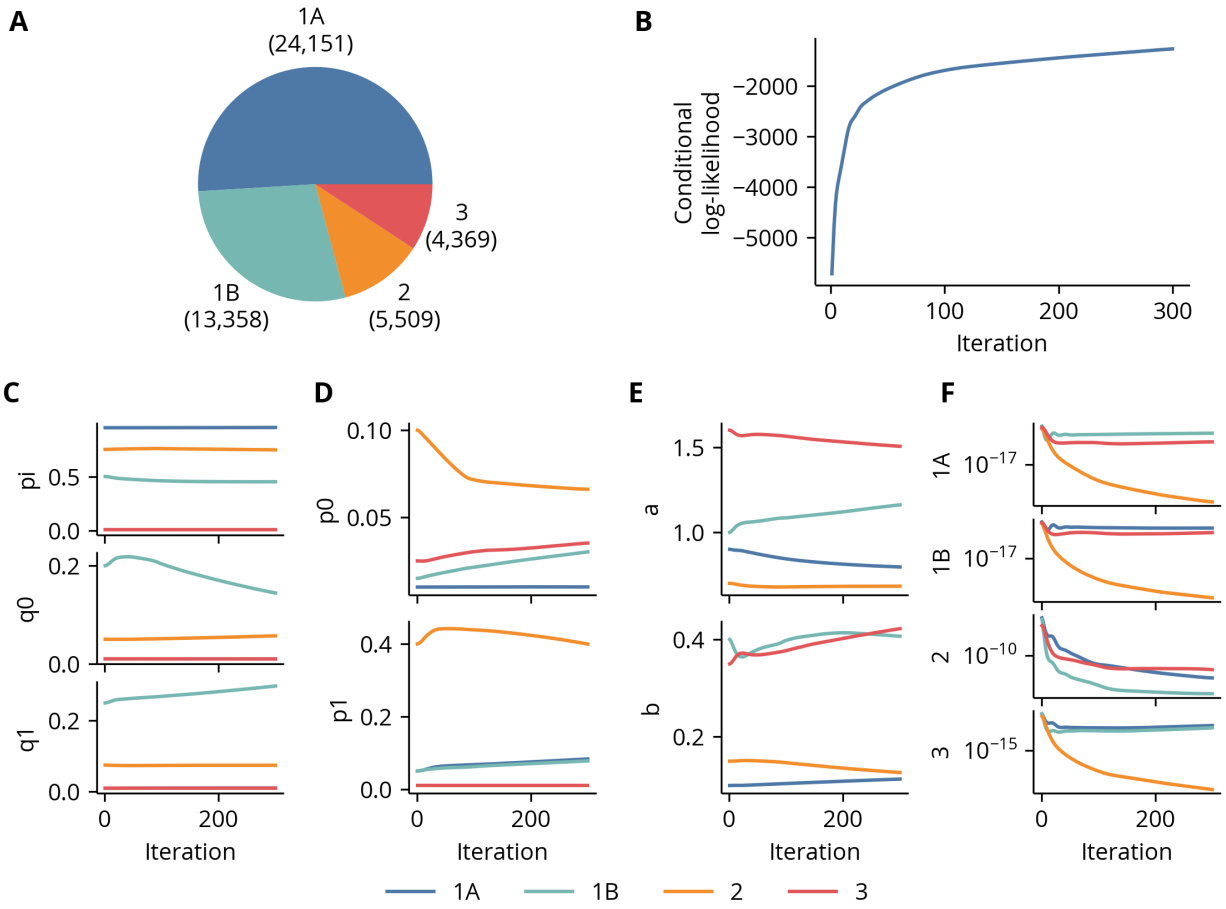

Figure A4. Insertion phylo-HMM data and training details. **(A)** Most columns in the training data were labeled as state 1A or 1B. **(B)** The model loss stabilized by the final training iteration. **(C-F)** The values of parameters in the phylogenetic process, the jump process, the pattern stickiness model, and the transition matrix, respectively, at each training iteration. The transition matrix plots are the transition rates to the state indicated on the vertical axis and given in log scale. Self transitions are excluded.

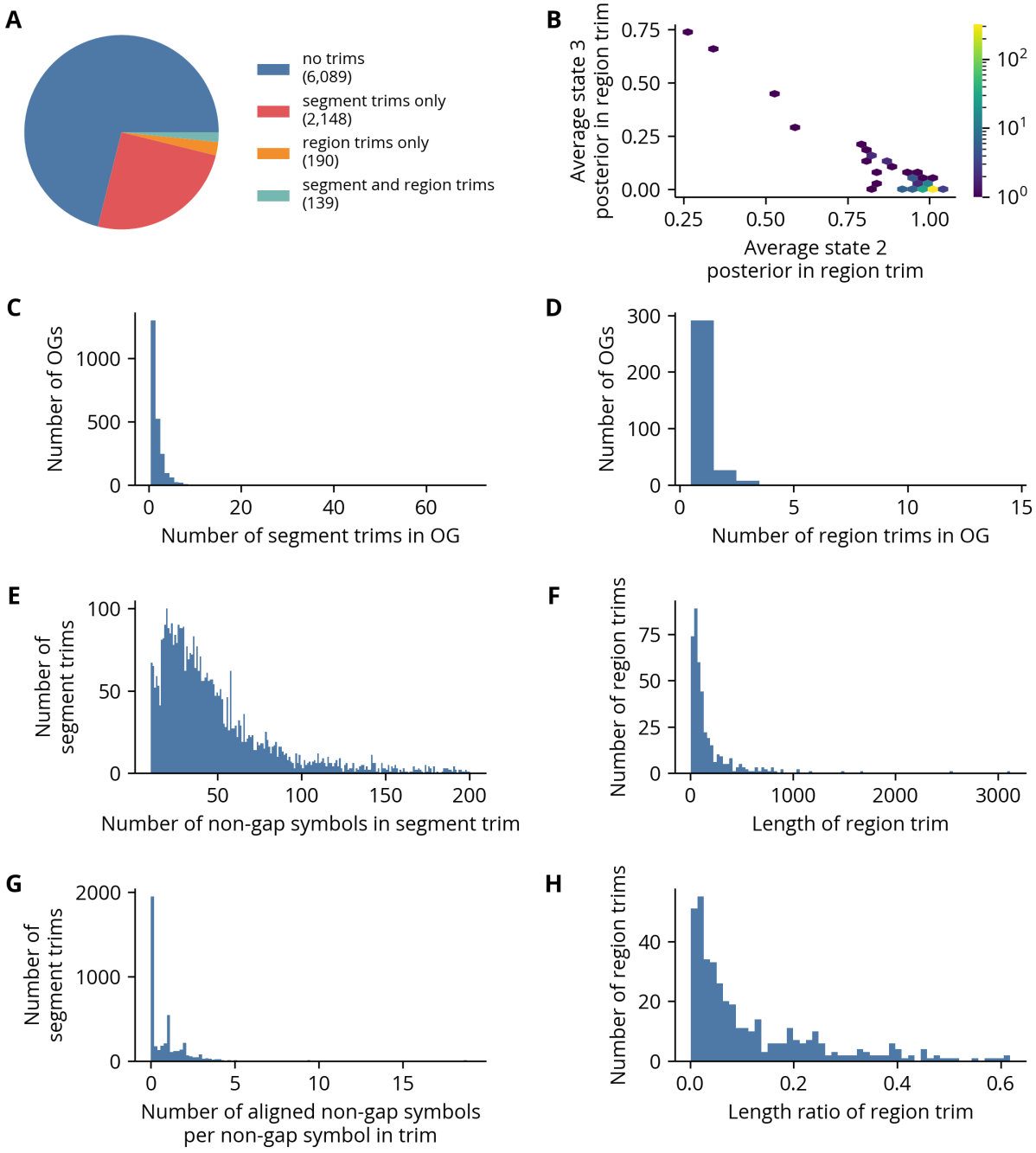

Figure A5. Insertion phylo-HMM trimming details. **(A)** Most alignments were not trimmed. Of the alignments with trims, most were trimmed only at the level of sequences. **(B)** Most trimmed regions were inferred primarily as state 2. **(C)** Most alignments with sequence trims have fewer than 10 segments removed. **(D)** Most alignments with region trims have fewer than five regions removed. **(E, G)** The number of non-gap symbols in sequence trims can vary considerably, but for nearly all sequence trims each non-gap symbol in the removed segment is aligned to fewer than five non-gap symbols on average. Only the lower 95% of the distribution of the number of non-gap symbols in the sequence trims is shown. **(F, H)** The length of region trims can also vary considerably, but generally each region trims accounts for fewer than 10% of the columns in the original alignment.

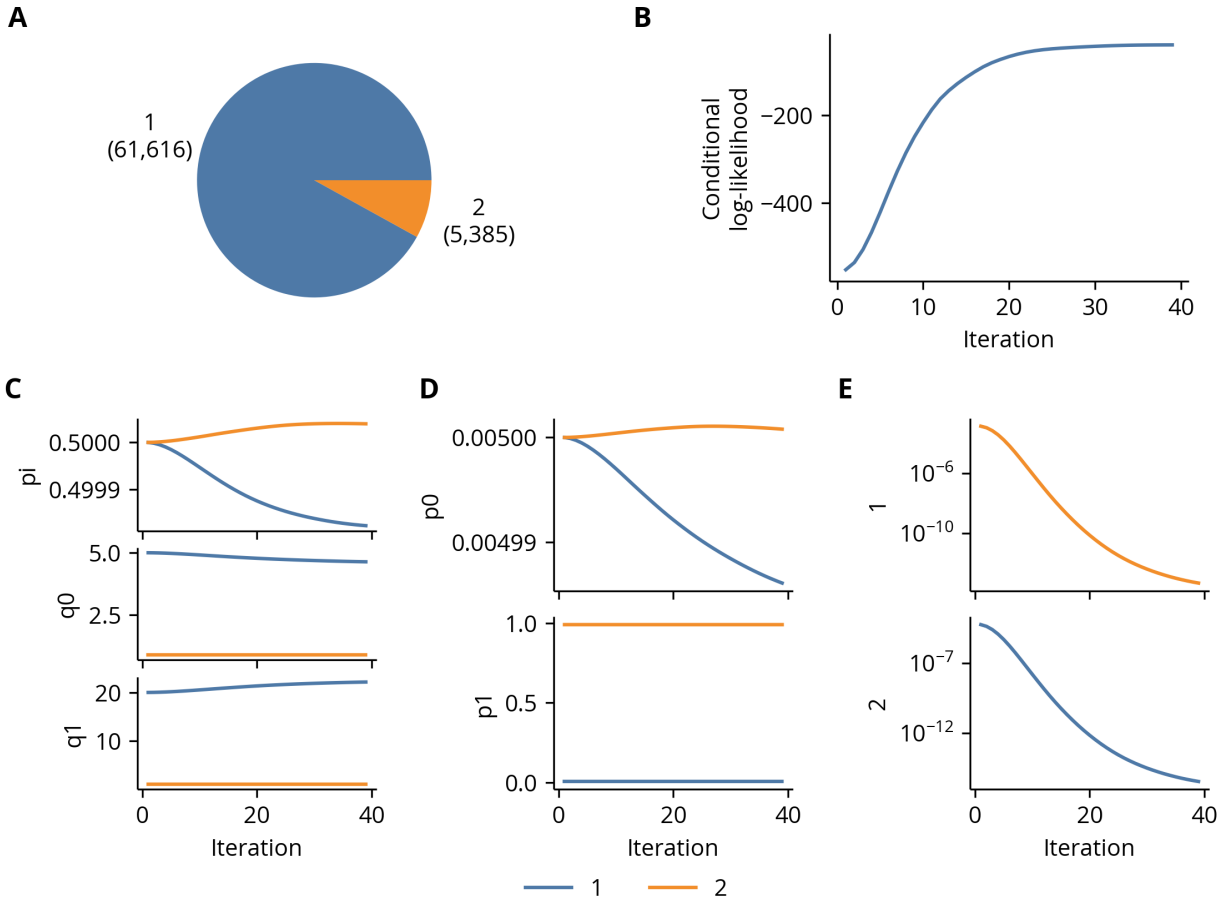

Figure A6. Missing phylo-HMM data and training details. (A) Most columns in the training data were labeled as state 1, which is referred to as the "not missing" state in the main text. **(B)** The model loss stabilized by the final training iteration. **(C-F)** The values of parameters in the phylogenetic process, the jump process, and the transition matrix, respectively, at each training iteration. The transition matrix plots are the transition rates to the state indicated on the vertical axis and given in log scale. Self transitions are excluded.

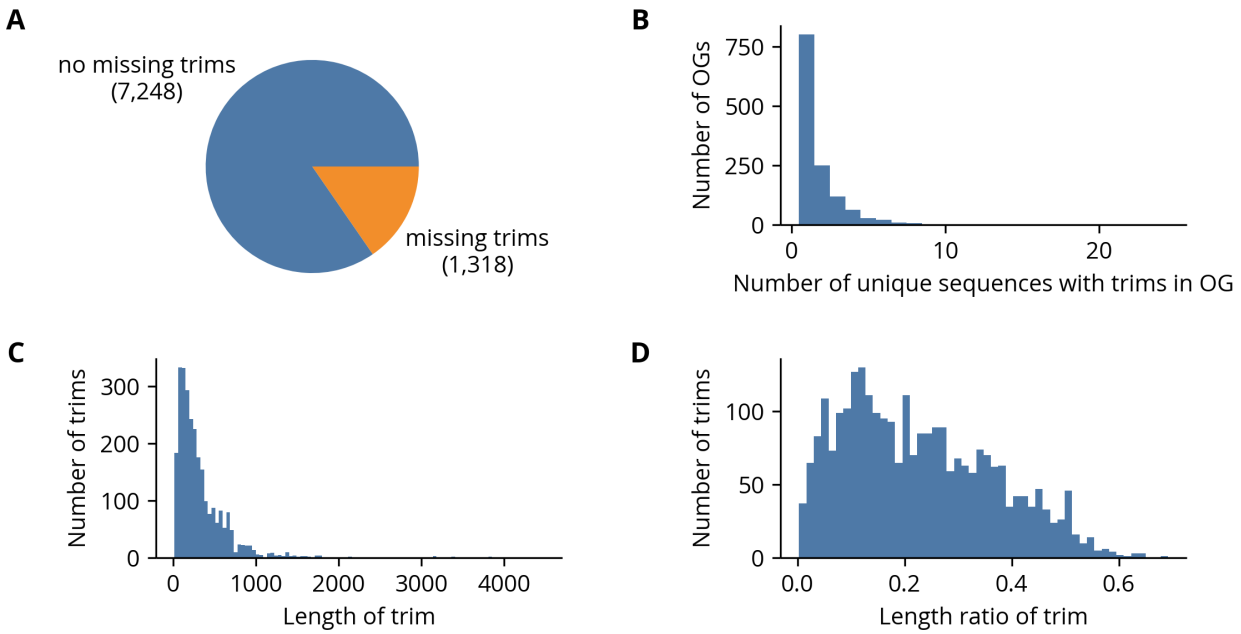

Figure A7. Missing phylo-HMM trimming details. **(A)** Most alignments have no sequences with "missing" segments. **(B)** Of the alignments with sequences trimmed of missing segments, a majority have only one trimmed sequence. **(C-D)** The length of missing segments can vary considerably, both in terms of the number of positions as well as its ratio to the number of columns in the alignment.

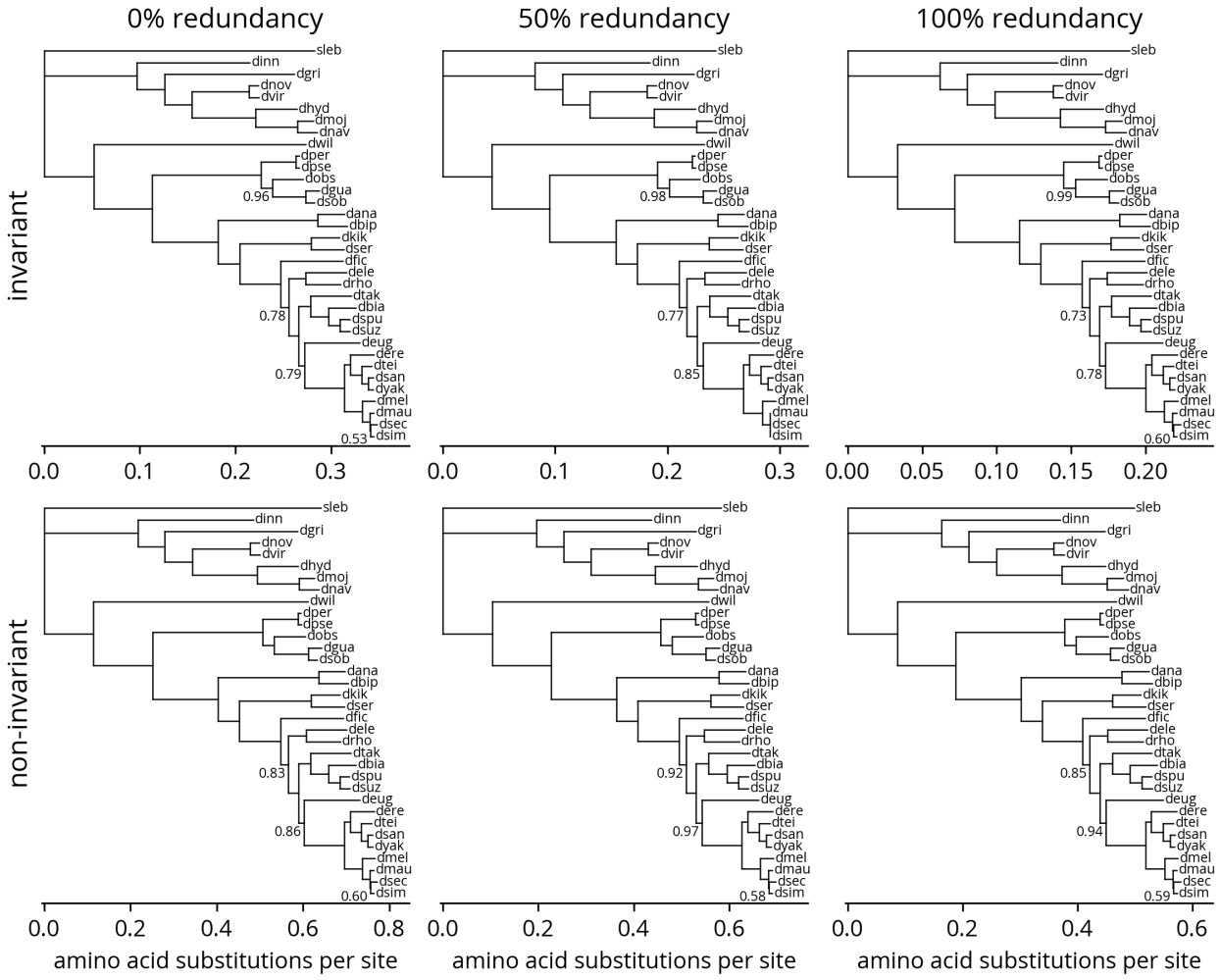

Figure A8. Phylogenetic trees fit to meta-alignments yielded by different sampling strategies under LG model.

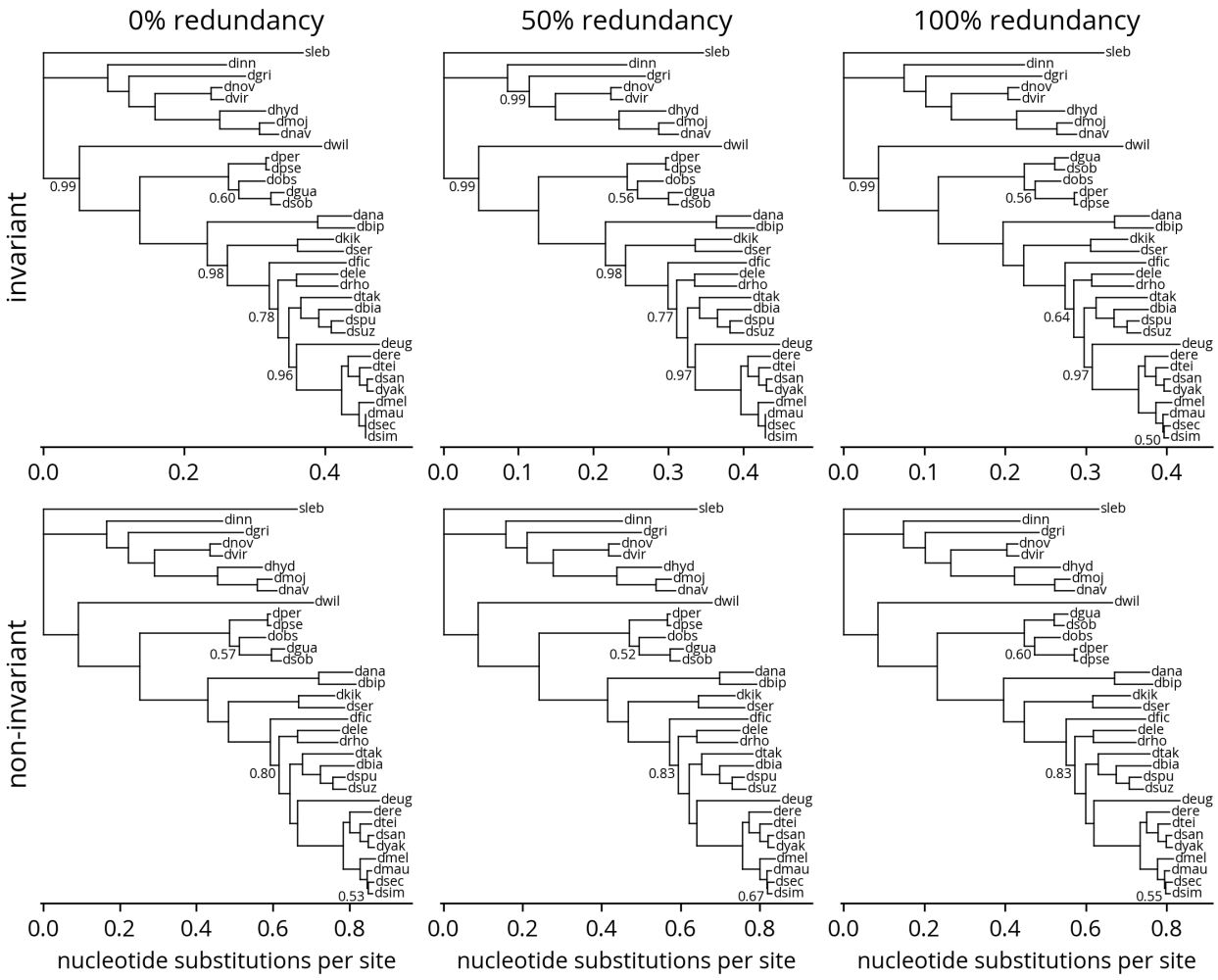

Figure A9. Phylogenetic trees fit by different sampling strategies under GTR model.

Table A1. Genome annotations.

Species	Species ID	Taxon ID	Version	Source
Drosophila ananassae	dana	7217	102	NCBI
Drosophila biarmipes	dbia	125945	102	NCBI
Drosophila bipectinata	dbip	42026	102	NCBI
Drosophila elegans	dele	30023	102	NCBI
Drosophila erecta	dere	7220	101	NCBI
Drosophila eugracilis	deug	29029	102	NCBI
Drosophila ficusphila	dfic	30025	102	NCBI
Drosophila grimshawi	dgri	7222	103	NCBI
Drosophila guanche	dgua	7266	100	NCBI
Drosophila hydei	dhyd	7224	101	NCBI
Drosophila innubila	dinn	198719	100	NCBI
Drosophila kikkawai	dkik	30033	102	NCBI
Drosophila mauritiana	dmau	7226	100	NCBI
Drosophila melanogaster	dmel	7227	FB2022_02	FlyBase
Drosophila mojavensis	dmoj	7230	102	NCBI
Drosophila navojoa	dnav	7232	101	NCBI
Drosophila novamexicana	dnov	47314	100	NCBI
Drosophila obscura	dobs	7282	101	NCBI
Drosophila persimilis	dper	7234	101	NCBI
Drosophila pseudoobscura	dpse	7237	104	NCBI
Drosophila rhopaloa	drho	1041015	102	NCBI
Drosophila santomea	dsan	129105	101	NCBI
Drosophila sechellia	dsec	7238	101	NCBI
Drosophila serrata	dser	7274	100	NCBI
Drosophila simulans	dsim	7240	103	NCBI
Drosophila subobscura	dsob	7241	100	NCBI
Drosophila subpulchrella	dspu	1486046	100	NCBI
Drosophila suzukii	dsuz	28584	102	NCBI
Drosophila takahashii	dtak	29030	102	NCBI
Drosophila teissieri	dtei	7243	100	NCBI
Drosophila virilis	dvir	7244	103	NCBI
Drosophila willistoni	dwil	7260	102	NCBI
Drosophila yakuba	dyak	7245	102	NCBI
Scaptodrosophila lebanonensis	sleb	7225	100	NCBI

Table A2. Phylogenetic diversity criteria.

Species IDs	Minimum number
dinn, dgri, dhyd	2
dnov, dvir	1
dmoj, dnav	1
dper, dpse	1
dgua, dsob	1
dana, dbip	1
dkik, dser	1
dele, drho	1
dtak, dbia	1
dspu, dsuz	1
dere, dtei	1
dsan, dyak	1
dmel	1
dmau, dsec, dsim	1

APPENDIX B

Supporting information for chapter 2

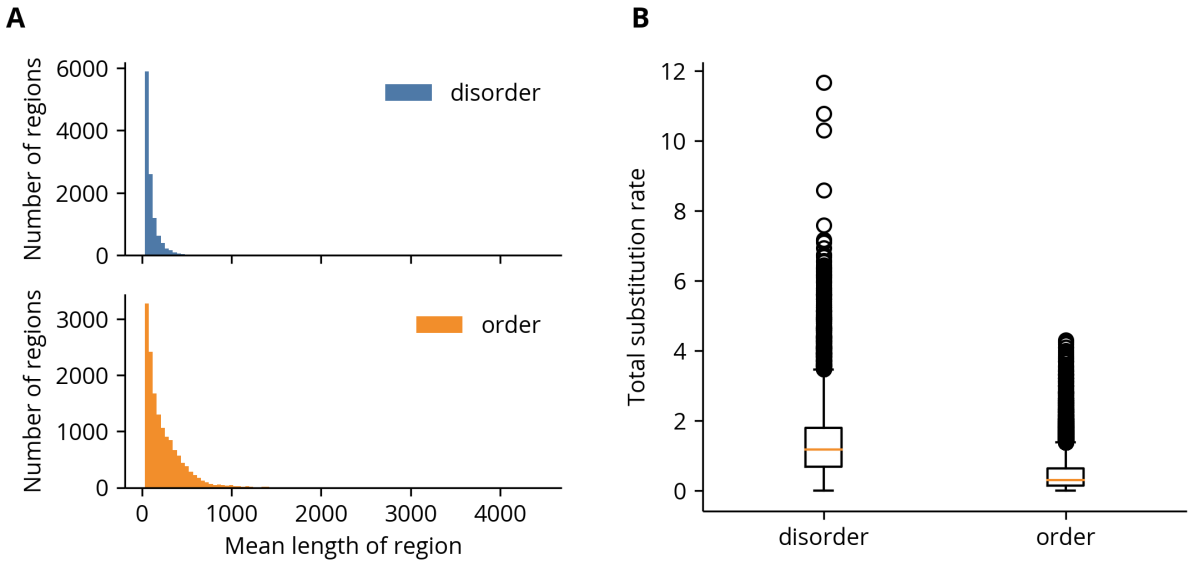

Figure B1. Summary statistics of disorder and order regions. (A) Distribution of mean lengths of regions. **(B)** Boxplot of the sums of the average amino acid and indel substitution rates in the disorder and order regions. The substitution rates are significantly greater in the disorder regions than in the order regions ($p < 1 \times 10^{-10}$, Mann-Whitney U test).

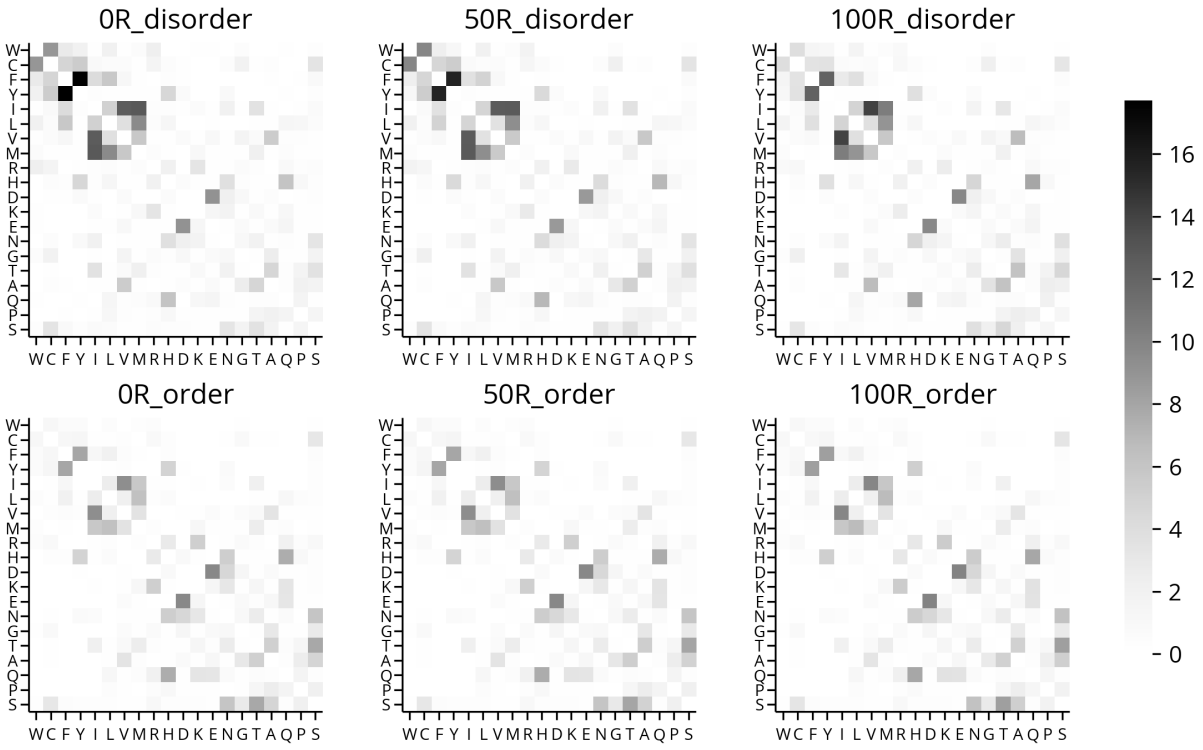

Figure B2. Exchangeability matrices fit to meta-alignments yielded by different sampling strategies. Each panel is a mean of the exchangeability coefficients fit to the meta-alignments yielded by a single sampling strategy ($n = 25$). The prefix and suffix in the title of each panel indicate the maximum gap fraction and region type of the columns in the meta-alignments. For example, the columns in the "50R_disorder" set of meta-alignments were fewer than 50% gaps and sampled from the disorder regions.

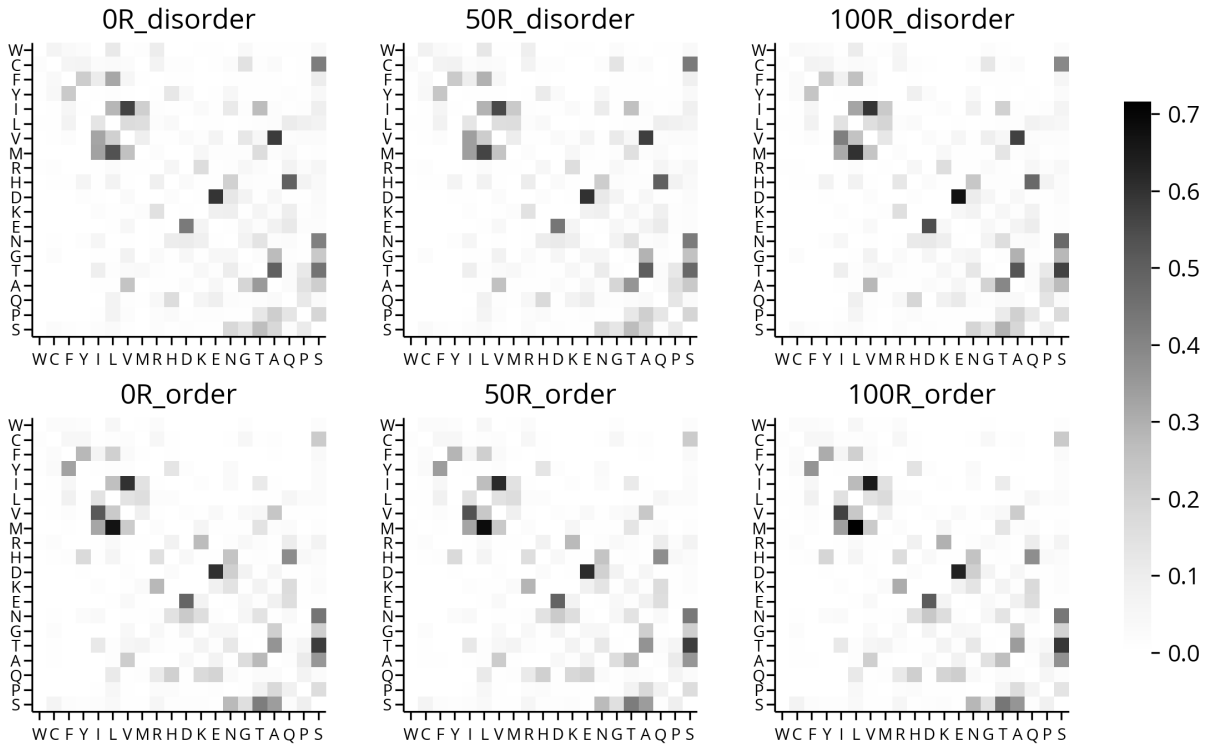

Figure B3. Rate matrices fit to meta-alignments yielded by different sampling strategies. Each panel is a mean of the rate coefficients fit to the meta-alignments yielded by a single sampling strategy ($n = 25$). See Fig. B2 for an explanation of the panel labels.

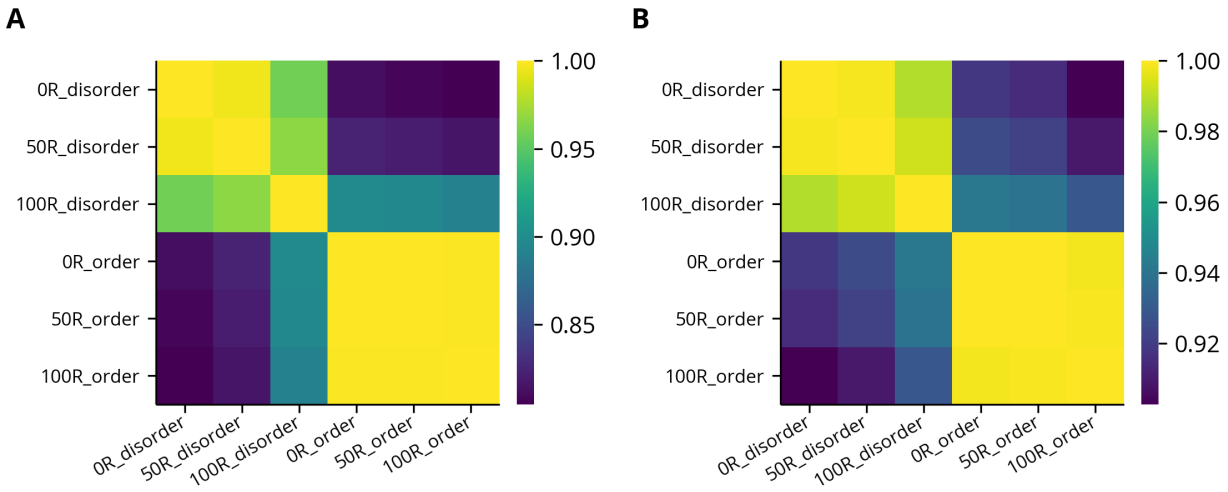

Figure B4. Correlations between mean exchangeability and rate matrices fit to meta-alignments yielded by different sampling strategies. (A) Correlations between the mean exchangeability matrices in Fig. B2. **(B)** Correlations between the mean rate matrices in Fig. B3.

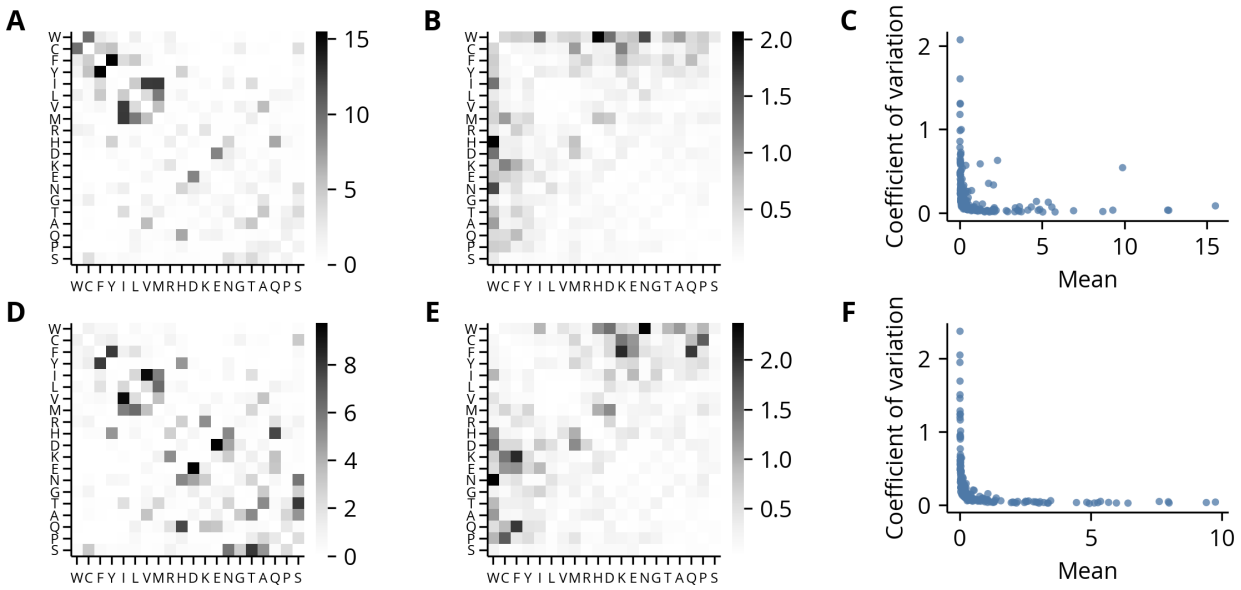

Figure B5. Coefficients of variation of the exchangeability matrices. For all panels, the top and bottoms rows correspond to the 50R_disorder and 50R_order meta-alignment sets, respectively. **(A, D)** Mean exchangeability matrices. **(B, E)** Coefficients of variation (ratio of the standard deviation to the mean) of exchangeability matrices. **(C, F)** The coefficient of variation is inversely proportional to the mean, indicating the variation in the parameter estimates is constant relative to their magnitude.

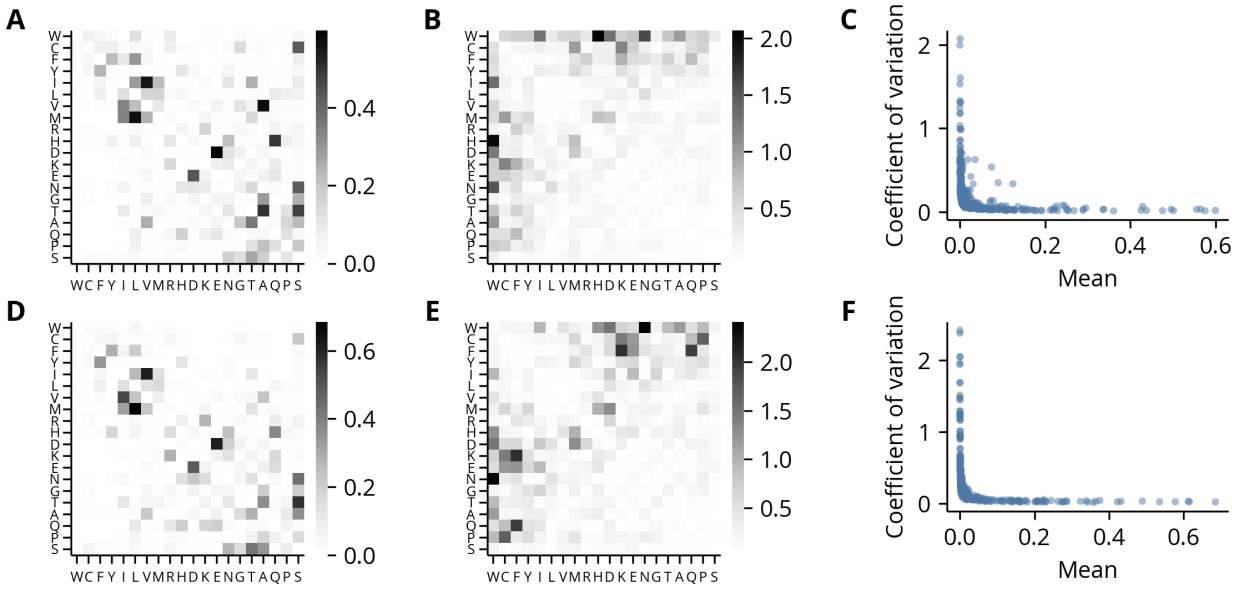

Figure B6. Coefficients of variation of the rate matrices. For all panels, the top and bottoms rows correspond to the 50R_disorder and 50R_order meta-alignment sets, respectively. **(A, D)** Mean rate matrices. **(B, E)** Coefficients of variation (ratio of the standard deviation to the mean) of rate matrices. **(C, F)** The coefficient of variation is inversely proportional to the mean, indicating the variation in the parameter estimates is constant relative to their magnitude.

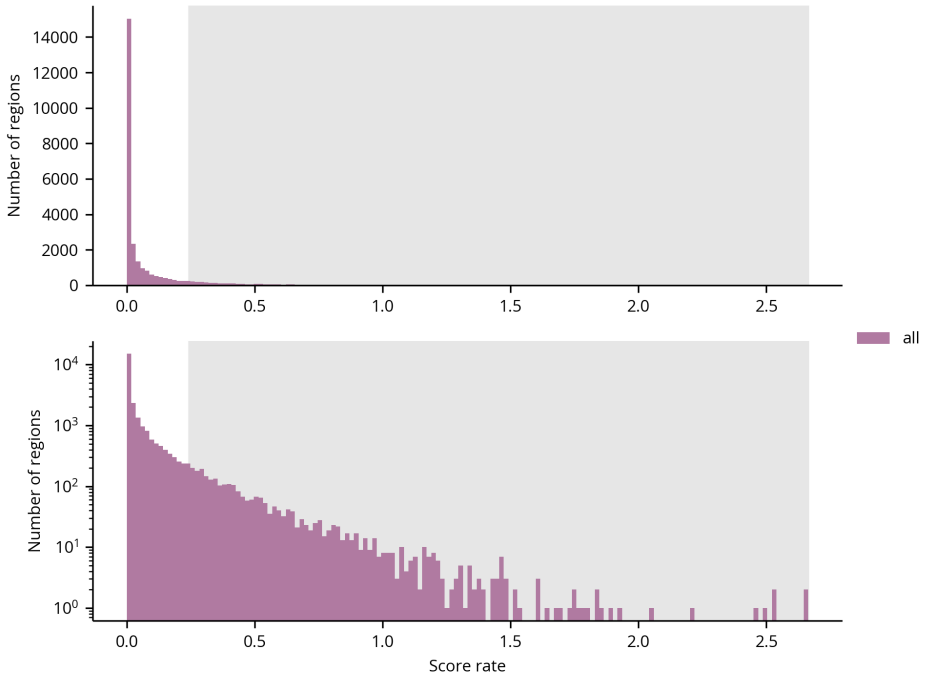

Figure B7. Histogram of disorder score rates in regions. The grey interval indicates the upper decile of the distribution across both disorder and order regions, which was used as the input set for the GO term enrichment analysis.

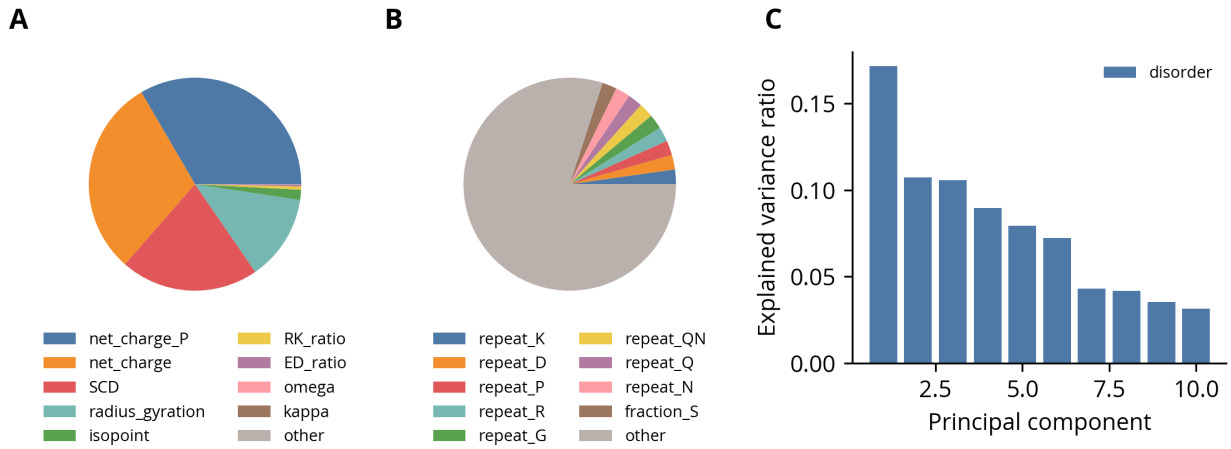

Figure B8. Variance ratios of disorder regions' feature roots. **(A)** Variance ratios before normalization. **(B)** Variance ratios after normalization. **(C)** Scree plot of the explained variance ratio by PC.

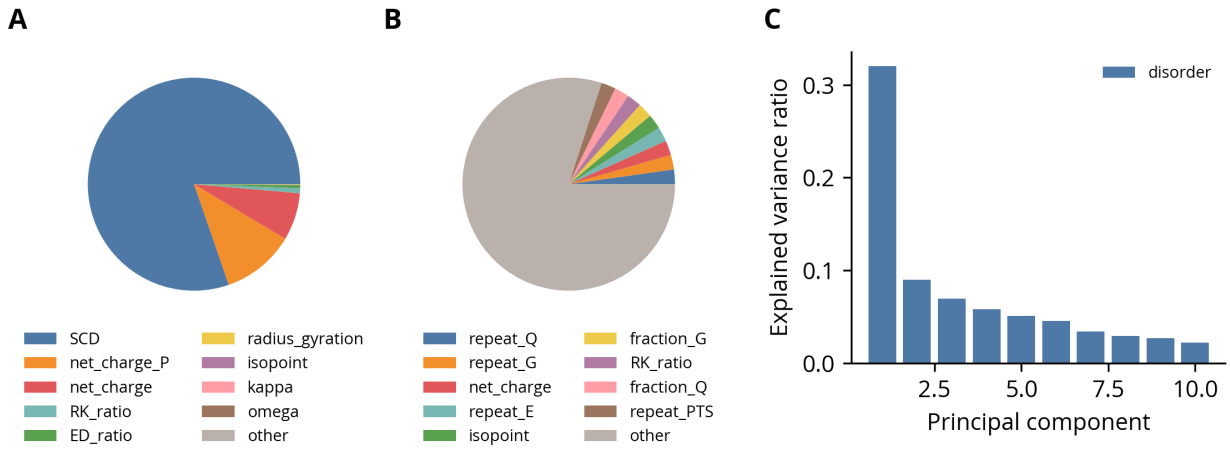

Figure B9. Variance ratios of disorder regions' feature rates. **(A)** Variance ratios before normalization. **(B)** Variance ratios after normalization. **(C)** Scree plot of the explained variance ratio by PC.

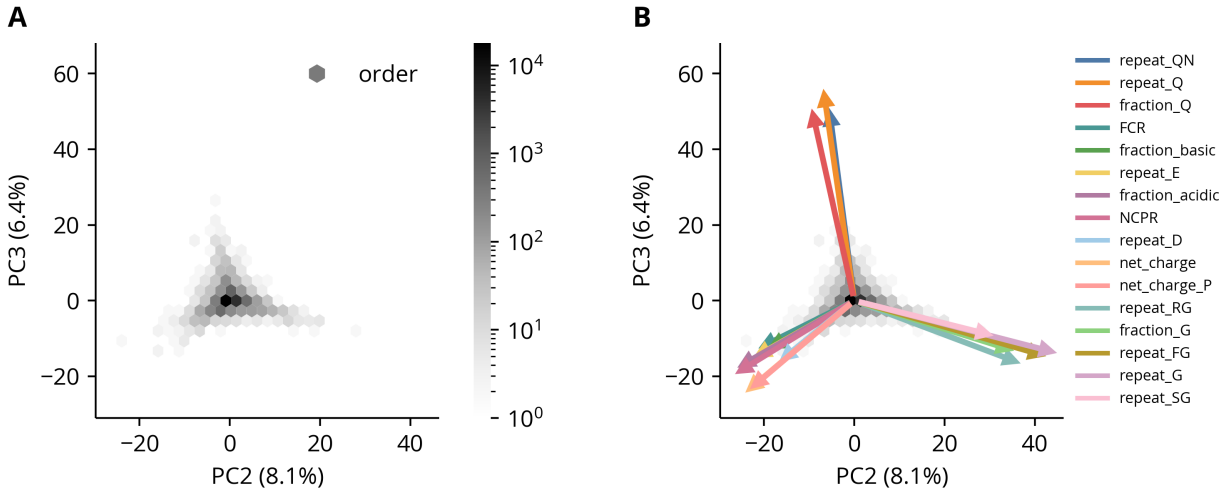

Figure B10. PCA of order regions' feature rates. **(A)** The second and third PCs of the order regions' feature rate distributions. The explained variance percentage of each component is indicated in parentheses in the axis labels. **(B)** The same plot as panel B with the projections of original variables onto the components shown as arrows. Only the 16 features with the largest projections are shown. Scaling of the arrows is arbitrary.

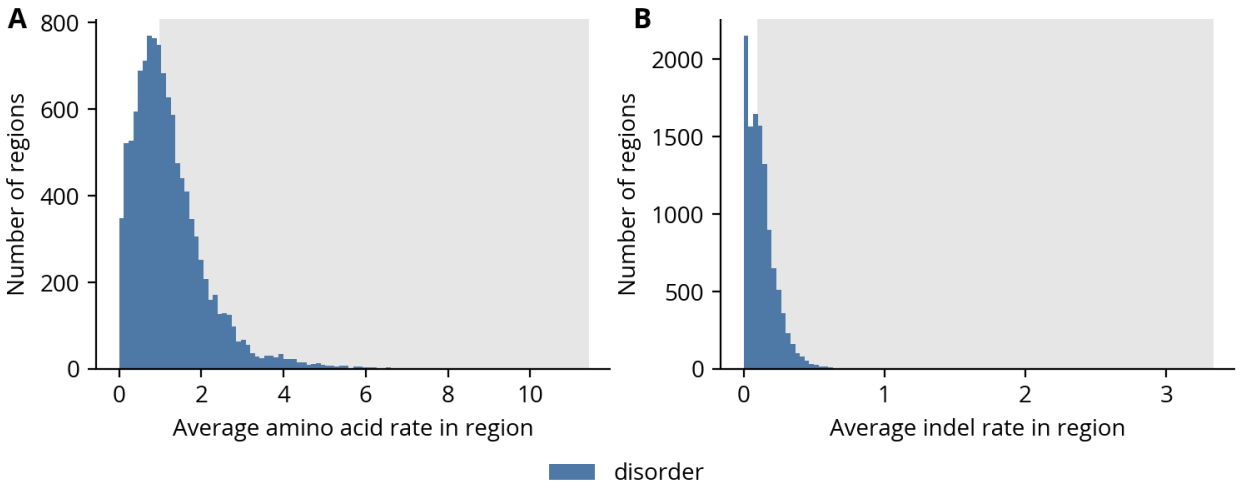

Figure B11. Rate distributions of substitution models fit to disorder regions. (A) Average amino acid rates in regions. **(B)**. Average indel rates in regions. For both panels, the grey intervals correspond to the subset of rapidly evolving regions used for the clustering and GO term enrichment analyses.

Table B1. Selected enriched annotations in clusters.

Cluster	*p*-value	Term ID	Term name
A	1.38E-03	GO:0005201	extracellular matrix structural constituent
A	3.38E-03	GO:0043062	extracellular structure organization
A	9.48E-03	GO:0030198	extracellular matrix organization
B	3.64E-04	GO:0090263	positive regulation of canonical Wnt signaling pathway
B	4.32E-04	GO:0060828	regulation of canonical Wnt signaling pathway
B	5.04E-04	GO:0030177	positive regulation of Wnt signaling pathway
B	8.91E-04	GO:0030111	regulation of Wnt signaling pathway
B	3.98E-03	GO:0061629	RNA polymerase II-specific DNA-binding transcription factor binding
B	7.15E-03	GO:0008134	transcription factor binding
D	2.44E-03	GO:0006999	nuclear pore organization
D	3.23E-03	GO:0006607	NLS-bearing protein import into nucleus
D	3.60E-03	GO:0008104	protein localization
D	3.74E-03	GO:0045184	establishment of protein localization
D	3.78E-03	GO:0044613	nuclear pore central transport channel
D	3.78E-03	GO:0017056	structural constituent of nuclear pore
E	3.66E-04	GO:0070161	anchoring junction
E	7.11E-04	GO:0030054	cell junction
E	1.66E-03	GO:0022843	voltage-gated cation channel activity
E	2.12E-03	GO:0022832	voltage-gated channel activity
E	2.12E-03	GO:0005244	voltage-gated ion channel activity
F	2.92E-04	GO:0033365	protein localization to organelle
F	4.08E-04	GO:0051179	localization
F	5.43E-04	GO:0034504	protein localization to nucleus
F	8.68E-04	GO:0034613	cellular protein localization
F	1.57E-03	GO:0008104	protein localization
F	1.67E-03	GO:0006606	protein import into nucleus
F	2.10E-03	GO:0051170	import into nucleus
G	2.40E-04	GO:0005459	UDP-galactose transmembrane transporter activity
G	2.40E-04	GO:0005338	nucleotide-sugar transmembrane transporter activity
G	2.40E-04	GO:0015165	pyrimidine nucleotide-sugar transmembrane transporter activity
G	2.40E-04	GO:0072334	UDP-galactose transmembrane transport
G	2.40E-04	GO:0090481	pyrimidine nucleotide-sugar transmembrane transport
G	2.40E-04	GO:0015780	nucleotide-sugar transmembrane transport
G	1.41E-03	GO:0015932	nucleobase-containing compound transmembrane transporter activity
G	2.33E-03	GO:1901505	carbohydrate derivative transmembrane transporter activity
G	2.33E-03	GO:1901264	carbohydrate derivative transport
H	2.14E-04	GO:0007113	endomitotic cell cycle
H	1.51E-03	GO:0051726	regulation of cell cycle
I	5.02E-04	GO:0007616	long-term memory
I	6.03E-04	GO:0099177	regulation of trans-synaptic signaling
I	6.03E-04	GO:0050804	modulation of chemical synaptic transmission
I	8.90E-04	GO:0010646	regulation of cell communication
I	9.41E-04	GO:0023051	regulation of signaling
J	1.47E-03	GO:0008172	S-methyltransferase activity
J	2.37E-03	GO:0042800	histone methyltransferase activity (H3-K4 specific)
J	3.76E-03	GO:0034708	methyltransferase complex
J	4.79E-03	GO:0051568	histone H3-K4 methylation
J	8.43E-03	GO:0035097	histone methyltransferase complex
L	2.51E-03	GO:0031507	heterochromatin assembly
L	2.51E-03	GO:0031497	chromatin assembly
L	3.00E-03	GO:0070828	heterochromatin organization
L	3.91E-03	GO:0003677	DNA binding
L	4.70E-03	GO:0003676	nucleic acid binding

Table B2. Features and their definitions.

Feature ID	Feature name	Group name	Range	Description	Changes from Zarin *et al.* [125]
fraction_S	S fraction	amino acid content	[0, 1]		
fraction_P	P fraction	amino acid content	[0, 1]		
fraction_T	T fraction	amino acid content	[0, 1]		
fraction_A	A fraction	amino acid content	[0, 1]		
fraction_H	H fraction	amino acid content	[0, 1]		
fraction_Q	Q fraction	amino acid content	[0, 1]		
fraction_N	N fraction	amino acid content	[0, 1]		
fraction_G	G fraction	amino acid content	[0, 1]		
FCR	fraction charged residues	charge properties	[0, 1]	basic residue fraction + acidic residue fraction	
NCPR	net charge per residue	charge properties	[-1, 1]	basic residue fraction - acidic residue fraction	
net_charge	net charge	charge properties	$(-\infty, \infty)$	#[RK] - #[DE]	
net_charge_P	net charge with phosphorylation	charge properties	$(-\infty, \infty)$	net charge including phosphorylation of [ST]P consensus sites with -1.5 charge per site	
kappa	kappa	charge properties	(0, 1]	measure of separation between positively and negatively charged residues	
omega	omega	charge properties	(0, 1]	measure of separation between charged residues or prolines and all other residues	
SCD	sequence charge decoration	charge properties	$(-\infty, \infty)$	measure of separation between positively and negatively charged residues	
RK_ratio	R/K ratio	charge properties	$(0, \infty)$	adjusted ratio of arginine to lysine residues: (#R + 1)/(#K + 1)	
ED_ratio	E/D ratio	charge properties	$(0, \infty)$	adjusted ratio of glutamic acid to aspartic acid residues: (#E + 1)/(#D + 1)	
fraction_acidic	acidic residue fraction	physiochemical properties	[0 ,1]		

Continued on next page

Table B2 (continued)

Feature ID	**Feature name**	**Group name**	**Range**	**Description**	**Changes from Zarin *et al.* [125]**
fraction_basic	basic residue fraction	physiochemical properties	[0 ,1]		
fraction_aliphatic	aliphatic residue fraction	physiochemical properties	[0 ,1]		
fraction_polar	polar residue fraction	physiochemical properties	[0 ,1]		removed glycine
fraction_chainexp	chain-expanding residue fraction	physiochemical properties	[0 ,1]		
fraction_aromatic	aromatic residue fraction	physiochemical properties	[0 ,1]		
fraction_disorder	disorder-promoting residue fraction	physiochemical properties	[0 ,1]		
radius_gyration	radius of gyration	physiochemical properties	[0, ∞)	number of residues to the 0.6 power	substituted for length
hydropathy	hydropathy	physiochemical properties	[0 ,1]	normalized Kyte-Doolittle scale	
isopoint	isoelectric point	physiochemical properties	($-\infty$, ∞)	pH where charge of peptide is neutral	
PPII_propensity	PPII propensity	physiochemical properties	[0, 1]	propensity for proline to form left-handed helices	
repeat_Q	Q repeat fraction	repeats and complexity	[0, 1]	fraction 2 or more consecutive Q	
repeat_N	N repeat fraction	repeats and complexity	[0, 1]	fraction 2 or more consecutive N	
repeat_S	S repeat fraction	repeats and complexity	[0, 1]	fraction 2 or more consecutive S	
repeat_G	G repeat fraction	repeats and complexity	[0, 1]	fraction 2 or more consectuive G	
repeat_E	E repeat fraction	repeats and complexity	[0, 1]	fraction 2 or more consecutive E	
repeat_D	D repeat fraction	repeats and complexity	[0, 1]	fraction 2 or more consecutive D	
repeat_K	K repeat fraction	repeats and complexity	[0, 1]	fraction 2 or more consecutive K	
repeat_R	R repeat fraction	repeats and complexity	[0, 1]	fraction 2 or more consecutive R	

Continued on next page

Table B2 (continued)

Feature ID	Feature name	Group name	Range	Description	Changes from Zarin *et al.* [125]
repeat_P	P repeat fraction	repeats and complexity	[0, 1]	fraction 2 or more consecutive P	
repeat_QN	[QN] repeat fraction	repeats and complexity	[0, 1]	fraction 2 or more consecutive [QN]	
repeat_RG	[RG] repeat fraction	repeats and complexity	[0, 1]	fraction 2 or more consecutive [RG]	
repeat_FG	[FG] repeat fraction	repeats and complexity	[0, 1]	fraction 2 or more consecutive [FG]	
repeat_SG	[SG] repeat fraction	repeats and complexity	[0, 1]	fraction 2 or more consecutive [SG]	
repeat_SR	[SR] repeat fraction	repeats and complexity	[0, 1]	fraction 2 or more consecutive [SR]	
repeat_AP	[KAP] repeat fraction	repeats and complexity	[0, 1]	fraction 2 or more consecutive [KAP]	
repeat_TS	[PTS] repeat fraction	repeats and complexity	[0, 1]	fraction 2 or more consecutive [PTS]	
wf_complexity	Wootton-Federhen sequence complexity	repeats and complexity	[0, 1]	complexity based on SEG algorithm: blob length=IDR length, step size=1	
CLV_Separin_Metazoa	separase cleavage motif	motifs	[0, ∞)		Metazoa motif instead of fungi
DEG_APCC_KENBOX_2	APCC-binding destruction motif	motifs	[0, ∞)		
DEG_APCC_TPR_1	APCC-TPR-docking motif	motifs	[0, ∞)		
DOC_CKS1_1	Cks1 ligand	motifs	[0, ∞)		
DOC_MAPK_DCC_7	MAPK docking motif	motifs	[0, ∞)		
DOC_MAPK_gen_1	MAPK docking motif	motifs	[0, ∞)		
DOC_MAPK_HePTP_8	MAPK docking motif	motifs	[0, ∞)		
DOC_PP1_RVXF_1	PP1-docking motif RVXF	motifs	[0, ∞)		
DOC_PP2B_PxIxI_1	calcineurin (PP2B)-docking motif PxIxI	motifs	[0, ∞)		
LIG_APCC_Cbox_1	APC/C_Apc2-docking motif	motifs	[0, ∞)		Metazoa motif instead of fungi
LIG_AP_GAE_1	gamma-adaptin ear interaction motif	motifs	[0, ∞)		
LIG_CaM_IQ_9	helical calmodulin binding motif	motifs	[0, ∞)		
LIG_EH_1	EH ligand	motifs	[0, ∞)		

Continued on next page

Table B2 (continued)

Feature ID	Feature name	Group name	Range	Description	Changes from Zarin *et al.* [125]
LIG_eIF4E_1	eIF4E binding motif	motifs	[0, ∞)		
LIG_GLEBS_BUB3_1	GLEBS motif	motifs	[0, ∞)		
LIG_LIR_Gen_1	Atg8 protein family ligands	motifs	[0, ∞)		same ELM entry, but updated regex
LIG_PCNA_PIPBox_1	PCNA binding PIP box	motifs	[0, ∞)		same ELM entry, but updated regex
LIG_SUMO_SIM_par_1	SUMO interaction site	motifs	[0, ∞)		
MOD_CDK_SPxK_1	CDK phosphorylation site	motifs	[0, ∞)		
MOD_LATS_1	LATS kinase phosphorylation motif	motifs	[0, ∞)		
MOD_SUMO_for_1	sumoylation site	motifs	[0, ∞)		
TRG_ER_FFAT_1	FFAT motif	motifs	[0, ∞)		same ELM entry, but updated regex
TRG_Golgi_diPhe_1	ER export signals	motifs	[0, ∞)		
TRG_NLS_MonoExtN_4	classical nuclear localization signals	motifs	[0, ∞)		
MOD_CDK_STP	CDK phosphorylation motif	motifs	[0, ∞)		
MOD_MEC1	Mec1 phosphorylation motif	motifs	[0, ∞)		
MOD_PRK1	Prk1 phosphorylation motif	motifs	[0, ∞)		
MOD_IPL1	Ipl1 phosphorylation motif	motifs	[0, ∞)		
MOD_PKA	Pka phosphorylation motif	motifs	[0, ∞)		
MOD_CKII	Ckii phosphorylation motif	motifs	[0, ∞)		
MOD_IME2	Ime2 phosphorylation motif	motifs	[0, ∞)		
DOC_PRO	proline rich motif	motifs	[0, ∞)		
TRG_ER_HDEL	ER localization motif	motifs	[0, ∞)		
TRG_MITOCHONDRIA	mitochondrial localization motif	motifs	[0, ∞)		

Continued on next page

Table B2 (continued)

Feature ID	**Feature name**	**Group name**	**Range**	**Description**	**Changes from Zarin *et al.* [125]**
MOD_ISOMERASE	disulfide isomerase motif	motifs	[0, ∞)		
TRG_FG	FG nucleoporin motif	motifs	[0, ∞)		
INT_RGG	RGG motif	motifs	[0, ∞)		

Table B3. Feature regular expressions.

Feature ID	Regular expression
fraction_S	S
fraction_P	P
fraction_T	T
fraction_A	A
fraction_H	H
fraction_Q	Q
fraction_N	N
fraction_G	G
fraction_acidic	[DE]
fraction_basic	[RK]
fraction_aliphatic	[ALMIV]
fraction_polar	[QNSTCH]
fraction_chainexp	[EDRKP]
fraction_aromatic	[FYW]
fraction_disorder	[TAGRDHQKSEP]
repeat_Q	Q{2,}
repeat_N	N{2,}
repeat_S	S{2,}
repeat_G	G{2,}
repeat_E	E{2,}
repeat_D	D{2,}
repeat_K	K{2,}
repeat_R	R{2,}
repeat_P	P{2,}
repeat_QN	[QN]{2,}
repeat_RG	[RG]{2,}
repeat_FG	[FG]{2,}
repeat_SG	[SG]{2,}
repeat_SR	[SR]{2,}
repeat_AP	[KAP]{2,}
repeat_TS	[PTS]{2,}
CLV_Separin_Metazoa	E[IMPVL][MLVP]R.
DEG_APCC_KENBOX_2	.KEN.
DEG_APCC_TPR_1	.[ILM]R
DOC_CKS1_1	[MPVLIFWYQ].(T)P..
DOC_MAPK_DCC_7	[RK].{2,4}[LIVP]P.[LIV].[LIVMF]|[RK].{2,4}[LIVP].P[LIV].[LIVMF]
DOC_MAPK_gen_1	[KR]{0,2}[KR].{0,2}[KR].{2,4}[ILVM].[ILVF]

Continued on next page

Table B3 (continued)

Feature ID	Regular expression
DOC_MAPK_HePTP_8	([LIV][^P][^P][RK]....[LIVMP].[LIV].[LIVMF])|([LIV][^P][^P][RK][RK]G.{4,7}[LIVMP].[LIV].[LIVMF])
DOC_PP1_RVXF_1	..[RK].{0,1}[VIL][^P][FW].
DOC_PP2B_PxIxI_1	.P[^P]I[^P][IV][^P]
LIG_APCC_Cbox_1	[DE]R[YFH][ILFVM][PAG].R
LIG_AP_GAE_1	[DE][DES][DEGAS]F[SGAD][DEAP][LVIMFD]
LIG_CaM_IQ_9	[ACLIVTM][^P][^P][ILVMFCT]Q[^P][^P][^P][RK][^P]{4,5}[RKQ][^P][^P]
LIG_EH_1	.NPF.
LIG_eIF4E_1	Y....L[VILMF]
LIG_GLEBS_BUB3_1	[EN][FYLW][NSQ].EE[ILMVF][^P][LIVMFA]
LIG_LIR_Gen_1	[EDST].{0,2}[WFY][^RKPGWFY][^PG][ILVFM]((.{0,4}[PLAFIVMY])|($)|(.{0,3}[ED]))
LIG_PCNA_PIPBox_1	[QM].[^FHWY][LIVM][^P][^PFWYMLIV](([FYHL][FYW])|([FYH][FYWL]))..
LIG_SUMO_SIM_par_1	[DEST]{0,5}.[VILPTM][VIL][DESTVILMA][VIL].{0,1}[DEST]{1,10}
MOD_CDK_SPxK_1	...([ST])P.[KR]
MOD_LATS_1	H.[KR]..([ST])[^P]
MOD_SUMO_for_1	[VILMAFP](K).E
TRG_ER_FFAT_1	[EDS].{0,4}[ED][FY][FYKREM][DE][AC].{1,2}[EDST]
TRG_Golgi_diPhe_1	Q.{6,6}FF.{6,7}
TRG_NLS_MonoExtN_4	(([PKR].{0,1}[^DE])|([PKR]))((K[RK])|(RK))(([^DE][KR])|([KR][^DE]))[^DE]
MOD_CDK_STP	[ST]P
MOD_MEC1	[ST]Q
MOD_PRK1	[LIVM]....TG
MOD_IPL1	[RK].[ST][LIV]
MOD_PKA	R[RK].S
MOD_CKII	[ST][DE].[DE]
MOD_IME2	RP.[ST]
DOC_PRO	P..P
TRG_ER_HDEL	HDEL
TRG_MITOCHONDRIA	[MR]L[RK]
MOD_ISOMERASE	C..C
TRG_FG	F.FG|GLFG
INT_RGG	RGG|RG

APPENDIX C

Supporting information for chapter 3

Listing B1: Implementation of Baum-Welch for categorical distributions

In:
```
epsilon = 0.01
maxiter = 100

ll0 = None
model_hat = HMM(t_dists=t_dists_hat,
                e_dists=e_dists_hat,
                start_dist=start_dist_hat)
for numiter in range(maxiter):
    # Initialize count dictionaries
    ps = []
    t_counts = {state1: {state2: 0 for state2 in t_dist}
                for state1, t_dist in t_dists_hat.items()}
    e_counts = {state: {emit: 0 for emit in e_dist}
                for state, e_dist in e_dists_hat.items()}
    start_count = {state: 0 for state in start_dist_hat}

    # Get counts across all examples
    for example in data:
        xs, ys = example
        fs, ss_f = model_hat.forward(ys)
        bs, ss_b = model_hat.backward(ys)

        p = reduce(lambda x, y: x+y, map(log, ss_f))
        ss_f = list(accumulate(map(log, ss_f)))
        ss_b = list(accumulate(map(log, ss_b[::-1])))[::-1]
        ps.append(p)

        # t_counts
        for t in range(len(ys)-1):
            for state1, t_count in t_counts.items():
                for state2 in t_count:
                    term1 = fs[state1][t] * t_dists_hat[state1][state2]
                    term2 = e_dists_hat[state2][ys[t+1]] * bs[state2][t+1]
                    count = term1 * term2
                    t_count[state2] += count * exp(ss_f[t] + ss_b[t+1] - p)

        # e_counts
        for t in range(len(ys)):
            for state, e_count in e_counts.items():
                if ys[t] in e_count:
                    count = fs[state][t]*bs[state][t]
```

```
                e_count[ys[t]] += count * exp(ss_f[t] + ss_b[t] - p)

        # start_count
        for state in start_count:
            count = fs[state][0]*bs[state][0]
            start_count[state] += count * exp(ss_f[0] + ss_b[0] - p)

    # Format parameters for display
    t_string = pprint.pformat(t_dists_hat)
    t_string = t_string.replace('\n', '\n' + len('t_dists: ')*' ')
    e_string = pprint.pformat(e_dists_hat)
    e_string = e_string.replace('\n', '\n' + len('e_dists: ')*' ')
    start_string = pprint.pformat(start_dist_hat)

    # Check stop condition
    # Don't want to repeat calculations,
    # so ith iterate checks previous update
    # For example, 0th iterate shows initial parameters,
    # and 1st iterate shows results of first update
    ll = sum(ps)
    if ll0 is not None and abs(ll - ll0) < epsilon:
        print(f'FINAL VALUES')
        print('log-likelihood:', ll)
        print('delta log-likelihood:', ll-ll0 if ll0 is not None else None)
        print('t_dists:', t_string)
        print('e_dists:', e_string)
        print('start_dist:', start_string)
        break

    # Print results
    print(f'ITERATION {numiter}')
    print('log-likelihood:', ll)
    print('delta log-likelihood:', ll-ll0 if ll0 is not None else None)
    print('t_dists:', t_string)
    print('e_dists:', e_string)
    print('start_dist:', start_string)
    print()

    # Normalize all counts and update model
    t_dists_hat = {}
    for state1, t_count in t_counts.items():
        t_sum = sum(t_count.values())
        t_dist_hat = {}
        for state2, count in t_count.items():
            t_dist_hat[state2] = count / t_sum
        t_dists_hat[state1] = t_dist_hat

    e_dists_hat = {}
    for state, e_count in e_counts.items():
        e_sum = sum(e_count.values())
        e_dist_hat = {}
        for emit, count in e_count.items():
            e_dist_hat[emit] = count / e_sum
        e_dists_hat[state] = e_dist_hat

    start_sum = sum(start_count.values())
    start_dist_hat = {}
    for state, count in start_count.items():
```

```
        start_dist_hat[state] = count / start_sum

    ll0 = ll
    model_hat = HMM(t_dists=t_dists_hat,
                    e_dists=e_dists_hat,
                    start_dist=start_dist_hat)
```